



UNIVERSIDADE D
COIMBRA



Maria do Rosário Dinis Moreira Fino

THE APPLICATION OF ICB AS AN EXTERNAL
THERMAL INSULATING COMPOSITE SYSTEM
AN EXPERIMENTAL AND NUMERICAL STUDY

PhD Thesis in Sustainable Energy Systems supervised by Professor António
José Barreto Tadeu and Professor Nuno Albino Vieira Simões submitted to
the department of Mechanical Engineering of Faculty of Sciences and
Technology of the University of Coimbra

March 2018



THE APPLICATION OF ICB AS AN EXTERNAL THERMAL INSULATING COMPOSITE SYSTEM

An Experimental and Numerical Study

by

Maria do Rosário Dinis Moreira Fino

Thesis submitted to the Department of Mechanical Engineering, FCTUC
in partial fulfilment of the requirements for the degree of
Doctor of Philosophy in Sustainable Energy Systems

Supervisors

Professor António José Barreto Tadeu

Professor Nuno Albino Vieira Simões

March 2018

MITPortugal



FCT
Fundação para a Ciência e a Tecnologia
MINISTÉRIO DA CIÊNCIA, TECNOLOGIA E ENSINO SUPERIOR



to the memory of my father

to my brother António, for believing that there is always a way

Acknowledgements

The research work developed within this thesis was supported by the doctoral grant SFRH/BD/52303/2013 awarded by the Foundation for Science and Technology of the Portuguese Ministry of Education and Sciences under the program MIT Portugal - Sustainable Energy Systems. This work has also been developed under the projects FCOMP-01-0202-FEDER-033938, “MDfachada - MDCoberturas”, POCI-01-0145- FEDER-016852 “GRLF - Conception and behaviour of green roofs and living facades made of healthy engineered expanded cork systems” and POCI-01-0247-FEDER-003408 - “Slimframe PV & Cork Skin Project”, approved through the Incentive Scheme R&TD Co-promotion Projects and co-funded by the European Regional Development Fund through Compete2020. I’m also grateful for the financial support provided by Energy for Sustainability Initiative of the University of Coimbra for the dissemination of this work over the past few years.

I gratefully acknowledge the support and generosity of Amorim Isolamentos S.A. and Saint-Gobain Weber Portugal S.A.

This work could not have been developed without the support of my supervisors, colleagues, family and friends.

I would like to express my deep gratitude to Professor António Tadeu and Professor Nuno Simões, my research supervisors, for their patient guidance, encouragement and useful critiques of this research work. I would also like to extend my heartfelt appreciation to Professor Leopold Škerget for his precious help and valuable contribution to this work. I would be remiss if I did not thank all of my colleagues from the Institute for Research and Technological Development in Construction, Energy, Environment and Sustainability (ITeCons). In particular I would like to thank Saúl Martins, Aurélio Gonçalves, Sara Dias, António Nascimento, Gina Matias, Ruben Ramalho and Sofia Tavares for their help in the laboratory work, Michael Brett and Catarina Serra for their help in reviewing the English, and to Vitor Gil and Joana Prata, for their willingness to help with all of "the little things".

Finally, I wish to thank my family and friends for their support and encouragement throughout my study.

Abstract

The promotion of a more resource efficient and greener economy and the reduction of energy consumption are among the priorities defined in the Europe 2020 Strategy. The implementation of effective measures for reducing energy consumption in new construction and retrofitting existing buildings have therefore been set as priorities. The use of thermal insulation materials is the most efficient way of reducing heat loss in buildings, thus reducing heat energy needs. The potential of incorporating different types of waste and by-products, such as those produced in the cork processing industry, in construction materials and solutions is relevant for achieving a more sustainable construction and use of buildings throughout their life cycle.

Expanded cork agglomerate (ICB) has been used on an ad hoc basis as an alternative to external thermal insulating composite systems but without a detailed technical characterisation. This work aims to contribute to the characterisation and development of this system by incorporating ICB boards, both when they are used in new building construction and for retrofitting projects.

First, existing ICB coated buildings were visited to assess the main anomalies, its probable causes, and eventual solutions. A set of detailed application methods have been proposed. Constructive rules and construction details are presented. Maintenance actions to preserve the properties of the system are proposed.

Then, a wide range of laboratory tests were performed to evaluate the mechanical, hygrothermal and durability characteristics of both standard (90-110 kg/m³) and medium (140-160 kg/m³) density ICB. It was found that the medium density ICB has a better mechanical performance, without compromising its hygrothermal behaviour, and therefore more suitable to be used as external insulation. It was proven that it is also resistant to long-term exposure to external aggression.

The importance of varying moisture content on the thermal behaviour of a wall covered with medium density ICB, when exposed to rain, was evaluated. A simple analytical model that simulates the heat transfer phenomenon was used to quantify its importance by comparing the mathematical results with those obtained experimentally. Steady and unsteady state conditions for both summer and winter conditions were considered. The results show that the thermal behaviour of the wall is only affected during the rainy period, until the first few hours when the ICB starts to dry and is confined to the upper layers of ICB.

The influence of the solar heat flux, temperature, and relative humidity on OSB and concrete walls covered with medium density ICB, with different thicknesses, was evaluated. A boundary element numerical model was used to simulate the coupled heat and moisture transfer through the walls. Initially, the effect of the abrupt variation of relative humidity and temperature were simulated, allowing to conclude that the relative humidity variation is only significant when, during the course of the year, there are relevant weather changes. Thus, summer and winter real weather data of both Bragança (Portugal) and Seville (Spain) were used to simulate the walls' hygrothermal behaviour. The obtained results show that the short-term environment moisture variation has an impact limited to the outer surface layers and that the moisture along the wall is only high when the external moisture is high and remains high for an extended period.

Finally, wind resistance, water-tightness and resistance to impacts of the proposed constructive solutions were experimentally evaluated.

Resumo

A promoção de uma economia mais ecológica e mais eficiente a nível de recursos, assim como a redução do consumo de energia, estão entre as prioridades definidas na Estratégia para a Europa 2020. A implementação de medidas eficientes que permitam reduzir o consumo de energia, tanto em edifícios novos como em reabilitação, foi definida como prioritária. O uso de isolamento térmico é a maneira mais eficiente de minimizar as perdas de calor nos edifícios, reduzindo, assim, as necessidades de energia térmica. O potencial de incorporar diferentes tipos de resíduos e subprodutos, como os produzidos na indústria de processamento de cortiça, em materiais e soluções de construção, torna-se relevante para alcançar uma construção e uso mais sustentáveis dos edifícios ao longo de seu ciclo de vida.

O aglomerado de cortiça expandido (ICB) tem sido usado como uma alternativa aos sistemas de isolamento térmico pelo exterior, mas sem uma caracterização técnica detalhada. Este trabalho tem como objetivo contribuir para a caracterização e desenvolvimento de sistemas incorporando ICB, quer para aplicação em edifícios novos, quer em obras de reabilitação.

Como ponto de partida, foram visitados edifícios existentes revestidos a ICB, de forma a avaliar as suas principais anomalias, causas prováveis e eventuais soluções. São propostos um conjunto de métodos de aplicação do ICB e apresentados pormenores construtivos. De modo a preservar as propriedades do sistema, são ainda apresentados procedimentos de manutenção.

Após este trabalho inicial, foi realizada uma vasta campanha de testes laboratoriais de forma a avaliar as propriedades mecânicas, higrotérmicas e de durabilidade do ICB de densidade *standard* (90-110 kg/m³) e de média densidade (140-160 kg/m³). Verificou-se que o ICB de média densidade apresenta um melhor desempenho mecânico sem comprometer o seu desempenho higrotérmico sendo, portanto, mais adequado para ser usado como isolamento térmico pelo exterior. Foi ainda comprovada a sua resistência à ação prolongada das agressões externas.

Foi avaliada a importância da variação do teor de humidade no comportamento térmico de uma parede revestida com ICB de média densidade quando exposta à chuva. Um modelo analítico que simula o fenómeno de transferência de calor foi usado para quantificar a sua importância, através da comparação dos resultados matemáticos com os obtidos experimentalmente. Foram consideradas as situações de regime permanente e transiente, para as condições de verão e de inverno. Os resultados mostraram que o comportamento térmico da parede só é afetado durante o período de chuva e durante as primeiras horas de secagem do ICB, e é confinado às camadas superficiais do ICB.

Foi avaliada a influência da radiação solar, temperatura e da humidade relativa em paredes de OSB e de betão revestidas com ICB de média densidade com diferentes espessuras. Foi utilizado um modelo numérico baseado no método dos elementos de fronteira para simular a transferência simultânea de calor e humidade. Inicialmente, foi simulado o efeito da variação abrupta da humidade relativa e temperatura, permitindo concluir que a variação da humidade relativa só é significativa quando, no decorrer do ano, há mudanças climáticas relevantes. Assim, os dados meteorológicos de verão e de inverno de Bragança (Portugal) e de Sevilha (Espanha) foram utilizados para simular o comportamento higrotérmico das paredes. Os resultados obtidos mostraram que a variação a curto prazo da humidade do ambiente tem um impacto limitado às camadas da superfície externa e que a humidade ao longo da parede é apenas alta quando a humidade exterior é alta e permanece alta durante um período prolongado.

Por fim, a resistência ao vento, estanquidade e a resistência ao impacto das soluções construtivas propostas foram avaliadas.

Table of contents

Chapter 1

Introduction

1.1	Context and motivation	1
1.2	Objectives	1
1.3	Thesis outline	2

Chapter 2

Buildings Coated with Expanded Cork Boards: Main Anomalies and General Application Rules

2.1	Introduction.....	7
2.2	Survey of existing buildings coated with ICB	10
2.3	General rules of application.....	17
2.3.1	Application methods of the ICB boards	18
2.3.2	Constructive details of singularities	21
2.4	Maintenance actions	26
2.5	Final remarks.....	28
2.6	References.....	29

Chapter 3

Expanded Cork Properties

3.1	Introduction.....	35
3.2	Mechanical characterization	39
3.2.1	Dimensional stability under specified temperature and humidity conditions	39
3.2.2	Bending behaviour.....	40
3.2.3	Tensile strength perpendicular to faces: dry and wet conditions	41
3.2.4	Compressive behaviour	43
3.2.5	Shear behaviour	44
3.2.6	Behaviour under point load.....	45
3.2.7	Deformation under specified compressive load and temperature conditions	46
3.3	Hygrothermal properties.....	47

3.3.1	Basic properties (standard and medium density).....	47
3.3.1.1	Water vapour transmission properties.....	47
3.3.1.2	Short and long-term water absorption by partial immersion	49
3.3.1.3	Thermal conductivity at dry and reference state	50
3.3.2	Comprehensive study of medium density ICB hygrothermal properties	51
3.3.2.1	Open porosity	51
3.3.2.2	Dry density, apparent density and saturation moisture content.	52
3.3.2.3	Variation of the thermal conductivity with moisture.....	53
3.3.2.4	Hygroscopic sorption properties	55
3.3.2.5	Water absorption coefficient by partial immersion	56
3.3.2.6	Liquid water conductivity/diffusivity	57
3.3.3	Drying	59
3.4	Durability	63
3.4.1	Freeze-thaw cycles	63
3.4.2	Compressive creep.....	65
3.4.3	Ageing test by exposure to xenon-arc light.....	66
3.5	Final Remarks	67
3.6	References.....	68

Chapter 4

Importance of Moisture on the Thermal Performance

4.1	Introduction.....	81
4.2	Methodology	85
4.2.1	Analytical model for conduction.....	85
4.2.2	Experimental Set-up	88
4.2.3	Test procedures.....	88
4.2.4	Test specimen	90
4.2.5	Data acquisition chain	91
4.3	Heat transfer under dry conditions.....	92
4.3.1	Steady-state conditions	93
4.3.2	Unsteady-state conditions	94
4.4	Heat transfer under wet conditions	96

4.4.1	Steady state conditions	96
4.4.2	Unsteady state conditions	99
4.4.2.1	Summer environment conditions	99
4.4.2.2	Winter environment conditions	102
4.5	Final remarks.....	106
4.6	References.....	107

Chapter 5

Modelling Moisture

5.1	Introduction.....	113
5.2	Governing transport equations for a two-phase system.....	116
5.2.1	Initial and boundary conditions	118
5.3	Integral representations for energy and moisture transport equations	119
5.4	Material properties	121
5.5	Validation of the material properties	125
5.6	Importance of the moisture and heat flow through walls coated with expanded cork	127
5.7	Case studies.....	129
5.7.1	Constructive solutions	129
5.7.2	Real climate data	129
5.7.3	Simulation results	130
5.7.3.1	Summer and winter conditions for Bragança and Seville: OSB constructive solution	130
5.7.3.2	OSB versus concrete constructive solutions.....	137
5.8	Final remarks.....	139
5.9	References.....	140

Chapter 6

Validation of the Solutions when Subjected to Wind, Rain and Impact Loads

6.1	Introduction.....	147
6.2	Experimental characterisation of constructive solutions	149
6.2.1	Construction of the test specimens.....	150
6.2.2	Test procedures.....	153

6.2.3	Test results	156
6.3	Final remarks.....	160
6.4	References.....	160

Chapter 7

Final Considerations

7.1	Overview and main conclusions	165
7.2	Future work	167

Index of figures

Chapter 2

Figure 2-1: Concert hall known as <i>Pavilhão de Portugal</i> .	10
Figure 2-2: Corkhouse: a) Main entrance of the house (view of both facade and roof covered with ICB); b) Application phase of the ICB boards on the concrete walls .	11
Figure 2-3: Quinta do Portal: a) Overview of the NE and NW facades; b) Application of the ICB boards onto the corrugated metallic panels.	11
Figure 2-4: Ecocabana: a) Left side of the building; b) Application of the ICB boards onto the wooden frame structure.	12
Figure 2-5: Ecorkhotel: a) Location of the main building and the suites area (Google Earth); b) Detail of the bonding phase during the application of the ICB boards.	12
Figure 2-6: Logowines: a) Overview of the building; b) Method of application of the ICB boards.	13
Figure 2-7: Surf Centre of Viana do Castelo: a) Facade; b) Flat roof.	13
Figure 2-8: ICB application on wall using double bonding.	18
Figure 2-9: Example of double bonding application: a) Spreading of mortar on ICB; b) Spreading of mortar on the wall.	19
Figure 2-10: Application by using a corrugated metal panel with an air layer.	19
Figure 2-11: Application of the ICB boards by using discontinuous steel profile systems.	20
Figure 2-12: Application on wooden panels.	21
Figure 2-13: Illustration of the use of the perforated base wall profile.	22
Figure 2-14: Base wall details: a) System starting off the ground - different thicknesses of insulation boards; b) System starting off a balcony or terrace.	22
Figure 2-15: Wall capping: a) Top cover cross section; b) Top cover front view; c) Metallic wall capping.	23
Figure 2-16: Connection facade/flat roof: a) General view; b) Detail of the wall capping application.	23
Figure 2-17: Corner connections: a) Special one-piece corner ICB; b) ICB half lap boards cut at 45° and c) Staggered ICB.	24
Figure 2-18: Connection with windows: a) Connection with window sill; b) Connections with side jambs.	25

Figure 2-19: Elements on facade: a) Attachment elements on the facade (drop tube); b) Expansion joint.....	25
Figure 2-20: Washing of a wall: a) Moss removal with water pressure; b) Facade appearance after being washed.....	26
Figure 2-21: Maintenance actions: a) Visual appearance of ICB after being submitted to slight abrasion; b) ICB boards before and after being subjected to deeper abrasion.	27

Chapter 3

Figure 3-1: Apparatus for bending and force-deflection curves for both ST and MD ICB...41	
Figure 3-2: Tensile strength perpendicular to faces. Force-displacement curves for ST and MD ICB in wet conditions: a) Set 1: 7 days; b) Set 2: 28 days.	42
Figure 3-3: Compressive test apparatus and force- displacement curves, for ST and MD ICB, 50 and 70 mm thick.	43
Figure 3-4: Shear test apparatus and force-displacement curves for the ST and MD ICB....	44
Figure 3-5: Point load apparatus and force-deformation results for the ST and MD ICB.....	45
Figure 3-6: Measured thermal conductivity of medium density expanded cork as a function of moisture content u [kg/kg] (the triangle represents the mean value of λ_{meas} at reference conditions obtained experimentally for a mean moisture content of 0.022 kg/kg (section 3.3.1.3)).	54
Figure 3-7: Adsorption (continuous blue line) and desorption curves (red dashed line) of medium density expanded cork at $(23 \pm 0.5) ^\circ\text{C}$ and their average (green triangles).....	55
Figure 3-8: Test apparatus for water absorption evaluation and test results.	57
Figure 3-9: W/W_{sat} curve and the experimental data represented by green dots.	59
Figure 3-10: Liquid water conductivity/ diffusivity function of φ for MD ICB.....	59
Figure 3-11: Test specimens: a) During immersion; b) Draining stage.	60
Figure 3-12: Mean moisture content u [kg/kg] for each Set for the first nine drying hours and the respective trend lines.	61
Figure 3-13: Mean water loss [g/h] in the first 9 drying hours for each Set.	62
Figure 3-14: Expanded cork boards drying in climatic chamber (from left to right: Set 3, Set 2 and Set 1: a) $t= 3$ h; b) $t= 9$ h.....	62
Figure 3-15: Mean moisture content u [kg/kg] change after the first nine drying hours.	63

Figure 3-16: Test specimens during freezing conditioning (picture) and force-displacement curves of the compressive test.	64
Figure 3-17: Medium measured values (Meas.) and evolution of the deformation for the compressive loads of 30, 40 and 50 kPa extrapolated until $t = 87600$ h (Ext.).....	66
Figure 3-18: Test specimen subjected to ageing: a) Test specimen before test; b) Test specimen after the test with the right side slightly polished.....	67

Chapter 4

Figure 4-1: Geometry of the multilayer system.	86
Figure 4-2: Set-point of temperatures for both chambers (the marked line relates to the OUT chamber while the solid line relates to the IN chamber): a) Steady-state; b) Winter unsteady-state condition; c) Summer unsteady-state condition (the temperature in the IN chamber was not imposed).	89
Figure 4-3: Wall test specimen: a) Composition: 1- OSB; 2- waterproofing and bonding mortar; 3-medium density expanded cork board); b) Numbering of the expanded cork board panels and of the sub-blocks; Measuring points.....	90
Figure 4-4: Cross section of the specimen. Position identification of the thermocouples and heat flux sensors along the constructive solution.	91
Figure 4-5: Heat transfer under dry steady-state conditions: a) Temperatures; b) Heat fluxes.	93
Figure 4-6: Experimental and analytical results in dry conditions a) Temperatures for the first 132 h of testing; b) Temperatures for $72 \text{ h} < t < 96 \text{ h}$; c) Heat fluxes.....	95
Figure 4-7: Time lag and decrement factor provided by the constructive solution under dry conditions.	95
Figure 4-8: Experimental (solid lines) and analytical (dashed lines) results in wet conditions a) Temperatures for the first 68 h of testing; b) Temperatures for $28.5 \text{ h} < t < 30.5 \text{ h}$; c) Heat fluxes.	97
Figure 4-9: Experimental temperatures registered for unsteady summer conditions in the first 180 h: water spray lasting 1 h occurred at instant $t = 81.4 \text{ h}$	99
Figure 4-10: Temperatures before, during and after wetting for a 24 hours cycle: a) Before wetting ($56 \text{ h} \leq t < 80 \text{ h}$ – solid lines) and during wetting ($80 \text{ h} \leq t < 104 \text{ h}$ - dashed lines); b) Before wetting ($56 \text{ h} \leq t < 80 \text{ h}$ – solid lines) and after wetting ($104 \text{ h} \leq t < 128 \text{ h}$ - dashed lines).....	100

Figure 4-11: Experimental (solid lines) and analytical results (dashed lines) in summer wet conditions a) Temperatures for $70 \text{ h} < t < 110 \text{ h}$; b) Temperatures for $81 \text{ h} < t < 83 \text{ h}$; c) Heat fluxes for $70 \text{ h} < t < 110 \text{ h}$.	101
Figure 4-12: Experimental temperatures for unsteady wet winter conditions for the first 144 h.	103
Figure 4-13: Temperature comparison between the wall before and after wetting for a 24-hour cycle, for winter conditions: a) Before wetting ($24 \text{ h} \leq t < 48 \text{ h}$ – solid lines) and during wetting ($48 \text{ h} \leq t < 72 \text{ h}$ – dashed lines); b) Before wetting ($24 \text{ h} \leq t < 48 \text{ h}$ – solid lines) and after wetting ($72 \text{ h} \leq t < 96 \text{ h}$ – dashed lines).	104
Figure 4-14: Experimental (solid lines) and analytical (dashed lines) temperatures taking the wall surface temperatures in winter conditions as boundary conditions: a) Before, during and after wetting ($25 \text{ h} \leq t \leq 73 \text{ h}$); b) During wetting ($52.5 \text{ h} \leq t \leq 54.5 \text{ h}$); c) Heat fluxes ($25 \text{ h} \leq t \leq 73 \text{ h}$).	105

Chapter 5

Figure 5-1: Sorption isotherm at $T = 296.15 \text{ K}$. The markers represent experimental data.	123
Figure 5-2: Hygrothermal behaviour ($T = 296.15 \text{ K}$): a) Liquid water conductivity/diffusivity; b) Water vapour permeability.	124
Figure 5-3: Position and identification of the thermocouples and corresponding numerical receivers in the cross section of the test specimen (dimensions in m).	125
Figure 5-4: Three-layer OSB (1)/mortar (2)/ICB (3) porous wall: initial and boundary conditions; $L_x = 0.093 \text{ m}$, $L_y = 0.006 \text{ m}$; $d_{\text{OSB}} = 0.018 \text{ m}$, $d_{\text{mortar}} = 0.005 \text{ m}$, $d_{\text{ICB}} = 0.070 \text{ m}$.	126
Figure 5-5: Experimental versus numerical results.	127
Figure 5-6: Evolution of the relative humidity, water content and temperature throughout the cross section of the constructive solution with ICB 0.070 m thick: Case 1 and Case 2.	128
Figure 5-7: Constructive solutions: a) OSB (0.018m)/mortar (0.005m) and ICB (0.070/0.150m); b) Concrete (0.100m)/mortar (0.005m) and ICB (0.070/0.150m).	129
Figure 5-8: OSB constructive solution coated with ICB 0.070 m thick, subjected to Bragança climate: a) Solar heat flux; b) Relative humidity; c) Temperature.	132
Figure 5-9: OSB constructive solution coated with ICB 0.070 m thick, subjected to Seville climate: a) Solar heat flux; b) Relative humidity; c) Temperature.	135
Figure 5-10: OSB constructive solution coated with ICB 0.070 and 0.150 m thick, subjected to Bragança summer climate: a) Relative humidity; b) Water content; c) Temperature.	136

Figure 5-11: OSB and Concrete constructive solutions coated with ICB 0.150 m thick, subjected to Bragança winter climate: a) Relative humidity; b) Water content; c) Temperature.	138
---	-----

Chapter 6

Figure 6-1: Front view of the metal frame and cross section AA (dimensions in mm).....	150
Figure 6-2: OSB specimen: a) OSB boards mounted on the frame; b) Application of the primer; c) Application of the 1st coat of regularisation/waterproofing mortar; d) Application of a fiberglass mesh; e) Appearance of the specimen after the application of the 2nd and 3rd coat of regularisation/waterproofing mortar; f) OSB coated with the ICB.	151
Figure 6-3: Corrugated metal panel assembly: a) Fixation of the corrugated metal panel; b) Application of the primer; c) Corrugated metal panel coated with ICB.	151
Figure 6-4: Omega profiles application: a) Omega profile with primer; b) Frame with the identification of the two steel profiles systems.	152
Figure 6-5: Assembly sequence of the MD ICB onto the omega profiles: a) Application of the bonding mortar to the profiles; b) Application of the bonding mortar to the MD ICB; c) Mechanical fixing.....	153
Figure 6-6: Test suction levels.....	154
Figure 6-7: Sequence of applied pressures during the water-tightness test.....	155
Figure 6-8: Impact test layout: a) Hard body; b) Large soft body.	155
Figure 6-9: Photos and thermographic images of the specimen after the test.....	157
Figure 6-10: Finalized wall before the suction test.	158
Figure 6-11: Suction test after prolonged wetting: a) During wetting b) Final appearance of the panel where it can be seen that there is no mechanical failure.	158
Figure 6-12: Hard body tests impact zones a) Zone A; b) Zone B.	159
Figure 6-13: Soft large body impact test.....	159

Index of tables

Chapter 2

Table 2-1: Summary of the main anomalies found and its probable causes.	14
Table 2-2: Illustration of the main anomalies that were found on the visited buildings.	15

Chapter 3

Table 3-1: Scheme of the measuring points and $\Delta\epsilon_l$, $\Delta\epsilon_b$ and $\Delta\epsilon_d$ results.	40
Table 3-2: Bending strength results.	41
Table 3-3: Apparatus and results for tensile strength perpendicular to faces.	43
Table 3-4: Compressive stress results at 10% strain.	44
Table 3-5: Shear strength results.	45
Table 3-6: Compressive force F_p and $F_{p(5mm)}$ for both ST and MD ICB.	46
Table 3-7: Apparatus for evaluating the deformation under specified compressive load and relative deformation results (ϵ_1 and ϵ_2).	46
Table 3-8: Scheme of the apparatus and water vapour transmission properties.	49
Table 3-9: Water absorption scheme and short (W_p) and long term (W_{lt}) water absorption results.	49
Table 3-10: Apparatus, thermal conductivity in dry state and in reference state after one wetting/drying cycle; moisture content at reference state.	50
Table 3-11: Hydrostatic balance and open porosity p_o and apparent volumetric mass ρ_b	52
Table 3-12: Dry density, apparent density and saturation moisture content, content (mass per mass and mass per volume) of MD ICB.	53
Table 3-13: Compressive results after freeze-thaw test.	65
Table 3-14: Expected relative deformation at the end of 10 years for compressive loads of 30, 40 and 50 kPa.	66

Chapter 4

Table 4-1: Material properties (mean values).	91
Table 4-2: Receiver numbering used in the analytical model.	92

Chapter 5

Table 5-1: Materials' properties: ICB - measured in Chapter 3; OSB, mortar and concrete - WUFI materials database.....	124
---	-----

Nomenclature

Chapter 3

Symbol		Units
a	moisture correction factor	-
A	cross sectional area of the test specimen	m^2
A_w	water absorption coefficient by partial immersion	$\text{kg}/(\text{m}^2 \text{ s}^{0.5})$
b	width	m or mm
d	thickness	m or mm
d_1, d_2	thickness of test specimen measured under load	mm
D_l	liquid water conductivity/diffusivity	s
D_w	liquid transport coefficient	m^2/s
D_{ws}	liquid transport coefficient for suction	m^2/s
D_{ww}	liquid transport for redistribution	m^2/s
e	increment in thickness	cm
F_{10}	force at 10% strain	N, kN
F_m	maximum force	kN
F_p	compressive force at critical point	kN
$F_{p(5\text{mm})}$	compressive force for 5 mm deformation	kN
F_x	force applied at corresponding displacement X	N
g	acceleration of gravity	m/s^2
g_v	water vapour transmission rate	$\text{mg}/(\text{h m}^2)$
G	mean of five successive determinations of $G_{1,2}$	mg/h
$G_{1,2}$	change in mass of the test specimen, for instants t_1 and t_2	mg/h
h	capillary suction height	m
j_l	liquid transport flux density	$\text{kg}/(\text{m}^2 \text{ s})$
l	length	mm
L	span between supports	mm
m	mass	g, kg
m_0	dry mass	g, kg
m_1, m_2	mass of the test assembly at instant t_1, t_2	mg
m_{1f}	mass of the test specimen after the freeze-thaw cycles	g
m_{72}	mass of the test specimen after been immersed 72 h	kg
m_h	mass of the test specimen when immersed in water	g

Symbol		Units
m_i	initial mass	kg
m_{LT}	mass of the test specimen after the long-term water absorption	g
m_{RC}	mass of test specimen at $T = (23 \pm 2)^\circ\text{C}$ and (0.5 ± 0.05) relative humidity	g, kg
m_s	water saturation mass of the test specimen	g
m_{sat}	free water saturation mass	kg
m_t	mass of the test specimen at each weighing	kg
p_{suc}	suction pressure	Pa
p_o	open porosity	%
p	open porosity	m^3/m^3
R_w	water vapour gas constant	$\text{m}^2 \cdot ^\circ\text{C}/\text{W}$
S_d	equivalent air thickness	m
T	temperature	$^\circ\text{C}$, K
t	time	s, h
t_0	time equal to 0 s	$\text{s}^{0.5}$
t_1, t_2	successive times of weighing	h
t_f	final time	$\text{s}^{0.5}$
$u_{23/0.5}$	moisture content at $T = (23 \pm 2)^\circ\text{C}$ and 0.5 ± 0.05 relative humidity	kg/kg
u_{sat}	moisture content mass by mass at free saturation state	kg/kg
u_{RC}	moisture content mass by mass at reference conditions	kg/kg
V	volume of the test specimen	m^3
W	moisture content mass by volume	kg/m^3
W_p	short term water absorption by partial immersion	kg/m^2
W_{per}	water vapour permeance	$\text{mg}/(\text{m}^2 \cdot \text{h} \cdot \text{Pa})$
Wl	water mass loss per hour	g/h
W_{lp}	long term water absorption by partial immersion	kg/m^2
W_{LT}	long term water absorption by total immersion	%
W_m	water absorption after the freeze-thaw cycles	%
W_{max}	maximum water content	kg/m^3
W_p	short term water absorption by partial immersion	kg/m^2
W_{sat}	water content mass by volume at free saturation state	kg/m^3
X_{ct}	compressive creep	mm
X_m	displacement at midway between supports at maximum force	mm

Symbol		Units
Z	water vapour resistance	(m ² h Pa)/mg

Greek symbol		Units
α	moisture factor	-
δ	water vapour permeability	mg/(m h Pa)
δ_{air}	water vapour permeability of the air	mg/(m h Pa)
$\Delta m'0$	value of on the straight line at $t=0$ h	kg/m ²
Δm_t	difference between the mass at each weighting and the initial mass	kg/m ²
$\Delta m'tf$	value on the straight line at the final time	kg/m ²
Δp	pressure variation	Pa
$\Delta \varepsilon_b$	dimensional change in width	%
$\Delta \varepsilon_d$	dimensional change in thickness	%
$\Delta \varepsilon_l$	dimensional change in length	%
$\Delta \sigma_{10,\text{dry}}$	percentage variation of the values obtained for σ_{10} in dry conditions in relation to the initial compression values	%
$\Delta \sigma_{10,\text{wet}}$	percentage variation of the values obtained for σ_{10} in wet conditions in relation to the initial compression values	%
ε_t	relative deformation for a 10-year extrapolation	%
ε_1	relative deformation after step A	%
ε_2	relative deformation after step B	%
$\lambda_{(23/0.5)}$	thermal conductivity at (23±2)°C and 0.5±0.05 relative humidity	W/(m K)
λ_{dry}	thermal conductivity at a dry state	W/(m.K)
λ_{meas}	measured thermal conductivity	W/(m.K)
μ	water vapour diffusion resistance factor	-
ρ_0	density of dry material	kg/m ³
ρ_a	apparent density	kg/m ³
ρ_a	apparent density at reference conditions	kg/m ³
ρ_b	apparent volumetric mass	kg/m ³
ρ_l	liquid water density	kg/m ³
ρ_w	real volumetric mass of water	kg/m ³
σ	standard deviation	-
σ_{10}	compressive stress at 10% strain	kPa
$\sigma_{10,\text{dry}}$	compressive stress at 10% strain in dry condition	kPa

Greek symbol		Units
$\sigma_{10, \text{wet}}$	compressive stress at 10% strain in wet condition	kPa
σ_b	bending strength	kPa
σ_m	compressive strength	kPa
σ_{mt}	tensile strength perpendicular to faces	kPa
σ_x	bending stress	kPa
δ	water vapour permeability	mg/(m h Pa)
δ_{air}	water vapour permeability of air	mg/(m h Pa)
τ	shear strength	kPa
φ	relative humidity	-

Chapter 4

Symbol		Units
c	specific heat	J/(kg K)
c_j	specific heat of the layer j	J/(kg K)
h_j	thickness of the layer j	m
h_l	thickness of the layer l	m
j	identifies the number of the layer	
K_j	diffusivity of the layer j	m ² /s
m	mass	kg
m_0	dry mass	kg
R_{si}	thermal resistance of the inner surface	(m ² K)/W
R_{se}	thermal resistance of the outer surface	(m ² K)/W
t	time	h
T	temperature	K, °C
t_{0b}	temperatures on the bottom of external surfaces	K
t_{0t}	temperatures on the top of external surfaces	K
u	water content mass by mass	kg/kg
V	volume	m ³

Greek Symbol		Units
λ	thermal conductivity coefficient	W/(m.K)
λ_j	thermal conductivity coefficient of the layer j	W/(m K)
λ_{airin}	equivalent thermal conductivity of the inner air layer	W/(m K)

Greek Symbol		Units
λ_{airout}	equivalent thermal conductivity of the outer air layer	W/(m K)
ρ	density	kg/m ³
ρ_0	dry density	kg/m ³
ρ_j	density of the layer j	kg/m ³
ω	frequency	rad/s

Chapter 5

Symbol		Units
A_w	water absorption coefficient	kg/(m ² s ^{0.5})
c_{eff}	effective specific heat per unit volume	J/(m ³ K)
$c_{p,\text{eff}}$	specific capacity per mass	J/(kg K)
c_{pl}	specific heat capacity of liquid water	J/(kg K)
c_{pm}	specific heat capacity of dry material	J/(kg K)
c_{pv}	specific heat capacity of water vapour	J/(kg K)
D_L	liquid permeability of a solid material	s
D_T	moisture transport coefficient	kg/(m s K)
D_{va}	vapour diffusivity in air	m ² /s
D_w	liquid transport coefficient	m ² /s
D_{ws}	liquid transport coefficient for suction	m ² /s
D_{ww}	liquid transport for redistribution	m ² /s
D_ϕ	moisture transport coefficient	kg/(m s)
g	gravitational acceleration	m ² /s
h	capillary suction height	m
h_e	specific latent enthalpy of evaporation or condensation	kJ/kg
h_{lat}	specific latent enthalpy	kJ/kg
j	moisture mass flux	kg/(m ² s)
j_l	liquid water mass flux	kg/(m ² s)
j_v	water vapour mass flux	kg/(m ² s)
ρ	porosity	m ³ /m ³
p_a	atmospheric pressure	Pa
p_l	pore liquid water pressure	Pa

Symbol		Units
p_s	vapour saturation pressure	Pa
p_{suc}	suction pressure	Pa
p_v	water vapour pressure	Pa
q_{lat}	latent heat flux	W/m ²
q_{sens}	sensible heat flux	W/m ²
q_{sol}	solar heat flux	W/m ²
R_w	water vapour gas constant	J/(kg K)
T	temperature	K, °C
t	time	h, s
W	water content mass by volume	kg/m ³
W_{sat}	free saturation water content mass by volume	kg/m ³

Greek Symbol		Units
α	heat transfer coefficient	W/(m ² K)
β_p	vapour transfer coefficient	s/m
δ_o	vapour permeability of the still air	s
δ_p	vapour permeability	s
θ	slope of the sorption isotherm	-
λ_{eff}	effective thermal conductivity	W/(m K)
λ_m	thermal conductivity of dry material	W/(m K)
λ_{mst}	thermal conductivity of the solid matrix	W/(m K)
μ	diffusion resistance factor	-
ρ_l	liquid water mass density	kg/m ³
ρ_m	solid matrix mass density	kg/m ³
ϕ	relative humidity	-

Chapter 1

Introduction

1.1 Context and motivation

There is increasing global concern about climate change and the scarcity of resources. It has been recognised that there is a need to take concrete measures to reduce the effects of human activity that are harmful to the environment, such as the emission of greenhouse gases. It is becoming urgent to promote the use of new products and solutions that are sustainable in environmental and energy terms.

Expanded cork agglomerate has been used for some time as an alternative material to traditional external thermal insulation composite systems. However, its use has not been supported by a detailed technical characterisation. Its mechanical and hygrothermal behaviour when exposed to environmental stresses are unknown. It is also known that the external application of ICB can lead to the occurrence of some anomalies. Therefore, the use of this insulation system needs to be further studied.

This research work is driven by the fact that new systems incorporating ICB as an external insulation without any coating need to be correctly characterised in all aspects (hygrothermal and mechanical), to ensure adequate mechanical performance and durability, and contribute to the energy efficiency of buildings and to a more sustainable construction.

1.2 Objectives

This research work studies the use of uncoated ICB as an exterior wall insulation. The following specific objectives were established:

- to identify constructive solutions and anomalies, their probable causes and potential solutions in existing buildings coated with ICB;
- to study the mechanical and hygrothermal properties of ICB of different densities to ascertain which has the best properties for it to be used as uncoated external insulation;
- to evaluate the behaviour of the material when exposed to solar radiation, freeze-thaw conditions and long-term loads;
- to experimentally quantify the importance of moisture on the thermal performance of a constructive solution coated with ICB, when subjected to rain;
- to numerically model the hygrothermal behaviour of walls coated with ICB;
- to experimentally validate ICB constructive solutions regarding their resistance to external conditions (wind, rain and impact loads).

The work carried out to achieve these goals was based on experimental work that included performing laboratory tests on both the material and system specimens, and on numerical modelling, using analytical solutions and numerical models. The experimental and numerical work was carried out at ITeCons - Institute for Research and Technological Development for Construction Sciences, Energy, Environment and Sustainability, a laboratory that undertakes a large number of experimental tests accredited by IPAC – Instituto Português de Acreditação (member of EA – European Cooperation for Accreditation and ILAC – International Laboratory Accreditation Cooperation). The expanded cork agglomerate was provided by Amorim Isolamentos, a business unit from the Portuguese group Corticeira Amorim.

1.3 Thesis outline

The work described in this dissertation is organised into seven chapters, which contain a survey of some of the buildings already coated with ICB and the definition of the constructive solutions to be studied, the mechanical and hygrothermal experimental characterisation of the material, followed by an experimental and numerical study of the hygrothermal and mechanical behaviour of some of the proposed solutions. Each chapter is an individual unit with its own introduction, conclusions and references, so that they can be read separately.

Chapter 2 presents the study of buildings coated with ICB, surveys existing anomalies and identifies their possible causes. The methods used to fix the ICB boards to the base wall are also analysed. Based on this survey, the constructive solutions to be studied and the most appropriate application methods are presented. General application rules and some maintenance procedures are proposed to ensure the material has a long lifespan.

The fact that the ICB will be included in the constructive system as a coating material means that specific tests are required to assess the mechanical resistance and the hygrothermal behaviour of this material. Chapter 3 focuses on the experimental study of the mechanical properties and the basic hygrothermal properties of two ICB densities (standard density, 90-110 kg/m³, and medium density, 140-160 kg/m³). Several mechanical and hygrothermal tests are described and, based on the results, the most appropriate ICB density for use as an external coating is selected. Once this has been chosen, a comprehensive study of its hygrothermal behaviour is performed. Its drying behaviour is also evaluated. After this, the material's behaviour over time is analysed to assess its durability.

As an external uncoated insulation material, the ICB will be exposed to rain, thus absorbing water. Chapter 4 looks at the importance of moisture in the hygrothermal behaviour of the ICB. For this, a medium density ICB coated OSB wall was experimentally studied under dry and wet conditions, for both steady state and transient summer and winter conditions, using a calibrated hot-box apparatus. A simple analytical model that simulates the heat transfer phenomenon was then used. By comparing the numerical results with those obtained experimentally, the importance of moisture on the thermal behaviour of the solution is quantified.

The hygrothermal behaviour of a concrete and an OSB wall, both coated with medium density ICB, when exposed to real climate data is modelled in Chapter 5. The boundary element method was used to develop a numerical model that takes into account the solar heat flux and this was then used to evaluate the heat and moisture transfer through these walls. First, the properties of the materials were validated by comparing the experimental results described in Chapter 4 with the ones obtained numerically. For comparison purposes, the solar heat flux is not taken into account in the numerical model. The same numerical model was used to evaluate the importance of the short-term variation in relative humidity. Then, to foresee the behaviour of the solution when subjected to different climatic conditions, the hygrothermal behaviour of both walls when exposed to real weather data are modelled, taking into account the solar heat fluxes.

A coating with ICB must ensure aesthetic quality and high functional performance, while securing the protection of the supporting base surface, water-tightness and durability. In Chapter 6, constructive solutions are experimentally evaluated. Test specimens of some of the solutions that were defined in Chapter 2 are built. Suction tests and suction tests after prolonged wetting are performed, as well as impact and waterproofness tests.

Chapter 7 presents a summary of the work carried out and the main conclusions, as well as mentioning research work that could provide continuity for this thesis.

Chapter 2

Buildings Coated with Expanded Cork Boards:
Main Anomalies and General Application
Rules

2.1 Introduction

At present, primary energy demand, CO₂ emissions and the ecological properties of materials are used to quantify the level of sustainability of buildings [1]. The most effective way of reducing heat losses in buildings is through the use of thermal insulation materials, which leads to a decrease in the energy required for heating [2]. This is demonstrated by the larger quantities of thermal insulation materials and thicker layers being used in buildings today. The environmental, public health and physical properties of insulation materials are aspects which play an increasing role in the search for optimal insulation [3]. The choice of insulation material must be made depending on their applicability for each type of building element, as well as on its specific requirements.

Regarding the position of the insulation within the building element, its external application has significant advantages. Once the continuity of the insulation is ensured, thermal bridges are minimised and the thermal inertia is not lost. One of the difficulties however, is to precisely provide solutions which deal with facade singularities, such as doors and windows. There are already some solutions available in the market which provide external application of insulation and attempt to deal with these issues.

One example of external insulation are the ventilated facade systems. An external cover, which can be made in stone, wood, plastic or metal, is applied on a support structure, thus creating a ventilated air layer. The insulation material is bonded to the support wall. The main benefit of ventilated facades is the reduction of the solar gains, which is achieved through ventilation and from the shading provided by the cover layer [4].

Another example is the system known as ETICS, the abbreviation for External Thermal Insulation Composite System. In this system, the insulating layer is typically bonded and fixed mechanically to the outer surface of the wall. A rendering layer is used to protect the insulation from the environment and to ensure water-tightness. This layer needs to ensure a proper water vapour permeability to avoid interstitial condensations. The use of ETICS is becoming more widespread since it is not a costly solution and it allows for low disturbance work, when used as a retrofitting solution in existing buildings. Some of the known weaknesses lie in the susceptibility to cracking, and on the occurrence of biological colonies [5].

As an alternative to ETICS, the use of thermal mortars is growing. These mortars incorporate small granules of insulation materials and are characterised by having thermal conductivities below 0.2 W/(m K) [6]. Since they are applied by projection, a great advantage is the easy application capability in the case of irregular wall surfaces. They are seen as a promising retrofitting solution [7] but with higher thermal conductivity when compared with insulation products.

The finishing layers of these systems are subjected to environmental effects, namely large thermal variations. Thus, the building envelope may easily develop anomalies, due to the combined effect of rain, wind, solar radiation, biological agents, atmospheric pollution and mechanical loads [8]. These factors, combined with poor constructive details, inadequate application and lack of maintenance [9] may lead to cracking, detachment, fastening defects, loss of cohesion and staining [10]. These anomalies, besides the visible aesthetic degradation of the building, are generally associated with high costs repair works and ultimately to loss of building durability. Therefore, improving these technical solutions is considered to be essential [11].

In recent years, the use of uncoated expanded cork boards has appeared as an alternative to the conventional external insulation solutions. These boards are produced using cork granules, a by-product of the cork industry, that are autoclaved at high temperature (approximately 300°C) and pressure (around 40 kPa) [12].

Internationally, expanded cork agglomerate is often referred to, in technical documents, by the acronym ICB (Insulation Cork Board). This material's properties depend greatly on grain size and agglomerate density [13,14]. The material impurity content, like wood particles, is also crucial for the final product quality, since it affects the efficiency of the binding process by impeding the adhesion between the cork granules [15]. The density of the agglomerate depends on how much raw material is introduced into the autoclave. For thermal insulation purposes, the most common densities are the standard material (ST ICB), with density range between $90\text{-}110 \text{ kg/m}^3$, and the medium density ICB (MD ICB), with density range between $140\text{-}160 \text{ kg/m}^3$. The ST ICB is the most often used as insulation material. Due to the intrinsic properties of the product, several designers started applying it to different constructive solutions, offering an opportunity to evaluate the performance of the solution.

It is known that, an adequate design and choice of materials along with correct application can decrease the probability of the occurrence of anomalies. To prevent early degradation and

premature ageing of a building's envelope, the quality of the design and construction is essential [16,17]. Based on an extensive inspection programme, Amaro et al. [18] found that the most common anomalies in ETICS include aesthetic anomalies, due to biological growth, colour changes and runoff marks. Appropriate construction details have been the focus of several researchers. Künzel and Zirkelbach [19], while investigating the hygrothermal behaviour of ETICS applied in wooden structures when subject to different climates, concluded that, in cold and moderate climates, there are no moisture problems if the detailing of joints and openings are well designed and implemented. As stated by Hradil et al. [20], a Swedish experiment with surveys on more than 800 ETICS coated timber buildings, showed that problems stemmed from moisture penetration into the structure, were due to rain infiltrating the joints and to poor connections to windows or doors, caused by poor design or poor workmanship. For these structures to perform satisfactorily, proper planning of the details and good workmanship are both required. Carretero-Ayuso et al. [21], after the analysis of 1374 damages associated with user complaints in Spanish courts, concluded that the main causes of complaints included the lack of supervision, insufficiently skilled labour and inadequate handling of materials. In this context, Silvestre and Brito [22] also proposed creating an inventory of the measures to be implemented in the design, execution and maintenance phases, in order to prevent the occurrence of pathologies in the ceramic tiling of buildings.

The ageing and the accompanying degradation of a building's envelope demands for the development of maintenance actions. Lack of maintenance is indicated by Madureira et al. [10] as one of the causes for most of the frequent anomalies found in the building envelopes (runoff marks, uniform dirt and localized stains). Cleaning techniques are among those actions that may help to preserve buildings [29]. The ageing of external coatings depends, not only on the type of materials used and their properties, but also on the environmental exposure to which they are subjected [25].

Several buildings in Portugal are already coated with ICB. They show a variety of construction technologies (several support structures or base materials, different methods of application, as well as different ICB densities) and are exposed to different climatic conditions. They represent a great opportunity, at this initial stage of this work, to evaluate the performance of externally applied ICB. In order to assess the contribution of each factor in the building's behaviour, a set of existing buildings, subjected to different environmental conditions, with specific base walls, and with different ICB application methods, were selected and visited.

This chapter first presents a detailed survey of the application methods and the anomalies associated with a set of existing buildings coated with ICB. Based on the results of this survey, the main concerns that need to be addressed during the design and application phases were identified. Then, some application methods suited for both new buildings and renovations are presented. These solutions will be the basis for the experimental and numerical studies developed within this work. Moreover, application guidelines and best practice rules for dealing with singularities, such as window to wall, wall to floor, or wall to roof junctions, are presented. Finally, maintenance procedures were proposed and tested.

2.2 Survey of existing buildings coated with ICB

This section presents a survey performed on seven existing buildings coated with ICB. The criteria used to select the buildings for this survey were based on climate zone, year of construction, type of base wall and ICB application method. Technical visits were made in order to determine the application method used during construction and to evaluate existing anomalies. A brief description of each building is given in the following paragraphs.

Pavilhão de Portugal was initially built for Expo 2000, which took place in Hannover, after which it was dismantled and rebuilt in Coimbra (2002), in the Parque Verde do Mondego (Figure 2-1).



Figure 2-1: Concert hall known as *Pavilhão de Portugal*.

Currently, this building works as a concert hall. The climate in Coimbra is cold and damp in the winter months, and hot and dry in the summer months. However, since the building is located on the Mondego riverbank, local moisture levels are high all year round. The building walls are made of metal coated with ICB in the NE, SE, SW and NW facades. ICB has been

applied to the metal panel walls with mechanical fixing. The boards' dimensions are $(900 \times 200 \times 100) \text{ mm}^3$ and they have half-lap joints sealed with silicone.

The **Corkhouse**, intended for use as a non-permanent residence, is located on the outskirts of Esposende, in a cold and damp rural area. Its construction was completed in 2006. The building's opaque envelope walls and sloping roof are completely coated with ICB. The boards' dimensions are $(1000 \times 500 \times 70) \text{ mm}^3$. The vertically aligned boards have been spot bonded to a structure of concrete blocks (Figure 2-2). The main entrance is East oriented.



Figure 2-2: Corkhouse: a) Main entrance of the house (view of both facade and roof covered with ICB); b) Application phase of the ICB boards on the concrete walls.

Quinta do Portal (Figure 2-3) is a winery, built in 2007, which is located in Sabrosa, where summers are hot and winters are cold.

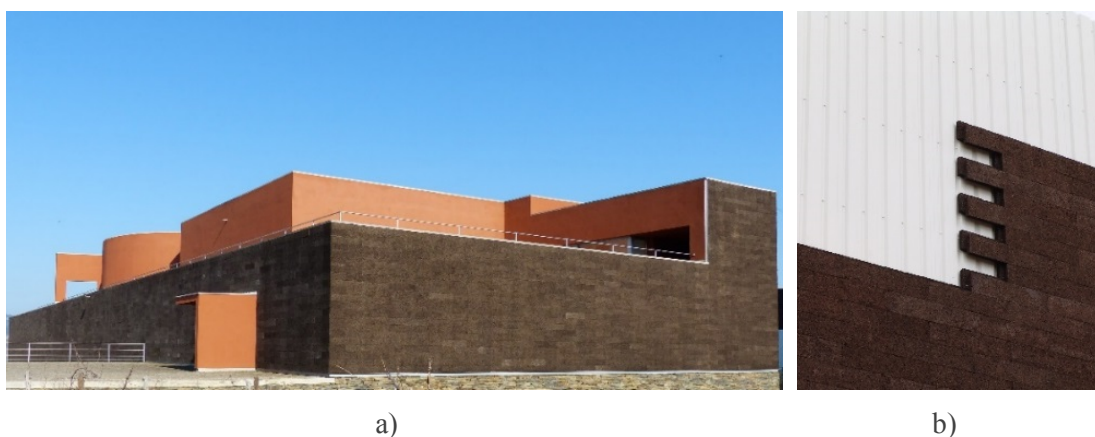


Figure 2-3: Quinta do Portal: a) Overview of the NE and NW facades; b) Application of the ICB boards onto the corrugated metallic panels.

ICB has been mechanically fixed to a corrugated metallic panels structure that involves the concrete structure of the building creating a non-ventilated air layer. The ICB boards are $(1000 \times 250 \times 70) \text{ mm}^3$. The main entrance is oriented to the Northeast.

Ecocabana (Figure 2-4) was built in 2008. It is a small tourist office building, belonging to the Municipality of Cascais (hot summers and mild winters), which is fully coated with ICB (walls and roof). ICB boards with a half lap cut and $(1000 \times 250 \times 95) \text{ mm}^3$ dimensions have been applied to the wooden structure of the building using mechanical fixings.

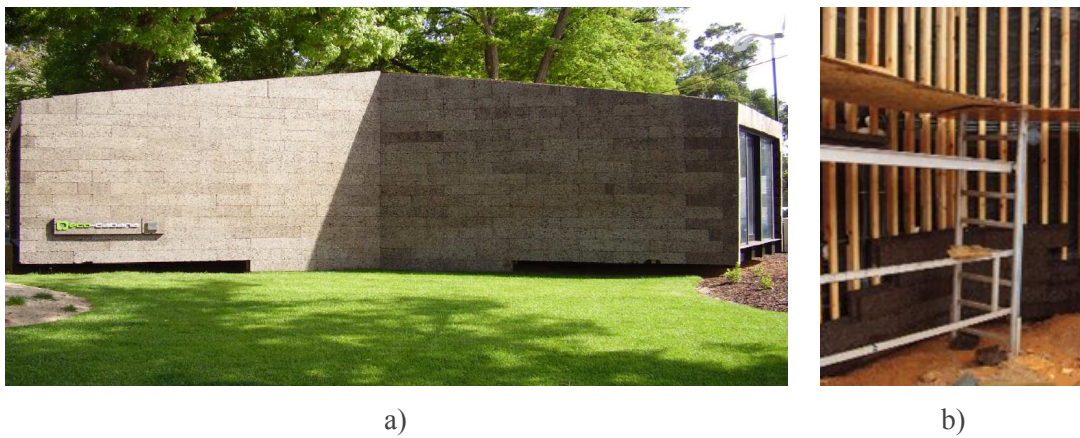


Figure 2-4: Ecocabana: a) Left side of the building; b) Application of the ICB boards onto the wooden frame structure.

Ecorkhotel was built in 2012 and is located near Évora (hot and dry summer, and mild winter with low pluviosity).

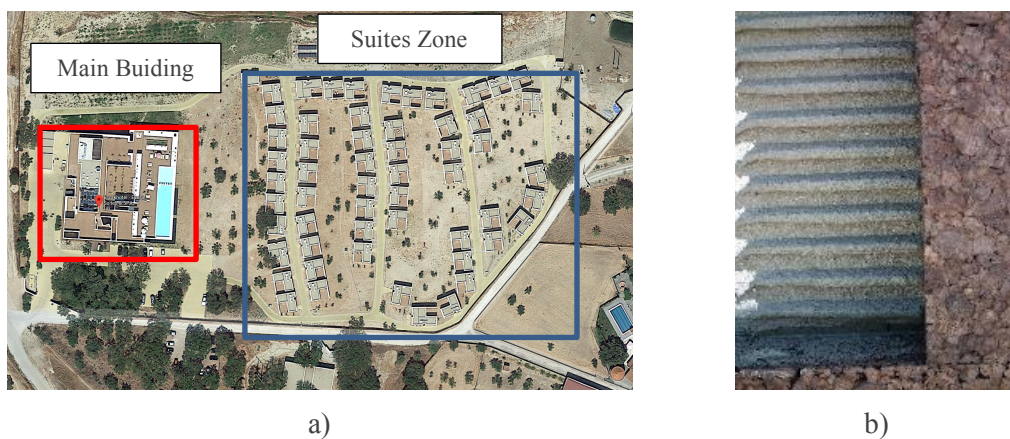


Figure 2-5: Ecorkhotel: a) Location of the main building and the suites area (Google Earth); b) Detail of the bonding phase during the application of the ICB boards.

The complex consists of one main building, with its entrance oriented to the South (Figure 2-5), and several suites, which are separated from the main building and are not coated with

ICB. The main building is mostly coated with ICB boards with dimensions of $(1000 \times 500 \times 60) \text{ mm}^3$, which have been bonded to the concrete building walls.

Logowines is a winery, built in 2012, and located in a rural area near Évora (hot and dry summers, and mild winters with low pluviosity). The ground floor is coated with ICB. The boards have several different sizes, and their thicknesses range from 100 to 400 mm, creating a tri-dimensional effect on the facade. The main facade, shown in Figure 2-6a, makes a 200° angle with the North direction. The ICB boards have been bonded to a concrete masonry wall base, as can be seen in Figure 2-6b.



Figure 2-6: Logowines: a) Overview of the building; b) Method of application of the ICB boards.

The **Surf Centre of Viana do Castelo**, located on the beach of Cabedelo (hot summers, rainy and cold winters), started its activity in 2013.



Figure 2-7: Surf Centre of Viana do Castelo: a) Facade; b) Flat roof.

The building's facades and flat roof are completely coated with ICB, as shown in Figure 2-7. The ICB has been bonded to the concrete walls. The boards' dimensions are (1000×500×80) mm³.

Table 2-1 contains a summary of the main anomalies found during the survey, along with the identification of their probable causes. These anomalies are illustrated in the photographic record provided in Table 2-2.

Table 2-1: Summary of the main anomalies found and their probable causes.

Main anomalies	Probable causes	Illustration Table 2-2
Boards erosion/ high concentration of mosses, lichens and moulds	High concentration of water runoff	a); b); c); d); e)
Disintegration of the material	Inadequate ICB boards density/ poor quality of the material	f); g); h)
Mosses, lichens and moulds	Unperforated base wall profile	i); j)
	Water run-off due to small spaces on the wall capping joints	k)
	Ineffective roof draining system	l)
	Connection to door without any spacing or perforated profile	m)
Open joints	Mechanical fixation without bonding	n); o); p)
Boards detachment	Poor bonding system	q); r); s)
	Mechanical fixation failure	
Damaged boards near the ground	Lack of base wall profile	t)
	Inadequate ICB boards density	u)
Efflorescence on facades	Water flow in the mortar-ICB interface before coming to the wall surface (e.g. due to ineffective roof draining system)	v)
Water infiltration / Moisture condensation	Inefficient waterproofing of the facade or roof	x); z)
	Inadequate hygrothermal behaviour	

Table 2-2: Illustration of the main anomalies that were found.

























 <p><i>Pavilhão de Portugal</i></p> <p>a)</p>	 <p><i>Ecorkhotel</i></p> <p>b)</p>	 <p><i>Logowines</i></p> <p>c)</p>
 <p><i>Pavilhão de Portugal</i></p> <p>d)</p>	 <p><i>Ecorkhotel</i></p> <p>e)</p>	 <p><i>Ecocabana</i></p> <p>f)</p>
 <p><i>Ecocabana</i></p> <p>g)</p>	 <p><i>Pavilhão de Portugal</i></p> <p>h)</p>	 <p><i>Pavilhão de Portugal</i></p> <p>i)</p>
 <p><i>Corkhouse</i></p> <p>j)</p>	 <p><i>Pavilhão de Portugal</i></p> <p>k)</p>	 <p><i>Corkhouse</i></p> <p>l)</p>

Table 2-2: Illustration of the main anomalies that were found (continuation).

 <p>m)</p>	 <p>n)</p>	 <p>o)</p>
 <p>p)</p>	 <p>q)</p>	 <p>r)</p>
 <p>*s)</p>	 <p>t)</p>	 <p>u)</p>
 <p>v)</p>	 <p>x)</p>	 <p>z)</p>

* the lighter boards are new boards applied to replace those which have fallen.

The main conclusions of the survey are listed below:

1. Deficient wall capping will originate water runoff along the surface of the walls. Consequently, proliferation of fungi or mould and erosion of the boards may occur;
2. The roof protection should protrude from the facade and provide continuity to ensure it does not create water runoff areas;
3. Material disintegration may occur when using ICB with low density or low quality;
4. Poor bonding of the boards and/or mechanical fixation failure can lead to detachment;
5. Mechanical fixation with no bonding may result in opening of joints due to the hygrothermal variations of the boards (due to the higher solar radiation, the South quadrant presents greater risk);
6. The boards located lowest to the ground shall be inserted in a base profile to avoid breakage. This profile shall be perforated in order to allow ease of water flow, and thereby preventing accumulation of water and, consequently, the development of mosses;
7. Connections with doors and windows must be made in a way so as to prevent accumulation of water;
8. The climate zone where ICB is being applied will have great influence on its behaviour. Buildings in hot and dry areas are less likely to develop fungi, mosses or lichens, even if there is water accumulation on the ICB;
9. To reduce the possibility of efflorescence on the facade, the drainage of water from the roof to the wall must be avoided (by creation of a physical separation between the roof and the facade boards);
10. Infiltration of water through the walls/roofs can occur if the bonding mortar does not guarantee water-proofing, increasing the risk of condensation.

2.3 General rules of application

ICB, as a coating material, shall provide the building with good appearance, visual and tactile comfort, and ensure durability. Furthermore, ICB must be resistant to weathering (rain, wind and sunlight) and to mechanical stress (compressive, shear and bending loads, among others). An ICB coated constructive solution has to ensure water-tightness, impact load and wind resistance and energy efficiency. These essential requirements will be thoroughly studied throughout this thesis. However, based on the results of the survey analysis presented in the previous section, it is also considered particularly relevant to define adequate ICB coating

application methods for different base walls or support structures. For this definition, watertightness and mechanical stability were the two main requirements considered.

The system's performance is also dependent on how singularities, such as the connection between building elements, are dealt with. Thus, in the following sections, some constructive details of specific building elements and singularities are also presented.

2.3.1 Application methods of the ICB boards

This section presents the application method for different types of base walls or support structures.

- **Direct application on walls**

The constructive solution illustrated in Figure 2-8 represents the direct application of ICB on a wall. The wall can be made from concrete, masonry, adobe or stone. This solution is suited for both new buildings or renovations, provided that the base wall is in good condition. The boards must be assembled so that they are always staggered, as seen in Figure 2-8.

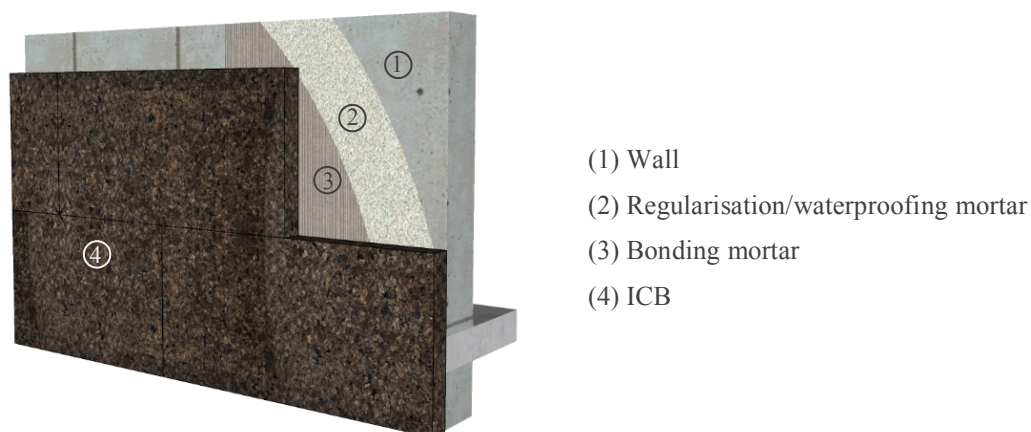


Figure 2-8: ICB application on wall using double bonding.

The first coat of regularisation/waterproofing mortar must be applied to ensure proper water sealing and levelling of the base wall. A second coat, of bonding mortar, is then applied to both the ICB boards (as illustrated in Figure 2-9a) and to the support wall (as illustrated in Figure 2-9b). This procedure, known as double bonding, is highly recommended to ensure mechanical stability. The ICB boards are then laid on the spread mortar, and pressure is applied to ensure a bonding area greater than 60% of the total area.

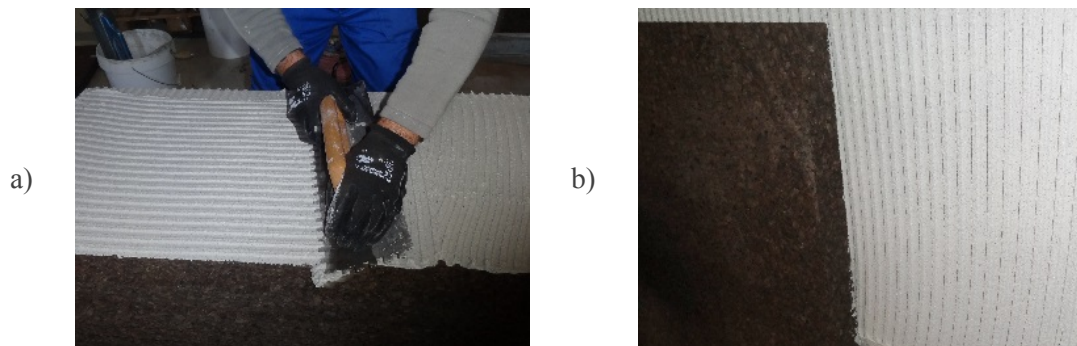


Figure 2-9: Example of double bonding application: a) Spreading of mortar on ICB; b) Spreading of mortar on the wall.

- **Corrugated metal panels**

Corrugated metal panels can be applied in new or existing buildings (namely if the base wall is not in good condition). It is also a suitable solution for roofs, since the metal sheets guarantee water-tightness. Furthermore, an air layer can be created between the base wall and the metal panels, which may be ventilated (Figure 2-10).

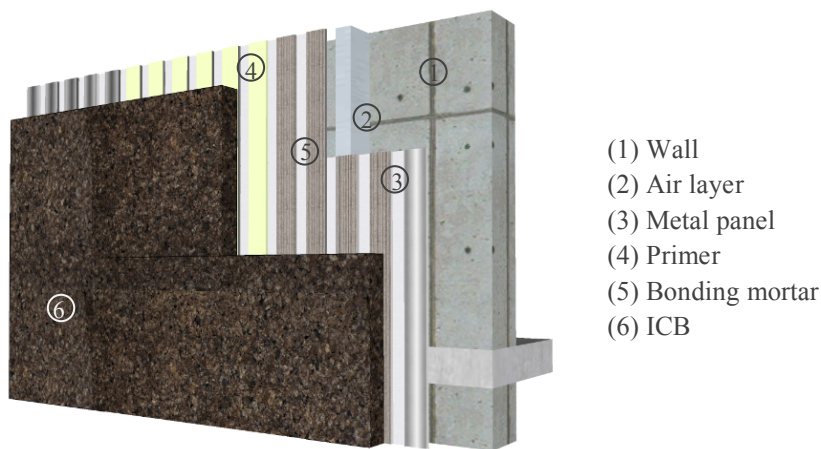


Figure 2-10: Application by using a corrugated metal panel with an air layer.

To minimise the risk of the boards' joints opening, the double bonding method is also recommended. As mentioned before, mechanical fixing alone does not prevent it from happening.

The metal sheets must be coated with a primer beforehand in order to ensure the necessary adherence. The ICB boards must be double bonded. As before, the bonding mortar shall be applied on both the ICB board and the metal.

The top of the wall system shall be adequately covered and sealed. Drainage channels at the bottom of the air layer must be created to ensure that infiltrated water or water from condensation is able to drain out.

- **Steel profile systems**

From a building retrofitting point of view, the possibility of not having to bond the materials is particularly interesting, since the base structure may often be in poor condition (e.g. irregular or degraded surfaces). In such cases, it is necessary to use alternative application methods, such as using discontinuous steel profiles systems (Figure 2-11). Furthermore, ICB application using discontinuous steel profiles creates a slightly ventilated air layer, allowing any rainwater that has infiltrated to dry more quickly since the back of the cork boards are also in contact with the air. Therefore, this solution is also suitable for new buildings located in regions with high moisture levels, which could create problems for ICB.

First, omega profiles are fixed mechanically to the support wall. A primer is applied to the profiles. After the required curing time, the bonding mortar is applied both to the profiles and to the ICB boards, but only to zones in contact with the profiles. Additional mechanical fixing shall be provided by using self-tapping screws.

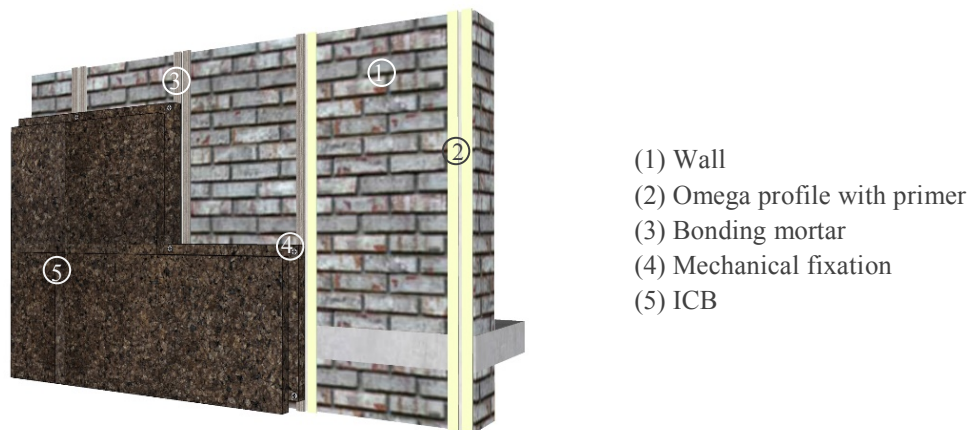


Figure 2-11: Application of the ICB boards by using discontinuous steel profile systems.

The distance between profiles must be defined so as to ensure the mechanical resistance of the system to both wind and impact loads. To define this distance, the proposed solution will be subject to laboratory tests, whose procedures and results are presented in Chapter 6.

- **Wooden boards**

Figure 2-12 shows the method of applying ICB on wooden boards. First, the wooden panels must be adequately sealed. Figure 2-12 illustrates the waterproofing/bonding sequence: a primer is applied to the wooden wall, followed by a first coat of regularisation/waterproofing mortar over which a fiberglass mesh is applied. Then, a second and a third coat of regularisation/waterproofing mortar are applied. Once dry, the ICB boards can be applied by double bonding, as explained previously.

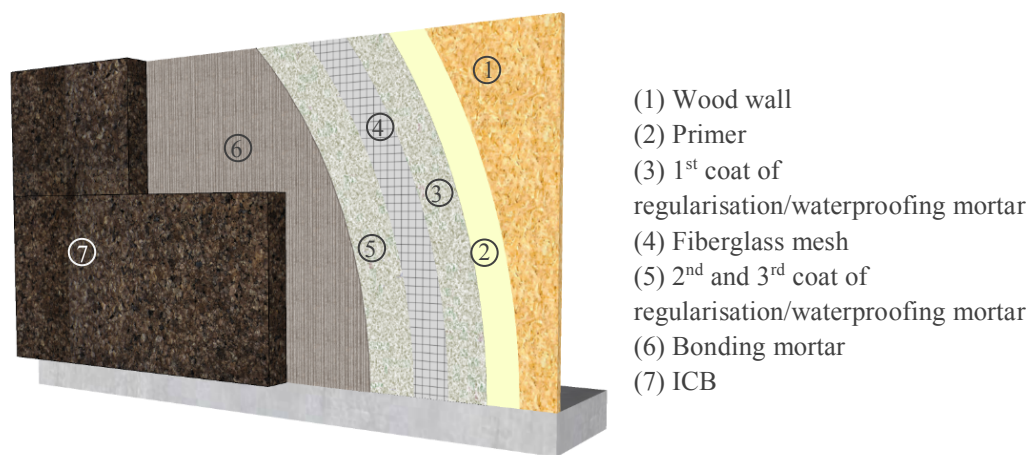


Figure 2-12: Application on wooden panels.

2.3.2 Constructive details of singularities

Besides the methods of applying ICB on to the different base walls, it is necessary to provide solutions for the dealing with the main singularities of the building envelope. The most relevant singularities and corresponding solutions are presented next.

- **Base wall profile**

All types of applications should start with a perforated base profile. Its function is to ensure support and to prevent mechanical damage from accidental impacts. The profile needs to be the same width as the board being used, and must be placed at least 50 mm away from the ground, or 5 mm distance from any other structure. The use of a perforated profile allows for the water that has been absorbed by the ICB (rain water, irrigation systems, etc.) to drain out. Figure 2-13 illustrates the application of the profile.

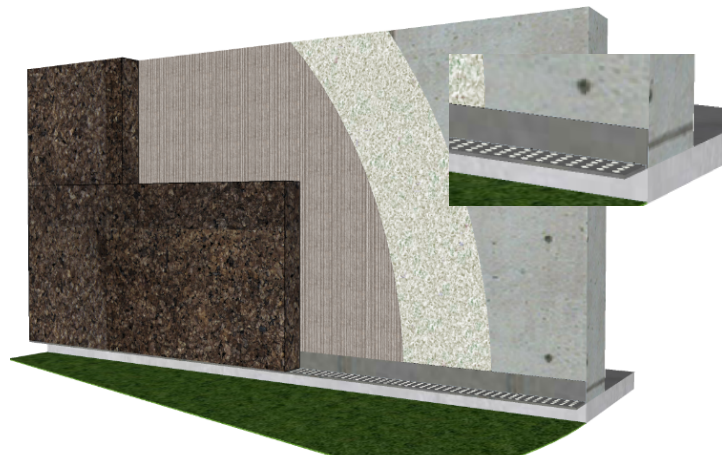
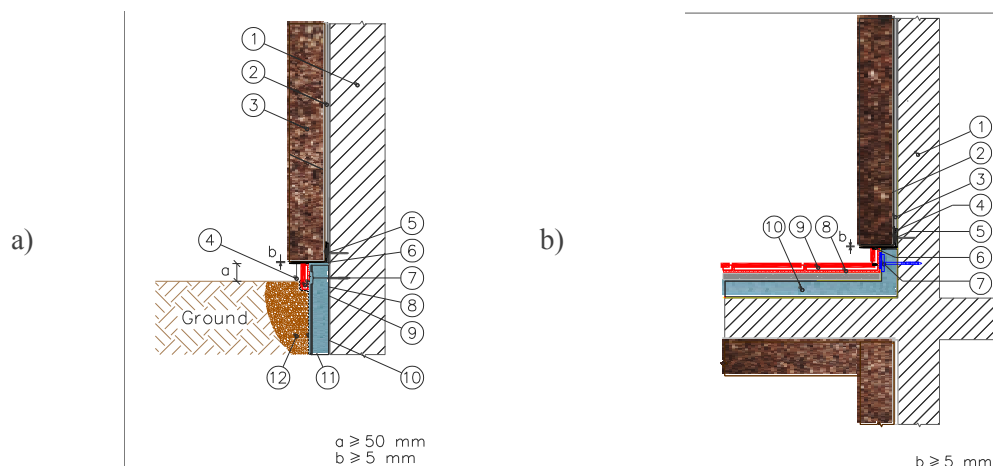


Figure 2-13: Illustration of the use of the perforated base wall profile.

However, in the case of insulation with a different thickness (Figure 2-14a), or with continuous insulation for a balcony or terrace system (Figure 2-14b), the base wall profile cannot be perforated. To avoid accumulation of water in the ICB, a minimum distance of 5 mm must be given between the profile and the first ICB board.



(1) Wall; (2) Waterproofing and bonding mortar; (3) ICB; (4) No perforated base wall profile; (5) Fixing screw; (6) Sealed joint; (7) Facade anchor; (8) Bonding mortar; (9) Ground coating; (10) Insulating board; (11) Studded draining mantle; (12) Draining rainwater curtain connected to collector.

Figure 2-14: Base wall details: a) System starting off the ground - different thicknesses of insulation boards; b) System starting off a balcony or terrace.

• Roof/ facade connection

Capping the walls has significant influence on the appearance of the facade over time. The spacing between the capping plates will originate water runoff in specific zones of the facade,

causing spots, the proliferation of fungi, mould and erosion of the boards. Therefore, the wall capping plates should protrude from the facade (Figures 2-15a and 2-15c) and joints must be sealed (Figure 2-15b).

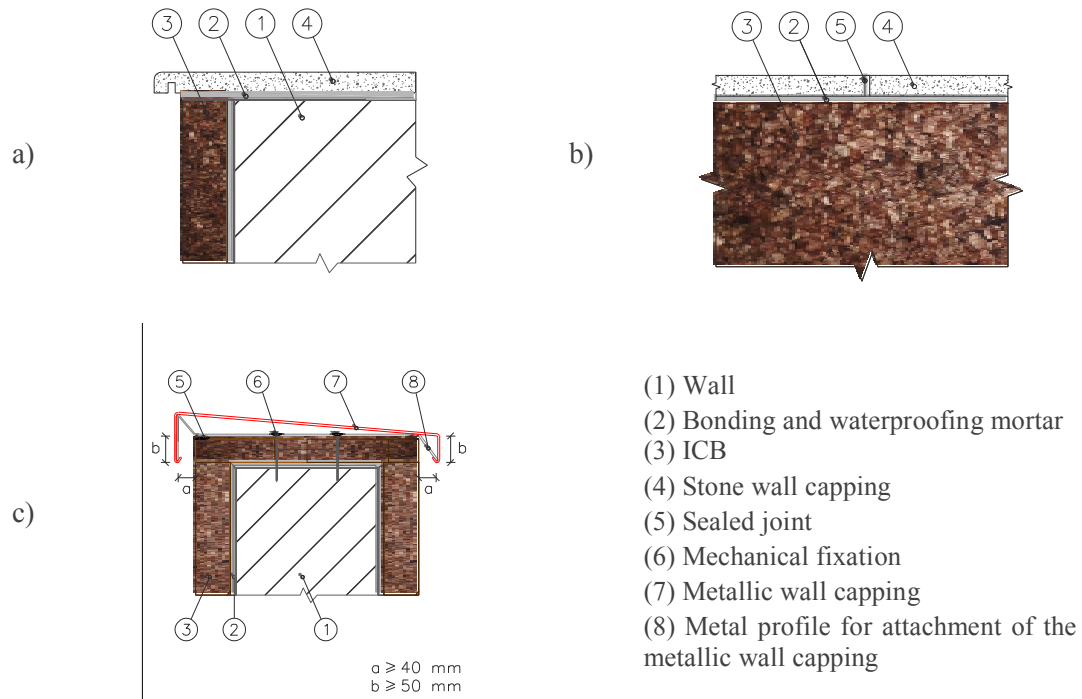


Figure 2-15: Wall capping: a) Top cover cross section; b) Top cover front view; c) Metallic wall capping.

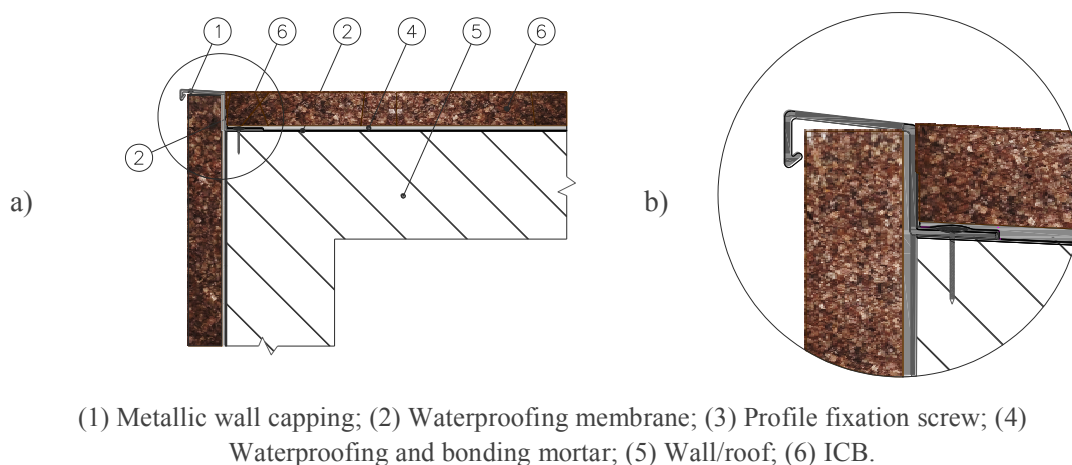


Figure 2-16: Connection facade/flat roof: a) General view; b) Detail of the wall capping application.

Water drainage and consequent salt deposition along the walls (coming from the roof) must be avoided. Thus, if the roof is also coated with ICB, it is recommended to guarantee a physical separation between the facade and the roof boards, as presented in Figure 2-16.

• Corners

Corners are weak singularities that frequently show early degradation. To reduce the likelihood of failure occurring, three main strategies may be followed:

- to build a special ICB one-piece component with a corner design (Figure 2-17a);
- to cut the ICB boards at a 45° angle (Figure 2-17b);
- to apply staggered ICB boards, as illustrated in Figure 2-17c.

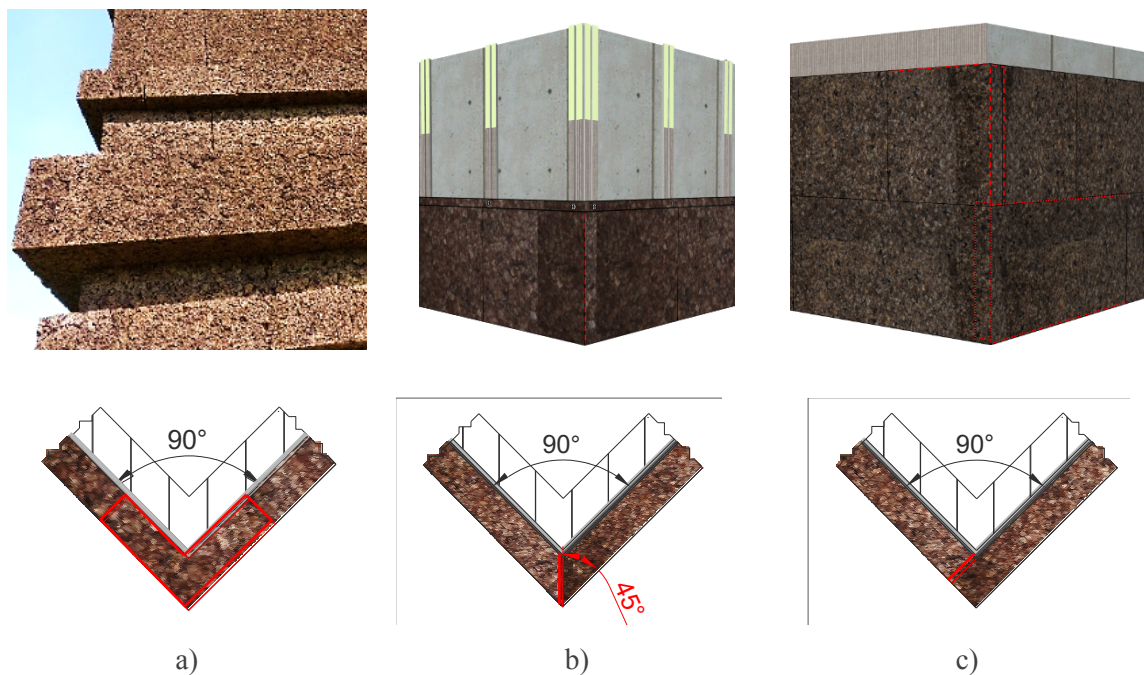
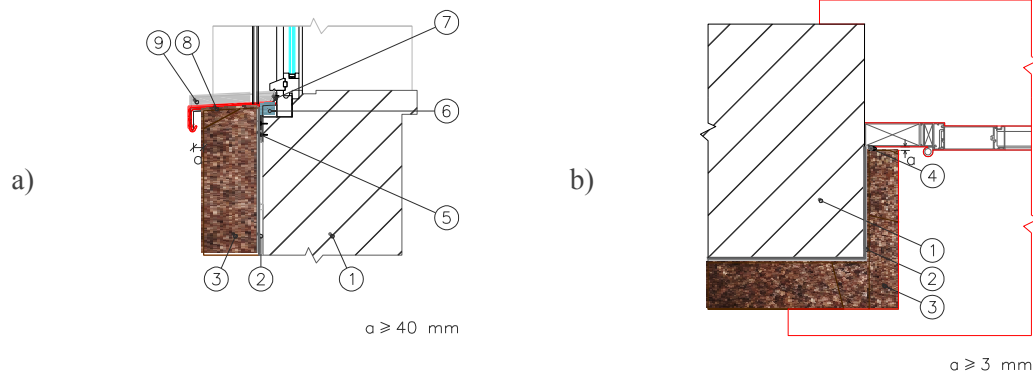


Figure 2-17: Corner connections: a) Special one-piece corner ICB; b) ICB half lap boards cut at 45° and c) Staggered ICB.

• Window (door)/wall junction

The application of a window sill is recommended to avoid the entrance of water directly on top of the ICB boards. The connection of the board with the window sill shall be made as represented in Figure 2-18a.

When connecting to window or door frames (Figure 2-18b), the window or door perimeter must be sealed before applying the ICB. In the head and side jamb, the ICB should be placed 3 mm away from the frame in order to prevent the accumulation of water.

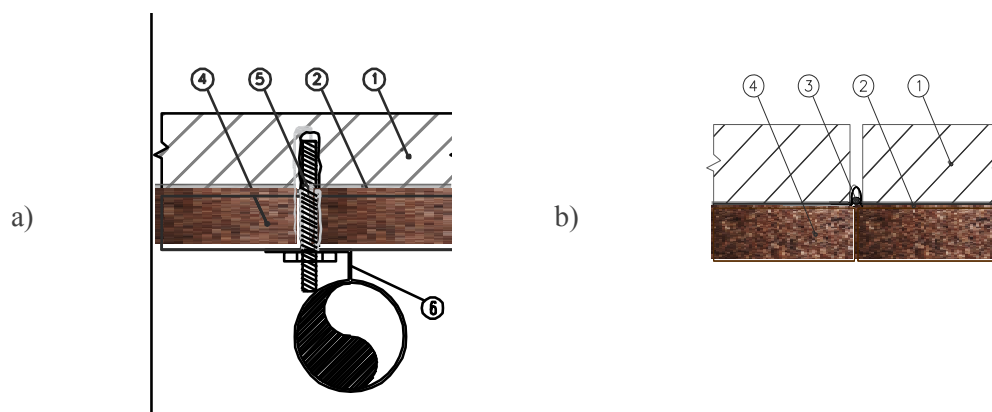


- (1) Wall; (2) Waterproofing and bonding mortar; (3) ICB; (4) Sealed joint; (5) Fixing the metal profile; (6) Insulating board; (7) Connection frame/sill; (8) Metal profiles for sill support; (9) Window sill.

Figure 2-18: Connection with windows: a) Connection with window sill; b) Connections with side jambs.

• Facade elements

Any construction elements that may have to be fixed to the building facade, need to be treated directly at the base wall level since ICB boards do not ensure the required water-tightness.



- (1) Wall, (2) Waterproofing and bonding mortar; (3) Sealed joint; (4) ICB; (5) Threaded rod fixed with plug and sealed; (6) Metal clamp for the downpipe.

Figure 2-19: Elements on facade: a) Attachment elements on the facade (drop tube); b) Expansion joint.

When applying components such as vents or pipes (Figure 2-19a), they have to be sealed directly in the base wall under the ICB board. In the same manner, expansion joints (Figure 2-19b) must be sealed in the base wall

2.4 Maintenance actions

Periodic maintenance procedures will help to preserve the initial visual characteristics of the ICB coated solution. The frequency needed for maintenance will depend on the geographic location of the building and on the orientation of the facade. A building located in a place with high levels of precipitation that may lead to accumulation of water in the ICB, or facades with high levels of surface moisture (e.g. North facing or heavily shaded facades) will have a greater need for maintenance when compared with a building located in a dry place or with facades receiving high levels of solar radiation.

The following section presents suggestions for maintenance procedures in buildings covered with ICB, namely through washing and abrasion techniques.

- **Washing**

Water under pressure can be used to clean facades or roofs which exhibit the accumulation of lichens or mosses (see Figure 2-20a). The pressure of the water shall be controlled in order to avoid damage to the ICB material. For areas of protruding material, such as corners, the use of lower pressure and greater distance from the material is advised.



Figure 2-20: Washing of a wall: a) Moss removal with water pressure; b) Facade appearance after being washed.

Figure 2-20b illustrates the facade after being washed. It is possible to verify that mosses were completely removed.

This test also showed that moss acts as a hydro retainer. When mosses were present, the affected areas did not reach a dry state, even on very hot days. Once removed, these areas became dry. Thus, to prevent degradation of the material in zones with moss accumulation, periodic washing is recommended.

- **Abrasion**

When an ICB coated facade presents overall good condition but colour or surface roughness are the properties that need to be corrected, it is suggested that a slight abrasion of the surface be employed. This abrasion can be done using 230 sandpaper grit. After the abrasive action, the ICB surface must be washed so as to remove all dust. Figure 2-21a presents the appearance of ICB after slight abrasion.

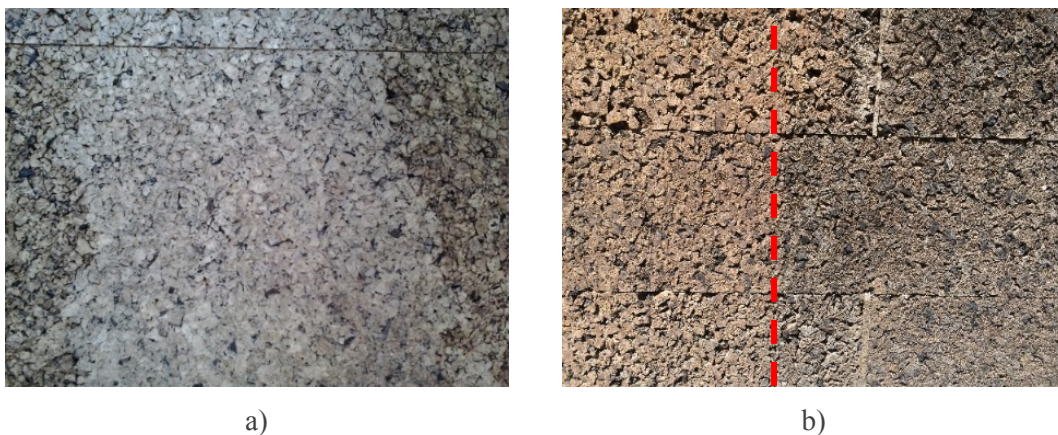


Figure 2-21: Maintenance actions: a) Visual appearance of ICB after being submitted to slight abrasion; b) ICB boards before and after being subjected to deeper abrasion.

If the facade's surface presents considerable changes in colour and texture, as illustrated in Figure 2-21b (right side), a deeper abrasion of the surface may be done by using 80 sandpaper grit. The removal of a thin 1- 2 mm layer of surface should be enough in most situations for the facade to recover its colour and texture. As before, after the abrasion process, the surface shall be washed for total removal of the dust accumulated in the material's pores. As shown in Figure 2-21b, a colour and texture difference is visible when comparing the left and right sides of the ICB surface. The left side corresponds to the final aspect of the treated surface.

2.5 Final remarks

In this chapter, an overview the application methods and anomalies found in existing ICB coated buildings was presented. Inadequate material density and presence of water accumulation or water run-off were found to be the main causes for the anomalies. It should be noted that most of the water-related problems that were found are due to inadequate constructive details. The climate location, as well as the orientation of the building facade has some influence on the material's behaviour. Buildings in hot and dry areas are less likely to develop fungi, mosses or lichens, even if there is water accumulating in the ICB. However, in North facing facades, shaded facades, or buildings located in places with high levels of moisture, fungi, lichens and mosses may develop easily.

To be successful, the ICB application method must be chosen according to the type of base wall and its condition, particularly in the case of retrofitting actions. It was observed that purely mechanically fixed systems can lead to openings in the ICB joints and, therefore, must be avoided. Double bonding using a bonding mortar that guarantees water-tightness and vapour permeability, is highly recommended. For solutions using corrugated metal sheets, discontinuous steel support structures or wooden boards walls, additional techniques are necessary. Metal solutions require an extra layer of primer to ensure adhesion. In the particular case of wooden walls, a careful waterproofing of the base wall shall be made. Several construction details were presented, looking to minimise the occurrence of anomalies. Additionally, some maintenance procedures were tested and presented.

The rules of application and maintenance guidelines that were presented in this chapter can help prevent part of the anomalies that were found in the buildings studied. However, in order to fully evaluate the applicability of the ICB as an external thermal insulation / coating solution, it is necessary to study its mechanical, hygrothermal and durability behaviour, as well as to define the most appropriate material density for use as external cladding. Furthermore, ICB coated constructive solutions must be ensured to be both watertight and permeable to water vapor to guarantee that there is no infiltration of water or surface condensation. They also have to provide good thermal insulation, in both dry and wet conditions, and simultaneously, be resistant to the external aggressions, such as rain, wind and solar radiation. These concerns were the motivation for the subsequent work developed within this thesis, which is presented in the following chapters.

2.6 References

- [1] Jirí Zach, A. Korjenic, V. Petránek, J. Hroudová, T. Bednar, Performance evaluation and research of alternative thermal insulations based on sheep wool, *Energy Build.* 49 (2012) 246–253. doi:10.1016/j.enbuild.2012.02.014.
- [2] F. Pacheco-Torgal, Eco-efficient construction and building materials research under the EU Framework Programme Horizon 2020, *Constr. Build. Mater.* 51 (2014) 151–162. doi:10.1016/j.conbuildmat.2013.10.058.
- [3] A.M. Papadopoulos, State of the art in thermal insulation materials and aims for future developments, *Energy Build.* 37 (2005) 77–86. doi:10.1016/j.enbuild.2004.05.006.
- [4] A. Gagliano, F. Nocera, S. Aneli, Thermodynamic analysis of ventilated façades under different wind conditions in summer period, *Energy Build.* 122 (2016) 131–139. doi:10.1016/j.enbuild.2016.04.035.
- [5] E. Barreira, V.P. de Freitas, External Thermal Insulation Composite Systems: Critical Parameters for Surface Hygrothermal Behaviour, *Adv. Mater. Sci. Eng.* 2014 (2014) 1–16. doi:10.1155/2014/650752.
- [6] M.G. Gomes, I. Flores-Colen, L.M. Manga, A. Soares, J. de Brito, The influence of moisture content on the thermal conductivity of external thermal mortars, *Constr. Build. Mater.* 135 (2017) 279–286. doi:10.1016/j.conbuildmat.2016.12.166.
- [7] A. Brás, F. Gonçalves, P. Faustino, Cork-based mortars for thermal bridges correction in a dwelling: Thermal performance and cost evaluation, *Energy Build.* 72 (2014) 296–308. doi:10.1016/j.enbuild.2013.12.022.
- [8] P.L. Gaspar, J. de Brito, Quantifying environmental effects on cement-rendered facades: A comparison between different degradation indicators, *Build. Environ.* 43 (2008) 1818–1828. doi:10.1016/j.buildenv.2007.10.022.
- [9] I. Flores-Colen, J. de Brito, A systematic approach for maintenance budgeting of buildings façades based on predictive and preventive strategies, *Constr. Build. Mater.* 24 (2010) 1718–1729. doi:10.1016/j.conbuildmat.2010.02.017.
- [10] S. Madureira, I. Flores-Colen, J. de Brito, C. Pereira, Maintenance planning of facades in current buildings, *Constr. Build. Mater.* 147 (2017) 790–802. doi:10.1016/j.conbuildmat.2017.04.195.

-
- [11] E. Barreira, V.P. de Freitas, Evaluation of building materials using infrared thermography, *Constr. Build. Mater.* 21 (2007) 218–224. doi:10.1016/j.conbuildmat.2005.06.049.
- [12] L. Gil, Insulation corkboard for sustainable energy and environmental protection, *Ciência Tecnol. Dos Mater.* 25 (2013) 38–41. doi:10.1016/j.ctmat.2013.12.008.
- [13] O. Castro, J.M. Silva, T. Devezas, A. Silva, L. Gil, Cork agglomerates as an ideal core material in lightweight structures, *Mater. Des.* 31 (2010) 425–432. doi:10.1016/j.matdes.2009.05.039.
- [14] R.T. Jardim, F.A.O. Fernandes, A.B. Pereira, R.J.A. de Sousa, Static and dynamic mechanical response of different cork agglomerates, *Mater. Des.* 68 (2015) 121–126. doi:10.1016/j.matdes.2014.12.016.
- [15] S.P. Silva, M.A. Sabino, E.M. Fernandes, V.M. Correlo, L.F. Boesel, R.L. Reis, Cork : properties , capabilities and applications, *Int. Mater. Rev.* 50 (2005) 345–365. doi:10.1179/174328005X41168.
- [16] N. Neto, J. de Brito, Inspection and Defect Diagnosis System for Natural Stone Cladding, *J. Mater. Civ. Eng.* 23 (2011) 1433–1443. doi:10.1061/(ASCE)MT.1943-5533.0000314.
- [17] M.F.S. Rodrigues, J.M.C. Teixeira, J.C.P. Cardoso, Buildings envelope anomalies: A visual survey methodology, *Constr. Build. Mater.* 25 (2011) 2741–2750. doi:10.1016/j.conbuildmat.2010.12.029.
- [18] B. Amaro, D. Saraiva, J. de Brito, I. Flores-Colen, Statistical survey of the pathology, diagnosis and rehabilitation of ETICS in walls, *J. Civ. Eng. Manag.* 20 (2014) 511–526. doi:10.3846/13923730.2013.801923.
- [19] H.M. Künzle, D. Zirkelbach, Influence of rain water leakage on the hygrothermal performance of exterior insulation systems, in: *Build. Phys. 2008 - 8th Nord. Symp.*, 2008: pp. 253–260.
- [20] P. Hradil, T. Toratti, E. Vesikari, M. Ferreira, T. Häkkinen, Durability considerations of refurbished external walls, *Constr. Build. Mater.* 53 (2014) 162–172. doi:10.1016/j.conbuildmat.2013.11.081.
- [21] M.J. Carretero-Ayuso, A. Moreno-Cansado, J. de Brito, Study of the prevalence of

- critical and conflict-prone points in facades, *Eng. Fail. Anal.* 75 (2017) 15–25. doi:10.1016/j.engfailanal.2016.12.009.
- [22] J.D. Silvestre, J. de Brito, Ceramic tiling in building façades: Inspection and pathological characterization using an expert system, *Constr. Build. Mater.* 25 (2011) 1560–1571. doi:10.1016/j.conbuildmat.2010.09.039.
- [23] M.E. Young, D.C.M. Urquhart, R.A. Laing, Maintenance and repair issues for stone cleaned sandstone and granite building façades, *Build. Environ.* 38 (2003) 1125–1131. doi:10.1016/S0360-1323(03)00084-2.
- [24] I. Flores-Colen, J. de Brito, V.P. de Freitas, Stains in facades’ rendering – Diagnosis and maintenance techniques’ classification, *Constr. Build. Mater.* 22 (2008) 211–221. doi:10.1016/j.conbuildmat.2006.08.023.
- [25] A. Sarja, Bamforth, Caccavelli, J.-L. Chevalier, S. Durucan, M.J. Setzer, *European Guide for Life Time Design and Management of Civil Infrastructures and Buildings - Project Cluster LIFETIME*, Espoo, 2005.

Chapter 3

Expanded Cork Properties

3.1 Introduction

The use of greener insulation products is a strategy that is being followed to achieve more sustainable energy efficient buildings. Insulation materials produced from recycled or natural materials are increasing and they also fit well with the creative methods of eco-design. To be part of the building envelope, such as a facade or roof, it has to be resistant to weathering and mechanical actions and be durable [1].

Both medium and standard density expanded cork board are being used more often as uncoated external facade and roof insulating building systems. Thus, besides the need to guarantee an adequate hygrothermal behaviour its durability must also be ensured by providing enhanced protection from the effects of weathering and from mechanical actions (particularly the weight of fixtures and fittings, and impact loads).

Expanded cork board, which is often alluded to in technical documents by the acronym ICB (insulation cork board), is 100% natural, sustainable and recyclable, once the cork tree regenerates after being stripped [2]. ICB is made of cork granules, a by-product of the cork industry [3,4], that are agglutinated with their own suberin, through the effect of pressure and temperature [5] to form a compact block, which is then cut to the desired thickness. The quantity of the granules inside the autoclave and their compression before the steam process controls the final product density [6]. For thermal insulation purposes, ranges between 90 to 110 kg/m³ (standard density) and 140 to 160 kg/m³ (medium density) are the most used. ICB has a lower carbon footprint than other insulation materials [7]. However, Demertzi et al. [8] concluded that more attention should be paid to the production of the thermal energy used in the agglomeration process and the production of the raw material, *falca*.

ICB is an insulation material that has proved to be resistant to mechanical loads as well as biological and chemical agents. Moreover, under fire conditions it does not release toxic substances as other insulation materials such as polyurethane foams and extruded or expanded polystyrene do [3].

Several factors can affect the mechanical behaviour of cork solutions. Jardin et al. [9] studied the mechanical behaviour (under static and dynamic loading) of different types of cork composites using different grain size and agglutination binders. They showed the influence of those characteristics on the Young's modulus and densification strain results. Díaz-Parralejo et al. [10] investigated the bending strength of expanded cork, concluding that an increased

presence of carbonized and foreign particles noticeably lowers the bending strength of the material. The use of the expanded cork as core material in sandwich panels is quite common and its mechanical characterization for different covering solutions can be found in the literature: Aleppo pine wood veneer [11], fibreglass reinforced polymer [12], carbon [13], and others. However, when used as an insulation material the information on it is very scarce and is mostly confined to densities below 130 kg/m^3 , which are covered by EN 13170:2012+A1:2015 [14].

The hygrothermal performance of the building envelope is a crucial factor in the energy balance and healthy internal conditions of a building [15]. Thus, a thorough knowledge of the properties associated with the moisture and heat flow is needed. Moisture transport within a porous material can take place in the liquid or vapour state. The modes of transport are vapour diffusion, capillary suction or a combination of the two [16]. The material's water vapour transmission properties are critical to the moisture transfer in the vapour phase process [17–21].

Each material has a specific sorption capacity in specific relative humidity and temperature environments. The sorption curve of the material is obtained for different spots of relative humidity for which the material needs to reach the equilibrium. Several processes can be used to achieve the adsorption/desorption curves. ISO 12571:2013 [22] proposes two alternative methods, the desiccator and climatic chamber methods. Several authors adopted the climatic chamber method in their research [18,23–25], however, other approaches can be also found in the literature. Lagorce-Tachon et al. [26] measured the sorption isotherm of natural cork by subjecting samples to relative humidity environments ranging from 0% to 100% in air-tight containers over P_2O_5 solutions, or water at 25°C in order to establish the desired relative humidity. To shorten the time taken to obtain the hygroscopic curves, Feng et al. [27] exposed samples of autoclaved aerated concrete to different relative humidity levels simultaneously. Measurements in transient conditions were performed by Ronzino and Corrado [28] to calculate the vapour permeability and the sorption isotherm of gypsum plaster by automatically weighing the test specimens every 60 seconds for 30 days.

Capillary suction is one of the moisture transport mechanisms in porous materials when the water is in liquid phase. The amount of water that a porous material can absorb when partially in contact with liquid water can be estimated by calculating its water absorption coefficient, A_w [29], and the short-term water absorption, W_p [30], as described in several studies [18,19,31]. The upper limit of the capillary range corresponds to the moisture content

saturation, but it is hard to achieve the maximum water content of a material because the air trapped inside the pores makes it difficult to completely fill them with water [32]. Thus, capillary saturation is always less than the maximum water content [33]. The saturation water content can be obtained by the gravimetric method after full immersion of the test specimens in water, as described in several works on materials like concrete and insulation materials [19,25,34,35].

Several authors emphasize the importance of considering the change in thermal conductivity (λ) with the moisture content of porous building materials because of its impact on thermal behaviour. Several studies [36–40] describe the quantification of the influence of the moisture content on thermal conductivity. Insulating materials have low thermal conductivity due to the embodied gas in the material's mass [41]. If this gas is displaced by vapour or water penetration, the material loses much of its insulation capability because water has higher thermal conductivity [41,42]. Jerman and Černý [19] used a transient method to measure the dependence of the moisture content on the thermal conductivity of some thermal insulation materials and established a quadratic relationship between those properties. Abdou and Budaiwi [43] studied the variation of thermal conductivity of fibrous insulation materials changing the moisture contents up to approximately 45 % by mass. The relationship between thermal conductivity and moisture content was found to be linear. Janetti et al. [44] calculated the contribution of the enthalpy fluxes due to liquid and vapour transfer when performing measurements to obtain the thermal conductivity of calcium silicate specimens. They compared the experimental values of thermal conductivity, obtained using a guarded hot plate apparatus, with the Krisher model results, which include heat conduction and radiation. The study was performed with materials in the dry state and up to moisture saturation state. According to the authors, the difference between these two states are the contributions of the enthalpy fluxes due to liquid and vapour transfer. The measured thermal conductivity is higher than the values given by the model, except for completely dry or saturated samples, since in these cases there is no mass transfer.

The sustainability of building systems is highly dependent on the materials durability [45]. A number of studies have addressed the effects of exposing materials to the effects generated by moisture, solar radiation and freeze-thaw cycles over their lifetime. Knapic et al. [6] studied the high density expanded cork (230 and 290 kg/m³) moisture resistance by means of an ageing test in which 3 freeze-thaw cycles were performed, after which the materials' tensile behaviour was analysed. The authors found that the internal cohesion dropped by an average

of 27% and 36% for the 230 and 290 kg/m³ ICB boards. The effect of freezing-thawing and wetting-drying ageing on the thermal conductivity and compressive response of two plaster and cereal straw (barley and wheat) composites was investigated by Belayachi et al. [46]. The authors noted that the freezing-thawing conditions had no effect on the thermal performance of the two composites. However, the crystallization that took place in the freezing phase caused the deterioration of the micro-tubes, which worsened the barley-straw composite's mechanical response. Klůšeiko et al. [47], studying the effects of freeze-thaw cycles on autoclaved aerated concrete, expanded perlite and calcium silicate insulation, found significant changes in the tensile strength of the autoclaved aerated concrete and the expanded perlite after 53 cycles. Ling et al. [48] subjected autoclaved lime-saline soil bricks to increased freeze-thaw cycles, and noted that there was a trend to higher followed by a lowering of compressive strength as the number of cycles increased.

Solar radiation can also damage building materials, ranging from discolouration to loss of mechanical integrity [49]. Laboratory tests can be used to induce accelerated ageing. One example is the study by Graziani et al. [50] that uses exposure to ultraviolet lamps (UV) and simultaneous UV and wetting/drying cycles to assess the durability of hydrophilicity and self-cleaning ability of TiO₂ nano-coatings applied to a fired clay brick substrate. The authors conclude that although some surface degradation was noticed, the remaining TiO₂ nanoparticles retained practically the same efficiency as before the tests. Derbyshire and Miller [51] irradiated thin strips of scots pine and lime with selected regions of the ultraviolet and visible spectrum. They found that the light exposure could initiate the depolymerisation of lignin and wood surface cell wall constituents.

The ability of the ICB to withstand compressive static loads over long periods is of major importance, particularly if it is intended to use it on roofs supporting heavy equipment such as air handling units. Many authors have studied the effects of creep strain under compressive stress. Mano [52] performed creep tests on natural cork samples under compression, at temperatures between 0 and 50 °C. It was found that a fraction of the strain resulting from creep is preserved permanently, particularly when the load is applied in the axial direction. Gnip et al. predicted the long-term deformability of mineral wool and expanded polystyrene slabs [53,54] under static compressive loads. They concluded that the creep strains for the long-term compressive effects may be predicted based on recorded data using shorter experimental times than those frequently indicated in standards.

To assess the capability of expanded cork boards to be used as uncoated finishing layer of facades, this chapter first presents the experimental evaluation of the mechanical and basic hygrothermal properties of standard (ST) and medium density (MD) ICB. Based on this first set of results, MD ICB was selected for further characterization in terms of thermal conductivity variation with moisture content (in both the hygroscopic and capillary domain), hygroscopic absorption and desorption behaviour, water absorption coefficient, liquid water conductivity/diffusivity variation with moisture, and drying behaviour. Finally, the durability of the MD ICB is evaluated by performing freeze-thaw cycles, ageing tests by exposure to xenon arc-light and a compressive creep test

3.2 Mechanical characterization

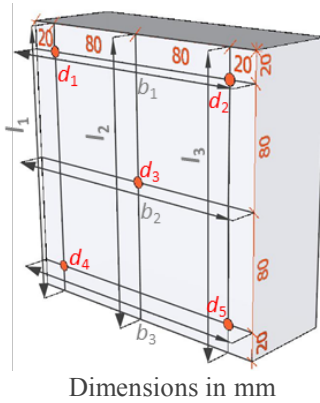
As an external insulating system, the expanded cork boards have to ensure appropriate mechanical resistance to external conditions such as wind, sunlight, rain and impacts. A series of mechanical tests based on EN 13170:2012+A1:2015 [14] were performed on both standard and medium density expanded cork samples to evaluate their mechanical performance.

The experimental procedures that were followed are briefly described in the next sections and the obtained results presented. Each sample is composed of several test specimens. Thus, the mean and the standard deviation, σ , are both presented. The equipment used to perform each test is listed in Annex 1, Table A1.

3.2.1 Dimensional stability under specified temperature and humidity conditions

This test evaluates the dimensional variation in length $\Delta\epsilon_l$, width, $\Delta\epsilon_b$, and thickness $\Delta\epsilon_d$, of the test specimen when subjected to specified conditions of temperature, relative humidity and duration of the exposure, accordantly to EN 1604:2013 [55].

Each sample consists of 3 square test specimens with a nominal side length of (200 ± 1) mm and nominal thickness of 70 mm. The test specimens were conditioned at $T = (23\pm2)$ °C and 0.5 ± 0.05 relative humidity (φ) until constant mass was achieved, and measured in the positions indicated as shown in Table 3-1. After measuring, the test specimens were conditioned for (48 ± 1) h at $T = (70\pm2)$ °C and $\varphi = 0.9\pm0.05$. After this time, they were removed from the climatic chamber and exposed to $T = (23\pm2)$ °C and $\varphi = 0.5\pm0.05$, for further (3 ± 1) h, and measured again. The changes in size are listed in Table 3-1.

Table 3-1: Scheme of the measuring points and $\Delta\epsilon_l$, $\Delta\epsilon_b$ and $\Delta\epsilon_d$ results.

Density	$\Delta\epsilon_l$ [%]	$\Delta\epsilon_b$ [%]	$\Delta\epsilon_d$ [%]
Standard ICB	0.2 (0.071)	0.2 (0.032)	0.3 (0.050)
Medium ICB	0.3 (0.010)	0.3 (0.000)	0.4 (0.058)

The results presented in Table 3-1 indicate that the changes in size are smaller for the ST ICB sample than they are for the MD ICB sample. However, these values are well below to the requirements imposed by EN 13170:2012+A1:2015 [14], which are 1% to $\Delta\epsilon_l$, $\Delta\epsilon_b$, and $\Delta\epsilon_d$. It can be concluded that the material is dimensionally stable, even under moisture conditions.

3.2.2 Bending behaviour

Bending strength indicates a material's ability to withstand mechanical stresses under operating conditions. The bending strength, σ_b [kPa], was determined according to the procedure set out in EN 12089:2013 [56]. It is evaluated by applying a force by means of loading edge moving at a speed of 10 mm/min perpendicular to the test specimen, which is placed on two support edges, until rupture occurs. The displacement at midway between supports (X_m [mm]) and the maximum force due to this displacement (F_m [N]) are measured.

Each sample consisted of 3 test specimens with nominal dimensions of (350×150×70) mm³. The span between the support edges was L=300 mm. The displacements X [mm], and the corresponding forces, F_x [N], are presented in Figure 3-1 for both ICB density samples. It can be seen that the MD ICB exceeds the bending resistance of the ST ICB samples.

The bending stress, σ_x [kPa] is given by the relation $\sigma_x = 3 \times 10^3 \times [(F_x \times L)/(2 \times b \times d^2)]$ (in which b [mm] is the width of the test specimen and d [mm] is its thickness). The bending strength, σ_b [kPa], obtained for the maximum force F_m [N], is presented in Table 3-2.

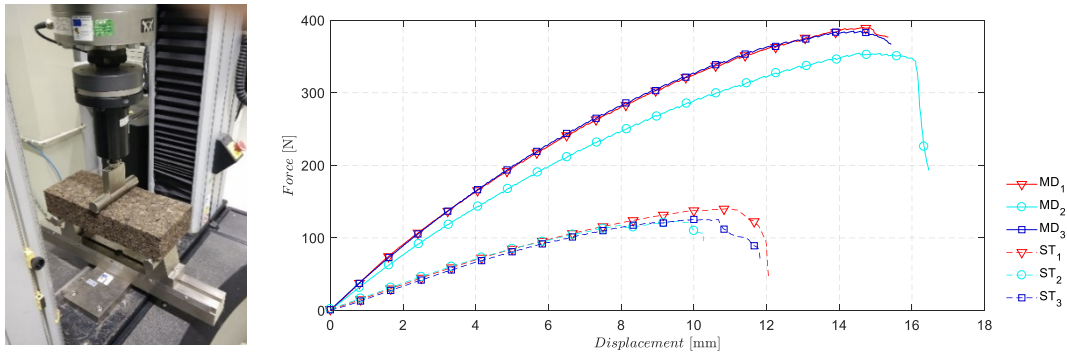


Figure 3-1: Apparatus for bending and force-deflection curves for both ST and MD ICB.

Table 3-2: Bending strength results.

Density	F_m [N]	X_m [mm]	σ_b [kPa]
Standard ICB	129.6	10.26	87.6 (5.90)
Medium ICB	376.6	14.54	227.4 (12.12)

From the results it can be seen that the bending strength of the medium density ICB is 2.6 times higher than that of the standard density ICB samples.

3.2.3 Tensile strength perpendicular to faces: dry and wet conditions

The tensile strength perpendicular to faces, σ_{mt} [kPa], is defined as the maximum tensile force (F_m [kN]) perpendicular to the test specimen faces recorded during the pulling operation, divided by the cross-sectional area of the test specimen (A [m²]). The tensile force is applied at a constant speed of 10 mm/min.

This test was performed for two conditions, dry and wet, to quantify the influence of moisture on the material tensile strength. The test in dry condition was performed according to standard EN 1607:2013 [57]. Each sample consisted of 5 test specimens with nominal dimensions of (100×100×70) mm³.

The wet conditioning was performed following the procedure described in ETAG 004:2011 [58]. Specimens were kept inside climatic chamber at $T = (70 \pm 2)^\circ\text{C}$ and $\phi = 0.95 \pm 0.05$. The

test principle was the same as for dry conditions. Each sample consisted of two sets of 8 specimens. Set 1 was exposed to the required conditions for 7 days and Set 2 for 28 days. Each exposure time was followed by a drying period at $T = (23 \pm 2)^\circ\text{C}$ and $\varphi = 0.5 \pm 0.05$, until constant mass was achieved, after which the tests were performed for both sets.

Figure 3-2 gives the force-displacement curves for Set 1 (Figure 3-2a) and for Set 2 (Figure 3-2b), for both standard and medium density ICB. The force-displacement curves for the dry state have a similar shape to the Set 1 curves (not included here). The ICB boards showed a brittle rupture across the middle of the test specimen.

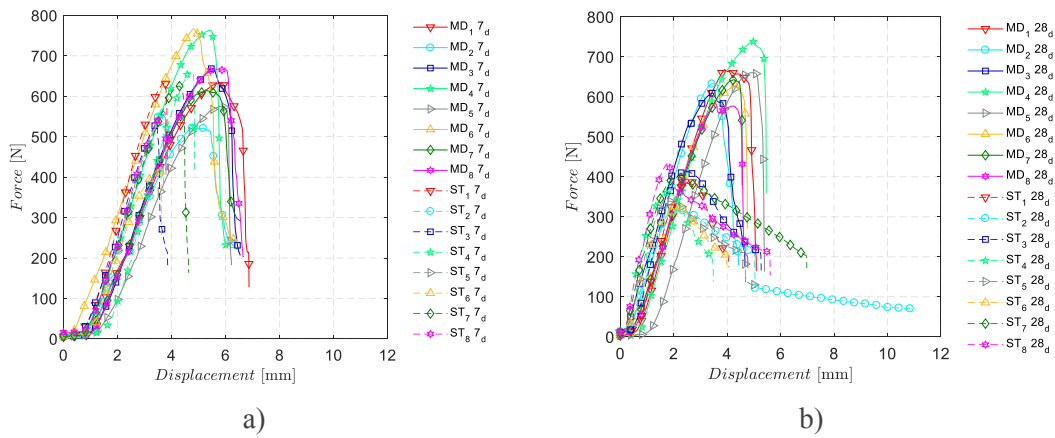


Figure 3-2: Tensile strength perpendicular to faces. Force-displacement curves for ST and MD ICB in wet conditions: a) Set 1: 7 days; b) Set 2: 28 days.

Analysing the results of the Set 1 conditions (Figure 3-2a), it can be concluded that the maximum strength of the ST and MD ICB test specimens is not very different. It should be noted that failure occurs suddenly after reaching the maximum strength. However, for the Set 2, the difference between the two ICB densities is remarkable, with the MD ICB exhibiting a better performance. As before, the MD ICB test specimens exhibit abrupt ruptures. The ST ICB specimens show significantly lower strength resistance but their ruptures are not abrupt. Table 3-3 presents the σ_{mt} results.

The tensile strength perpendicular to faces quantifies the internal bonding strength of the material. The results clearly show that the exposure to higher temperature and moisture induces a degradation on the standard material. The tensile strength of Set 2 is 26.9% lower than the tensile strength in dry condition. But the tensile strength perpendicular to faces of medium density ICB does not change significantly. A decrease of 5.3% in the tensile strength occurred for the Set 2 sample, compared to the dry condition.

Table 3-3: Apparatus and results for tensile strength perpendicular to faces.



Density	Dry σ_{mt} [kPa]	Wet; Set 1 σ_{mt} [kPa]	Wet; Set 2 σ_{mt} [kPa]
Standard ICB	60.7 (8.56)	58.5 (8.57)	44.4 (4.52)
Medium ICB	67.8 (5.37)	64.9 (8.62)	64.2 (4.59)

3.2.4 Compressive behaviour

A compressive force was applied perpendicular to the major faces of the test specimen at a constant speed ($0.1 d/\text{min} \pm 25\%$, in which d is the thickness of the test specimen, in mm). The maximum compressive force at 10% strain was calculated according to the procedures set out in EN 826:2013 [59]. The sample consisted of 3 test specimens with nominal dimensions of $(100 \times 100 \times d) \text{ mm}^3$. Figure 3-3 shows a picture of the apparatus and the force-displacement curves obtained for specimens 50 and 70 mm thick. The 10% strain values, ϵ_{10} , are indicated by vertical lines.

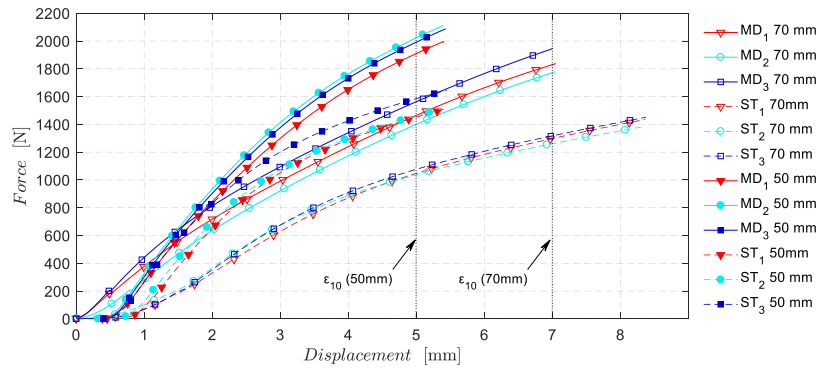
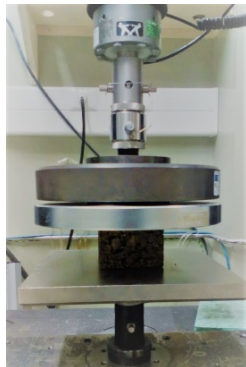


Figure 3-3: Compressive test apparatus and force-displacement curves, for ST and MD ICB, 50 and 70 mm thick.

The compressive stresses at 10% strain, σ_{10} [kPa], are listed in Table 3-4. These results make it possible to conclude that σ_{10} of the MD ICB, for both thicknesses, is considerably higher than for the ST ICB. It can be also be seen that when the thickness increases from 50 mm to 70 mm, σ_{10} falls 9.8% and 14.9% for the MD and ST ICB, respectively. These results suggest that for higher thicknesses and lower densities lower compression forces would be required to achieve 10% deformation.

Table 3-4: Compressive stress results at 10% strain.

Density	Thickness [mm]	σ_{10} [kPa]
Standard ICB	50	154 (6.81)
	70	131 (4.08)
Medium ICB	50	205 (5.98)
	70	185 (6.26)

3.2.5 Shear behaviour

The test specimen is subjected to a shear stress resulting from two parallel forces applied to the main surfaces at a constant speed of 3 mm/min through rigid supports bonded to the material, as indicated in EN 12090:2013 [60]. The corresponding force-displacement curve is obtained. The shear strength, τ [kPa], is defined as the ratio of the maximum force, F_m [kN], applied to the product, which causes rupture along a plane parallel to the direction of the applied force, to the area A [m²] of the plane in which the force acts. Each sample consists of 5 test specimens with nominal dimensions of (250×50×50) mm³.

It is considered that applying a tangential force to the main surface better simulates the stresses imposed on thermal insulation products in many construction applications, particularly walls, than methods such as bending tests.

Figure 3-4 shows the force-displacement curves and the shear test apparatus.

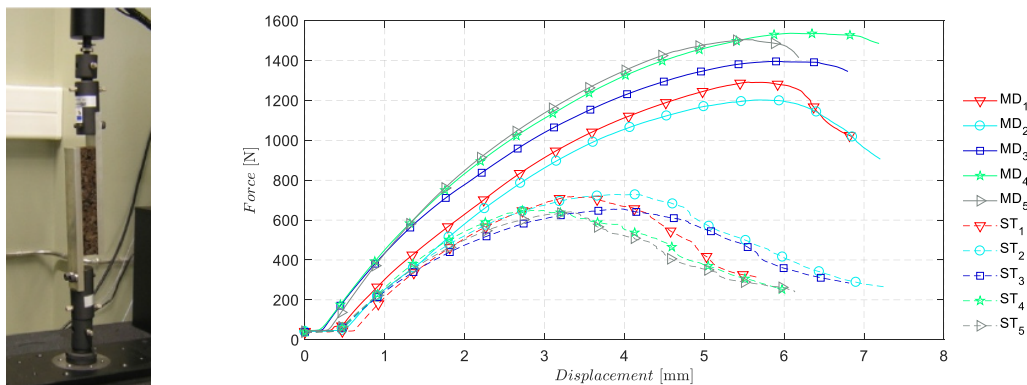


Figure 3-4: Shear test apparatus and force-displacement curves for the ST and MD ICB.

As before, the ST ICB test specimens show lower resistance. Complete rupture occurs after suffering a large deformation.

The results in Table 3-5 show that the shear strength of a medium density ICB is more than 2.0 times higher than that of the standard density sample.

Table 3-5: Shear strength results.

Density	Maximum force F_m [kN]	τ [kPa]
Standard ICB	0.69 (0.04)	55 (3.13)
Medium ICB	1.36 (0.14)	112 (10.82)

3.2.6 Behaviour under point load

A point load was applied with an indenter at (50 ± 5) mm/min in an axial direction perpendicular to the major faces of a square cross section of the test specimen while the force-displacement curve was recorded. The compressive force at the critical point, F_p [kN], is defined as a point on the force-displacement curve where a straight line forming a tangent to the curve separates from the curve. Additionally, the point load for a 5 mm deformation was recorded (as stated in EN 13170:2012+A1:2015 [14]). The test procedures set out in EN 12430:2013 [61] were followed. Each sample consisted of 5 test specimens with nominal dimensions of $(300 \times 300 \times 70)$ mm³.

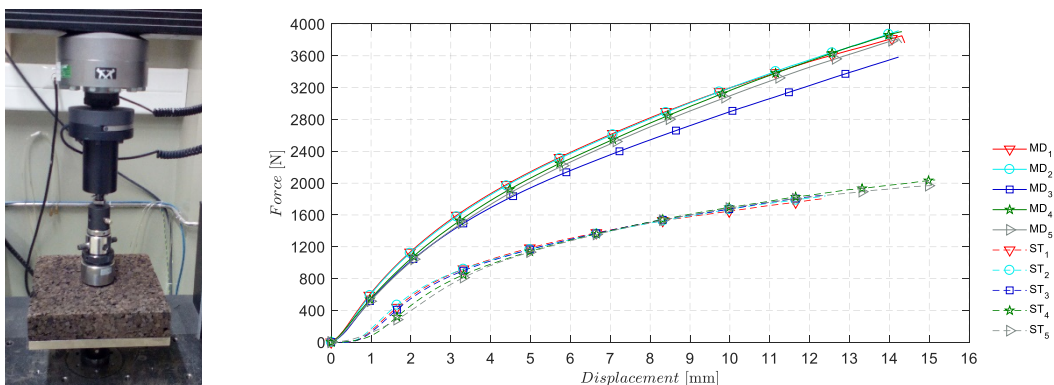


Figure 3-5: Point load apparatus and force-deformation results for the ST and MD ICB.

Figure 3-5 presents the force-deformation curves until a 20% deformation was obtained, while Table 3-6 gives the test results.

Table 3-6: Compressive force F_p and $F_{p(5mm)}$ for both ST and MD ICB.

Density	F_p [kN]	$F_{p(5mm)}$ [kN]
Standard ICB	0.63 (0.13)	1.17 (0.02)
Medium ICB	0.93 (0.06)	2.06 (0.07)

MD ICB compressive force at critical point, F_p , is 48% higher than for the ST sample and, for a 5 mm deformation, the compressive force is 76% higher than that for ST ICB. The results show that the MD ICB is more resistant to compressive point loads, which can be a relevant advantage if it is used in roofs subjected to loads generated by heavy equipment.

3.2.7 Deformation under specified compressive load and temperature conditions

The test consists of applying a compressive stress of 20 kPa to the specimens, as described in EN 1605:2013 [62]. The relative deformation under load is measured in two steps, with the temperature and test duration being changed. First the test specimen is loaded at $T = (23 \pm 5)^\circ\text{C}$ for (48 ± 1) h. At the end of this time the thickness of the test specimen, d_1 [mm], is measured under load and the first deformation, ε_1 , calculated. Then the test specimen is loaded at $T = (80 \pm 1)^\circ\text{C}$ for (48 ± 1) h, and its thickness, d_2 [mm], measured again under load, along with the second value of deformation, ε_2 . The sample consists of 3 test specimens with nominal dimensions of $(100 \times 100 \times 70)$ mm³. The results are presented in Table 3-7.

Table 3-7: Apparatus for evaluating the deformation under specified compressive load and relative deformation results (ε_1 and ε_2).

Density	ε_1 [%]	ε_2 [%]
Standard ICB	0.302 (0.015)	6.844 (0.661)
Medium ICB	0.949 (0.065)	4.630 (0.257)

As seen in Table 3-7, the ST ICB has lower deformation than the MD ICB when exposed to a lower temperature. When the temperature increases to $T = 80\text{ }^{\circ}\text{C}$, the deformations are much larger and the highest value of relative deformation (6.844%) is achieved by the ST ICB. It can be concluded that MD ICB performs better when exposed to compressive loads at high temperatures, which can occur on external roof applications.

3.3 Hygrothermal properties

As the expanded cork boards will be exposed to rain it is important to understand the effect of moisture on the hygrothermal properties. In a first stage, the water vapour transmission properties, short and long-term water absorption and the thermal conductivity of both material densities were evaluated.

These results and the mechanical results show that the MD ICB is more suitable for use as external insulation. Therefore, a more comprehensive study of MD ICB hygrothermal properties was performed. Its porosity, density and saturation water content were measured. In the capillary range, the thermal conductivity (λ_{meas}) of MD ICB was measured as a function of its moisture content. In the hygroscopic range, the adsorption curve, defined as the curve established in a series of increasing equilibrium relative humidity at a given temperature, and the desorption curve, defined as the curve established in a series of decreasing equilibrium relative humidity at a given temperature, were drawn. So that the hygrothermal behaviour of the material could be fully characterized, its water absorption coefficient and liquid water conductivity were determined and its drying behaviour studied.

The next sections describe the samples and the procedures used to perform each test. As before, the equipment used is listed in Annex 1, Table A2.

3.3.1 Basic properties (standard and medium density)

3.3.1.1 Water vapour transmission properties

The procedures recommended by EN 12086:2013 [63] were followed. Each sample consisted of 5 test specimens with nominal dimensions of $(100 \times 100 \times 40)\text{ mm}^3$. The test specimens were conditioned for 24 h at $T = (23 \pm 2)\text{ }^{\circ}\text{C}$ and $\phi = 0.5 \pm 0.05$. They were then fitted into the open end of a container which contained a desiccant (see figure in Table 3-8) and sealed laterally. The relative humidity inside the container was $\phi = 0.025$. The device was placed in a test

atmosphere of $T = (23 \pm 1)^\circ\text{C}$ and $\varphi = 0.5 \pm 0.03$. The difference in the partial pressure of water vapour between the interior of the container and the atmosphere generated a water vapour flow through the test specimen. Silica gel was the desiccant used. The thickness of the air layer between the test specimen and the silica gel layer was 20 mm. The flow occurred downwards.

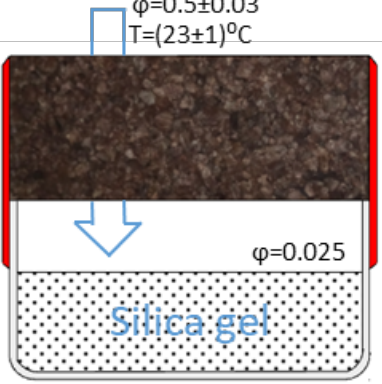
Mass was determined at 24 h intervals to calculate the water vapour transmission rate (g_v) [$\text{mg}/(\text{h m}^2)$] and ensure that the steady state was reached. g_v is obtained from the relation between the mean value of the last five successive determinations, G [mg/h] and the exposed area A [m^2]. The value of g_v is evaluated after five consecutive determinations of $G_{1,2}$ lie within $\pm 5\%$ of G , where $G_{1,2} = (m_2 - m_1)/(t_2 - t_1)$, in which m_1 [mg] is the mass of the test assembly at instant t_1 , m_2 [mg] is the mass of the test assembly at instant t_2 and t_1, t_2 [h], are successive weighing times.

The mathematical manipulations of the water vapour transmission measurements, g_v , yield other commonly used properties. The water vapour permeance, W_{per} [$\text{mg}/(\text{m}^2 \text{ h Pa})$], is given by the relation $W_{\text{per}} = G/(A \times \Delta p)$ in which Δp [Pa] takes the value of 1210 Pa. The water vapour resistance, Z [$(\text{m}^2 \text{ h Pa})/\text{mg}$], is the inverse of the permeance W_{per} . The water vapour permeability, δ [$\text{mg}/(\text{m h Pa})$], is the product of the permeance W_{per} and the thickness of the test specimen, d [m]. The water vapour resistance factor μ , is a dimensionless parameter used to evaluate the water vapour permeability of building materials in comparison to the unitary value assigned to air. It is given by $\mu = \delta_{\text{air}}/\delta$, in which δ_{air} is the water vapour permeability of air ($\delta_{\text{air}} = 0.71 \text{ mg}/(\text{m h Pa})$) as stated in EN 12086:2013 [63], for a registered test barometric pressure of 100.8 kPa). The equivalent air layer thickness S_d [m] represents the equivalent air thickness characterized by the same resistance to water vapour diffusion of the analysed material and is obtained by multiplying the μ value by the material thickness d .

The results are given in Table 3-8.

Regarding the water vapour transmission properties, it can be concluded that the ST ICB performs better than the MD. However, comparison with the μ value of other commonly used insulation materials indicates that medium density vapour permeability values are within the range exhibited by such insulation materials (for example $\mu_{\text{EPS}} = 20\text{-}100$ and $\mu_{\text{XPS}} = 80\text{-}250$ [64]).

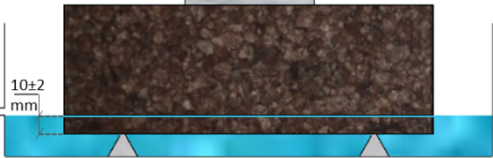
Table 3-8: Scheme of the apparatus and water vapour transmission properties.

	Property	Standard ICB	Medium ICB
	g_v [mg/(h m ²)]	813.64 (76.36)	455.54 (34.79)
	W_{per} (mg/(m ² h Pa))	0.58	0.33
	Z [(m h Pa)/mg]	1.73	3.09
	δ [mg/(m h Pa)]	0.04	0.01
	μ [-]	20.50	54.61
	S_d [m]	1.23	2.19

3.3.1.2 Short and long-term water absorption by partial immersion

The test consisted of placing a test specimen in the water tank and adding water until the bottom face of the test specimen was (10 ± 2) mm below the surface of the water. It was kept like that for a period of 24 hours for the short-term absorption test (W_p), and for 28 days for long-term absorption test (W_{lp}), after which time the weight change was determined. The procedures recommended by EN 1609:2013 [30] and EN 12087:2013 [65] for short- and long-term water absorption, respectively, were followed. For the long-term water absorption, as it is intended to evaluate the water absorption profile, the test specimens were not drained. Each sample consisted of 3 test specimens for short-term and 4 for the long-term water absorption, with nominal dimensions of $(200 \times 200 \times 70)$ mm³. The results are presented in Table 3-9.

Table 3-9: Water absorption scheme and short (W_p) and long term (W_{lt}) water absorption results.

	Density	W_p [kg/m ²]	W_{lp} [kg/m ²]
	Standard ICB	0.34 (0.03)	1.41 (0.079)
	Medium ICB	0.18 (0.01)	0.81 (0.021)

Thermographic images confirm a low capillary effect during the water absorption test for both ICB densities. The specimens did not present a high level of moisture above the water level, although the standard density shows a slightly higher moisture level than the medium density specimens, which is consistent with the results presented in Table 3-9. It can be said that the long-term water absorption will not pose a problem in real use situations.

3.3.1.3 Thermal conductivity at dry and reference state

The thermal conductivity at reference state ($T = 23\text{ }^{\circ}\text{C}$, $\varphi = 0.5$) was obtained after one wetting/drying cycle, as follows: test specimens were first immersed in water at $T = (23 \pm 2)\text{ }^{\circ}\text{C}$; after 72 h, the test specimens were removed from the water and dried at $T = (70 \pm 2)\text{ }^{\circ}\text{C}$ in a ventilated oven until constant mass was achieved, as indicated in EN 13149:2013 [14]; the test specimens were removed from the oven and cooled in a desiccator with silica gel until the temperature fell below $T = 40\text{ }^{\circ}\text{C}$; each board was weighed and its dry mass, m_0 [kg], recorded; the thermal conductivity in dry state, λ_{dry} [W/(m K)] was evaluated, using the heat flow meter (HFM) method; they were then placed in the climatic chamber at $T = (23 \pm 2)\text{ }^{\circ}\text{C}$ and $\varphi = 0.5$ until constant mass was achieved (the relative change in moisture cannot change by more than 0.5% between two consecutive weekly measurements [14]); each board was weighed and its mass at reference conditions, m_{RC} [kg], recorded; the moisture content mass per mass at reference conditions, was calculated by the relation $u_{\text{RC}} = (m_{\text{RC}} - m_0)/m_0$ [kg/kg]; each test specimen was then wrapped in a thin plastic film to prevent any change in moisture and its thermal conductivity at reference state, $\lambda_{(23/0.5)}$, measured.

The standard and medium density ICB samples consisted of 15 test specimens, with nominal dimensions of $(300 \times 300 \times 70)\text{ mm}^3$.

The thermal conductivity in dry and in reference state and the moisture content for reference state are presented in Table 3-10. From the results it can be concluded that the moisture content affects the ST boards more deeply than the MD boards. An increment of 5.1 % in the mean value of λ for the ST boards was observed, while for MD boards, λ rises only 1.5%. It can also be seen that the thermal conductivity provided by MD ICB test specimens is higher than that for ST ICB.

Table 3-10: Apparatus, thermal conductivity in dry state and in reference state after one wetting/drying cycle; moisture content at reference state.



Density	λ_{dry} [W/(m K)]	u_{RC} [kg/kg]	$\lambda_{(23/0.5)}$ [W/(m K)]
Standard ICB	0.037 (0.0005)	0.025 (0.001)	0.039 (0.0005)
Medium ICB	0.041 (0.0013)	0.022 (0.001)	0.042 (0.0014)

Based on the results of $\lambda_{(23/0.5)}$, it can be concluded that it will be necessary to increase the thickness of the MD ICB boards in relation to the thickness of the ST boards, to guarantee the same thermal resistance as the ST boards, $e > 0.077d$. For example, up to 13 cm ST board thickness, less than 1 cm increment in the MD board thickness will provide a better thermal resistance than that given by ST boards.

3.3.2 Comprehensive study of medium density ICB hygrothermal properties

Based on the mechanical and the basic hygrothermal properties of the MD and ST ICB determined above, it can be concluded that all the mechanical properties of MD ICB far exceed the values for the standard material, without substantial loss of the hygrothermal performance. Thus, it can be concluded that MD ICB is more suitable for use as external insulation than ST ICB. A more detailed study regarding the hygrothermal properties of the medium density ICB was then performed to evaluate the behaviour of the material when exposed to moisture in the liquid or vapour state.

3.3.2.1 Open porosity

Open porosity is a very important factor in natural thermal-insulation materials [17] as it has an important role in the moisture movement [66]. The procedures described in NP EN 1936:2008 [67] were followed to calculate the open porosity, which is the fraction of the volume that is occupied by fluid in the interconnected porous network. The test specimens (nominal dimensions of $(150 \times 150 \times 60)$ mm³) were dried until constant mass and their dry mass, m_0 [g], recorded. The test specimens were then placed in the vacuum tank and the pressure lowered gradually to (2.0 ± 0.7) Pa. This pressure was maintained for (2 ± 0.2) h so that the air within the open pores was completely removed. Distilled water at $T = (20 \pm 5)$ °C was slowly introduced so that the test specimens were completely immersed for more than 15 minutes. The low pressure was maintained during filling. When all samples were immersed, the atmospheric pressure inside the container was restored. The test pieces were kept immersed for 24 h, after which each was weighed in a hydrostatic balance. The mass, m_h [g] was recorded and then each test specimen was removed from the water, quickly cleaned with a damp cloth and its saturation mass, m_s [g] recorded. The open porosity was then calculated as a percentage using the relation $p_o = ((m_s - m_0)/(m_s - m_h)) \times 100$, and its apparent volumetric mass was calculated using the expression $\rho_b = (m_0/(m_s - m_h)) \times \rho_w$

[kg/m³], in which ρ_w is the real volumetric mass of water and equal to 997.6 kg/m³, at $T=20^\circ\text{C}$.

The sample consisted of 6 test specimens. Table 3-11 presents the test results.

Table 3-11: Hydrostatic balance and open porosity p_o and apparent volumetric mass ρ_b .



p_o [%]	ρ_b [kg/m ³]
9 (0.31)	160 (3.73)

The maximum moisture content of the medium density expanded cork, $W_{\max}=89.78\text{ kg/m}^3$, can be obtained from these results by multiplying the value of the porosity ($p=0.09\text{ m}^3/\text{m}^3$) by ρ_w .

3.3.2.2 Dry density, apparent density and saturation moisture content.

The apparent density, ρ_a , defined as the material density at reference conditions and the density in dry conditions, ρ_0 were evaluated. The sample consisted of 15 test specimens with (300×300×70) mm³ nominal dimensions.

A capillary-active material in contact with water will absorb water until it reaches its free saturation. This water content, W_{sat} [kg/m³], corresponds to the moisture storage at $\varphi=1$ [68]. For this purpose, the test specimens were immersed in water. Dead weights were used to keep them completely submerged. After 72 h, the test specimens were removed from the water one by one and immediately sealed. Their free water saturation mass, m_{sat} [kg] was recorded. The plastic seal was removed and the test specimens were dried at (70±2) °C in a ventilated oven with air taken outside ($T=(23\pm2)^\circ\text{C}$ and $\varphi=0.5\pm0.05$), until constant mass was achieved. They were cooled in a desiccator with silica gel until the temperature bellows 40 °C, and then weighed [14]. The dry mass, m_0 [kg], and dimensions were recorded. To obtain the apparent density at reference conditions the same 15 test specimens were placed in a climatic chamber at $T=(23\pm2)^\circ\text{C}$ and $\varphi=0.5\pm0.05$, for 6 weeks, until constant mass was achieved. Each board was weighed and its mass, m_{RC} [kg], recorded.

The mean values obtained for the dry density, ρ_0 [kg/m³], given by the relation $\rho_0 = m_0/V$, where V [m³] is the volume of the test specimens, the apparent density [kg/m³] given by the relation $\rho_a = m_{RC}/V$, the saturation moisture content mass per mass ($u_{sat} = (m_{sat} - m_0)/m_0$ [kg/kg]), and the saturation moisture content mass per volume ($W_{sat} = u_{sat} \rho_0$ [kg/m³]), are presented in Table 3-12.

Table 3-12: Dry density, apparent density and saturation moisture content, content (mass per mass and mass per volume) of MD ICB.

Density	ρ_0 [kg/m ³]	ρ_a [kg/m ³]	u_{sat} [kg/kg]	W_{sat} [kg/m ³]
Medium	156 (8.0)	158 (7.8)	0.518 (0.025)	80.64 (1.762)

As expected, although the air was forced out of the material in the immersion procedure, the saturation water content is lower than the maximum water content obtained before (section 3.3.2.1).

3.3.2.3 Variation of the thermal conductivity with moisture

The thermal conductivity variation as a function of the board's moisture content was measured. The sample consisted of 6 test specimens with nominal dimensions of (300×300×70) mm³. The specimens were first totally immersed in water at $T = (23 \pm 2)$ °C for 72 h. After this time, they were removed from the water one by one and immediately placed inside a thin vapour proof bag, which was then sealed. The thermal conductivity of each test specimen was measured using the heat flow meter method, as before. After this first measurement, the vapour proof material was removed and the test specimens were left to dry at laboratory temperature, $T = (23 \pm 5)$ °C. During the drying period the specimens were sealed at different times and the thermal conductivity determined again. Before each measurement the specimens were weighed and the moisture content calculated. The test specimens were then dried in a ventilated oven until constant mass was achieved, and the thermal conductivity in the dry state, λ_{dry} [W/(m K)], measured. A total of twelve measurements were taken for each specimen during the course of the drying process.

Figure 3-6 presents the global set of the measured thermal conductivity of medium density expanded cork as a function of its moisture content u [kg/kg], in the capillary range ($\lambda_{meas}(u)$).

Thus, this figure includes the dry and saturated state results. These results allow to conclude that the measured thermal conductivity increases by about 52.5% from dry to saturation state.

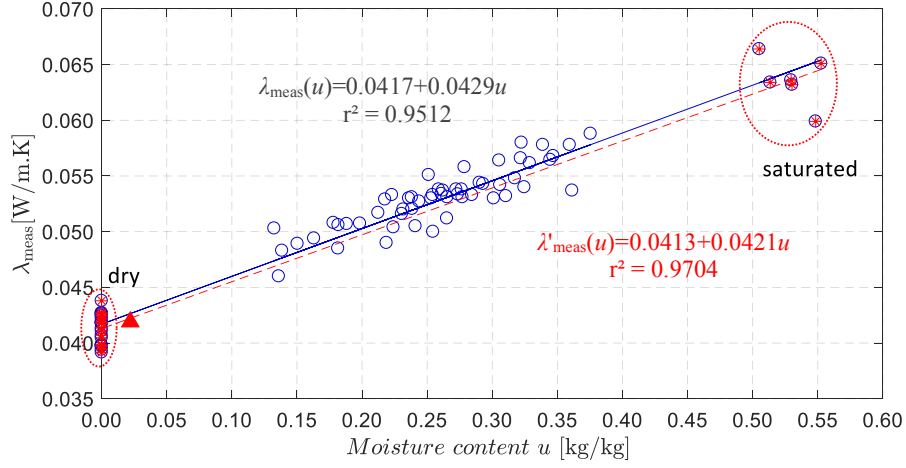


Figure 3-6: Measured thermal conductivity of medium density expanded cork as a function of moisture content u [kg/kg] (the triangle represents the mean value of λ_{meas} at reference conditions obtained experimentally for a mean moisture content of 0.022 kg/kg (section 3.3.1.3)).

According to ISO 10051:2008 [69], when the variation of λ_{meas} as a function of moisture content can be expressed as a linear relationship of the type $\lambda_{\text{meas}}(u) = \lambda_{\text{dry}} + a.u$, the movement of liquid is negligible. Based on the full set of measured results, the effective thermal conductivity can be given by:

$$\lambda(u) = 0.0417 + 0.0429.u \quad (3-1)$$

where 0.0429 corresponds to the moisture correction factor, a . Considering only the results of the thermal conductivity for the dry and saturated state, in which there is no movement of liquid, a second linear equation $\lambda'(u)$ was computed (dashed line in Figure 3-6).

$$\lambda'(u) = 0.0413 + 0.0421.u \quad (3-2)$$

The maximum difference between $\lambda'(u)$ and $\lambda(u)$ is 1.3 % at $u = 0.55$ kg/kg. This difference allows us to conclude that the movement of liquid and the phase changes have no significant influence on the measurements of the thermal conductivity.

Figure 3-6 also plots the thermal conductivity average when the material has been previously conditioned in the reference conditions ($T = 23$ °C, $\phi = 0.5$) after one wetting/drying cycle. The obtained value of $\lambda_{(23/0.5)} = 0.0419$ W/(m K) with $u_{(23/0.5)} = 0.022$ kg/kg is represented by the

triangular mark (see section 3.3.1.3). Applying equation (3-1) to $u_{(23/0.5)}$ the calculated $\lambda_{(23/0.5)}$ is equal to 0.0426 W/(m K), proving that eqn. (3-1) is also valid in the hygroscopic range.

3.3.2.4 Hygroscopic sorption properties

The hygroscopic sorption properties of the material were evaluated in accordance with the procedures indicated in ISO 12571:2013 [22], using the climatic chamber method. The climatic chamber was set at $(23 \pm 0.5)^\circ\text{C}$ and five relative humidity values (φ) were considered: 0.3, 0.5, 0.8, 0.9, and 0.95. The sample consisted of 6 test specimens with nominal dimensions of $(300 \times 300 \times 70) \text{ mm}^3$.

First the test specimens were dried in a ventilated oven at $T = (70 \pm 2)^\circ\text{C}$ until constant mass was achieved. They were cooled in a desiccator with silica gel until the temperature dropped below 40°C , and then weighed. Their dry mass, m_0 was recorded and the 6 test specimens were then placed in the climatic chamber, at the lowest relative humidity of $\varphi = 0.3$ until constant mass was achieved. Their water content, mass per mass, u [kg/kg], was calculated using the relation $u = (m - m_0)/m_0$ [kg/kg], in which m is the mass of the test specimen and m_0 is its dry mass. The procedure was repeated for the other relative humidity values.

The starting point of the desorption curve was the last point obtained on the sorption curve, $\varphi = 0.95$. The procedure was repeated for decreasing relative humidity values.

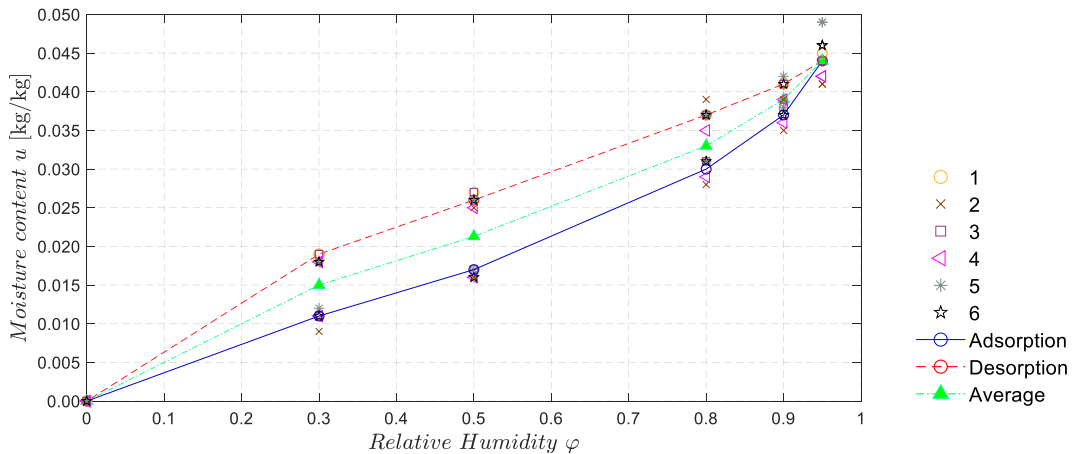


Figure 3-7: Adsorption (continuous blue line) and desorption curves (red dashed line) of medium density expanded cork at $(23 \pm 0.5)^\circ\text{C}$ and their average (green triangles).

Figure 3-7 presents the adsorption and desorption curves of medium density expanded cork at $T = (23 \pm 0.5)^\circ\text{C}$, which, for each relative humidity, are based on the mean of the obtained values of the six test specimens and so exhibit the typical behaviour of macro-porous materials

[32]. According to the IUPAC [70] classification, the obtained curves are Type II (S-shaped). Three different levels of water retention are clear in the adsorption curve. Up to $\varphi = 0.5$, the slope of the curve is less pronounced, indicating mono-molecular water absorption. As the relative humidity increases, the slope of the curve increases. First the water is absorbed by multi-molecular adsorption ($0.5 \leq \varphi \leq 0.9$), followed by capillary condensation, which is reflected in the increased slope of the curve ($\varphi > 0.9$). The results show that hysteresis is significant: during the adsorption at $\varphi = 0.5$, the mean moisture content is 0.017 kg/kg, while during desorption it is 0.026 kg/kg.

The mean values between the adsorption and the desorption curves are represented by the green triangles in Figure 3-7. It should be noted that the mean moisture content of the expanded cork boards in the reference state after being subjected to a wetting/drying process, $u_{RC} = 0.022$, is considerably higher than the mean value obtained in the adsorption process, in which $u_{(23/0.5)} = 0.017$ kg/kg. The average value of $u_{(23/0.5)}$ in the adsorption/desorption process is 0.021 kg/kg, which is in close agreement with the obtained mean value after a wetting/drying process. So, since the material moisture content depends on its wetting history, the average of the sorption and desorption curves is a more reliable representation of the real behaviour of medium density boards, as stated by Künzel [71].

3.3.2.5 Water absorption coefficient by partial immersion

As a complement to Section 3.3.1.2, the water absorption coefficient by partial immersion (A_w [kg/(m²·s^{0.5})]) is now presented, following the procedure described in ISO 15148:2002 [29]. A_w was determined by measuring the change in mass of the test specimen that has its bottom face in contact with water, over a period of 24 h. The side faces of each test specimen were wrapped with fine gauze and covered with paraffin wax to ensure complete sealing. The test specimens were placed in the water tank. The water level was kept constant at (5±2) mm above the base. After 5 minutes each test specimen was removed from the water, its surfaces blotted with a damp sponge and then weighed. This procedure was repeated at 20 min, 1 h, 2 h, 4 h, 8 h, 12 h and 24 h. The sample consists of 3 test specimens with nominal dimensions of (300×300×70) mm³.

The Δm_t values, taken as the difference between the mass at each weighing (m_t) and the initial mass (m_i) per area, were plotted against the square root of the weighing times. The resulting graph is type A (Figure 3-8), i.e., after an initial period of stabilization, a straight line can be drawn through the values of Δm_t plotted against \sqrt{t} . The water absorption

coefficient is $A_w = (\Delta m'_{t_f} - \Delta m'_0)/\sqrt{t_f}$ (where $\Delta m'_{t_f}$ and $\Delta m'_0$ are the values of Δm on the defined straight line at t_f and $t = 0$ s, respectively).

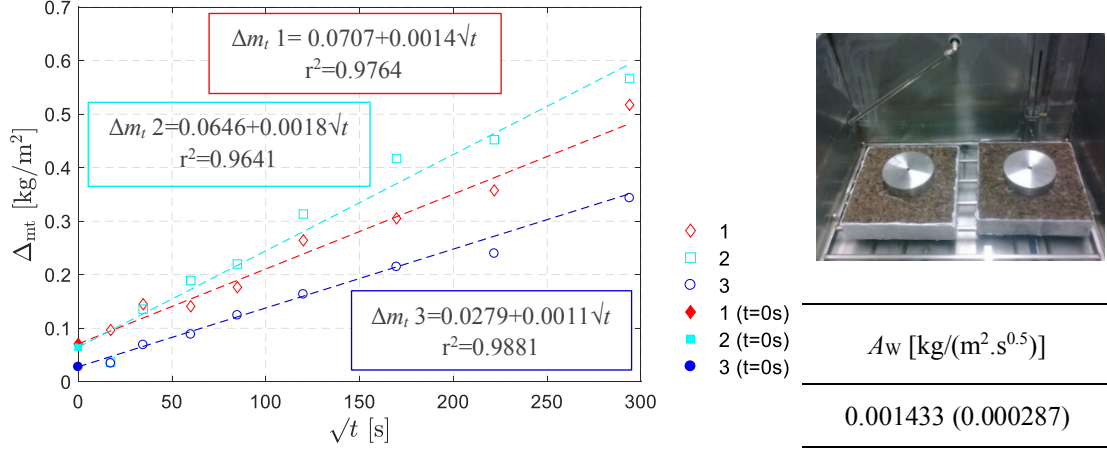


Figure 3-8: Test apparatus for water absorption evaluation and test results.

3.3.2.6 Liquid water conductivity/diffusivity

The liquid water conductivity/diffusivity $D_l(\varphi)$ [s] was obtained as indicated in EN 15026:2007 [72]:

$$D_l(\varphi) = -D_w(W) \frac{\partial W(\varphi)}{\partial p_{\text{suc}}} \quad (3-3)$$

In which p_{suc} [Pa] is the suction pressure, φ is the relative humidity, $D_w(W)$ [m²/s] is the liquid transport coefficient and $W(\varphi)$ [kg/m³] is the sorption isotherm that is given by:

$$W(\varphi) = \frac{k_1}{[1 + (a_1 h)^{n_1}]^{m_1}} W_{\text{sat}}, \quad h = \frac{p_{\text{suc}}}{\rho_l g} = -\frac{R_w T \ln(\varphi)}{g} \quad (3-4)$$

in which $m_1 = 1 - 1/n_1$, T [K] is the temperature, ρ_l [kg/m³] is the liquid water density, g [m/s²] is the acceleration of the gravity, $R_w = 461.4$ [J/(kg K)] is the water vapour gas constant, and W_{sat} [kg/m³] is the saturation moisture content.

To obtain $W(\varphi)$, eqn. (3-4) can be rewritten:

$$\frac{W(\varphi)}{W_{\text{sat}}} = \frac{k_1}{\left[1 + \left(a_1 - \frac{R_w T \ln(\varphi)}{g}\right)^{n_1}\right]^{m_1}} \quad (3-5)$$

Manipulating eqn. (3-5) the following derivative can be obtained:

$$\frac{\partial W(\varphi)}{\partial p_{\text{suc}}} = \frac{-K_1 \left(a_1 \frac{p_{\text{suc}}}{\rho_l g}\right)^{n_1} \left[1 + \left(a_1 \frac{p_{\text{suc}}}{\rho_l g}\right)^{n_1}\right]^{-m_1-1}}{p_{\text{suc}}} \quad (3-6)$$

$D_w(W)$ [m^2/s] (eqn. (3-3)) can be computed as proposed by Künzel [71].

The predominant moisture transport mechanism in capillary porous materials is capillary liquid transport. Although it is basically a convective phenomenon, in the context of building physics it is sufficiently accurate that the liquid transport in the pore spaces can be regarded as a diffusion phenomenon [68]:

$$j_l = -D_w(W) \cdot \text{grad } W \quad (3-7)$$

in which j_l [$\text{kg}/(\text{m}^2 \text{ s})$] is the liquid transport flux density.

D_w is generally strongly dependent on the material's moisture content. If a material water content has a linear increase over the square root of time the liquid transport can be described by the diffusion formula.

There are two liquid transport coefficients: D_{ws} is the liquid transport coefficient for suction and D_{ww} the liquid transport for redistribution.

The water absorption coefficient, A_w [$\text{kg}/(\text{m}^2 \text{ s}^{0.5})$], is the standard parameter used to describe the capillary suction of a material. The increase of D_{ws} with moisture content can be estimated using eqn. (3-8) [35,71].

$$D_{ws}(\varphi) = 3.8 \left(\frac{A_w}{W_{\text{sat}}}\right)^2 1000^{W/W_{\text{sat}} - 1} \quad (3-8)$$

D_{ww} is neglected in the present work given its small contribution.

From eqn. (3-6) and eqn. (3-8), eqn. (3-3) takes the form:

$$D_l(\varphi) = -3.8 \cdot \left(\frac{A_w}{W_{sat}} \right)^2 1000^{W/W_{sat}-1} \frac{-K_1 \left(\frac{a_1 p_{suc}}{\rho_l g} \right)^{n_1} \left[1 + \left(\frac{a_1 p_{suc}}{\rho_l g} \right)^{n_1} \right]^{-m_1-1}}{p_{suc}} \quad (3-9)$$

$p_{suc}(\varphi)$ is given by:

$$p_{suc}(\varphi) = -\rho_l R_w T \ln(\varphi) \quad (3-10)$$

with $\rho_l = 1000 \text{ kg/m}^3$.

The coefficients K_1 , a_1 and n_1 in equation (3-5) were defined numerically using the sorption isotherm and the free saturation water content. The resulting W/W_{sat} is plotted in Figure 3-9. The liquid water conductivity/diffusivity given by eqn. (3-9), is then evaluated and plotted in Figure 3-10.

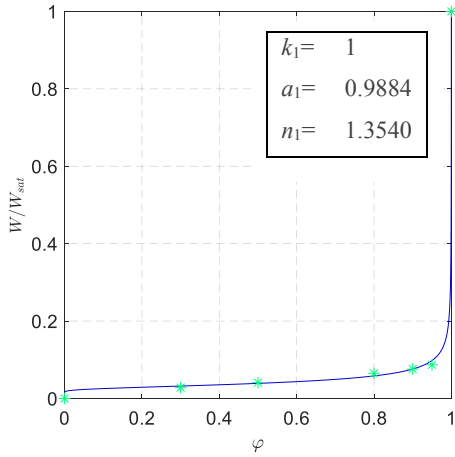


Figure 3-9: W/W_{sat} curve and the experimental data represented by green dots.

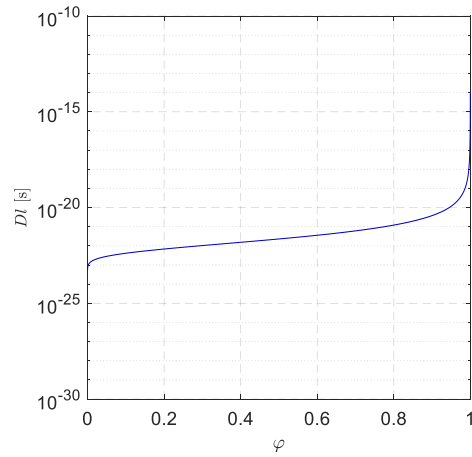


Figure 3-10: Liquid water conductivity/diffusivity function of φ for MD ICB.

3.3.3 Drying

The drying behaviour of the medium density expanded cork after being saturated was then evaluated. Three different drying scenarios were selected:

- Set 1 - five faces of the board are sealed (the front face is free);

- Set 2 - four faces of the board are sealed (the front and the bottom faces are free);
- Set 3 - all the 6 faces are free and not sealed.

Each set comprised 4 test specimens with nominal dimensions of $(300 \times 300 \times 70) \text{ mm}^3$.

The test started by drying all test specimens in a ventilated oven at $T = (70 \pm 5) ^\circ\text{C}$ for 72 hours. Then they were measured and their dry mass recorded. The desired faces for each condition were sealed with fine gauze and paraffin wax. After sealing they were placed in the climatic chamber at reference conditions until constant mass was achieved and then weighed. Then the test specimens were placed in a tank with 140 mm of water above the upper surface (see Figure 3-11a).



Figure 3-11: Test specimens: a) During immersion; b) Draining stage.

After 72 hours, they were removed from and placed on a drainer, 45° slope. They were left to drain for 5 minutes (Figure 3-11b), after which the excess surface water was removed from each board with absorbent paper. The boards were then weighed. The mass, m_{72} was recorded. They were placed in the climatic chamber to dry, at reference conditions. Each board was weighed at intervals of 30 minutes for the first six hours, at hourly intervals for the next 3 hours and afterwards at 24 h, 27 h, 30 h, 33 h, 48 h, 72 h, 96 h, 120 h, 168 h, 288 h, 360 h, 456 h, 696 h, 768 h, 1032 h and 1200 h.

The water content of each board, mass per mass, was calculated in relation to the weight of the boards after being sealed and conditioned under reference conditions.

The mean water content, expressed mass per mass, as a function of the square root of time for each set and for the first nine hours of drying is presented in Figure 3-12. The trend line (polynomial) and the correlation factor for the mean values are also presented. From this

figure it can be seen that a higher initial water content corresponds to a higher exposed area. Expanded cork is an agglomerated material and has channels that enable the water to enter by percolation. Thus, the larger the exposed area the more water percolates throughout the material. However, the water retained therein tends to drain rapidly, in liquid state, mainly due to the action of gravity. In all cases, more than a half of the initial water content was lost in the first nine hours of drying.

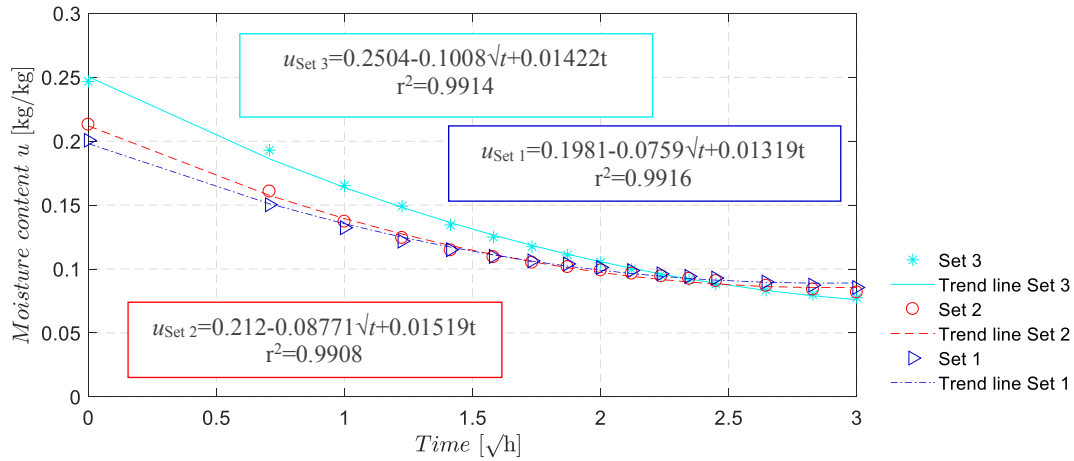


Figure 3-12: Mean moisture content u [kg/kg] for each Set for the first nine drying hours and the respective trend lines.

Section 3.3.2.2 described the saturation water content of the medium density expanded cork boards and gave a value of $u_{sat} = 0.5180$ kg/kg. In this section, for the same immersion time, a value of $u_{72} = 0.2468$ (0.0303) kg/kg was obtained for Set 3, with 6 faces free, which is 47.6% of the achieved u_{sat} . In the first case, the boards were immersed by pushing them to the bottom of the water tank such that most of the air that was entrapped in the pores could escape. In the second case the boards were placed at the bottom of the tank and then water was added. Therefore, it was more difficult for the air entrapped in the pores to escape, which reduced the percolation of water.

To better illustrate the drying process, Figure 3-13 shows the mean water mass loss per hour, W [g/h], for each condition and the resulting trend lines.

In the first 30 minutes all sets lose water rapidly. W for all sets decreases exponentially over time, but tends to converge to the same values as time passes.

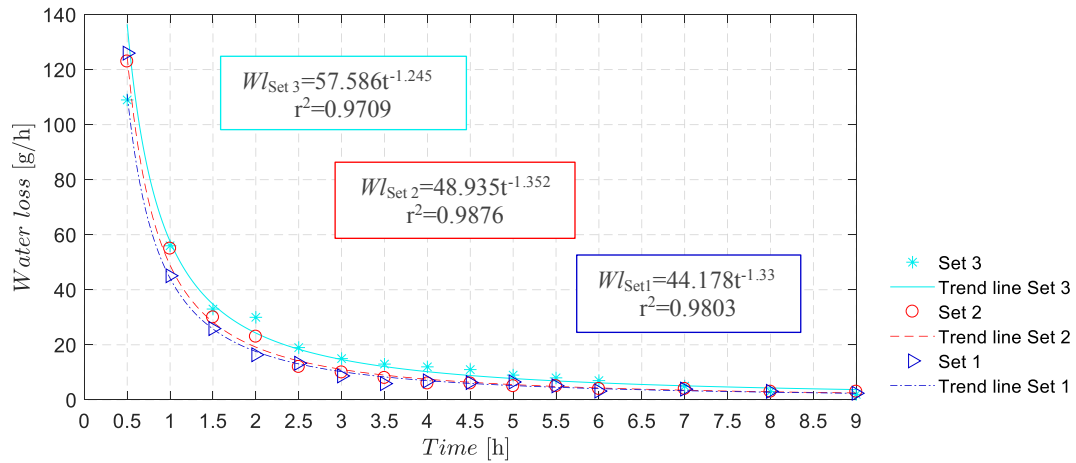


Figure 3-13: Mean water loss [g/h] in the first 9 drying hours for each Set.

To illustrate this behaviour visually Figure 3-14a shows the medium density boards drying in the climatic chamber at $t = 3$ h (from left to right, the board with six faces free, two faces free and one face free). At this time, the water accumulation on the bottom of the boards due to gravity action can be clearly seen. At $t = 9$ h (Figure 3-14b) the water on the bottom has almost disappeared in all cases.

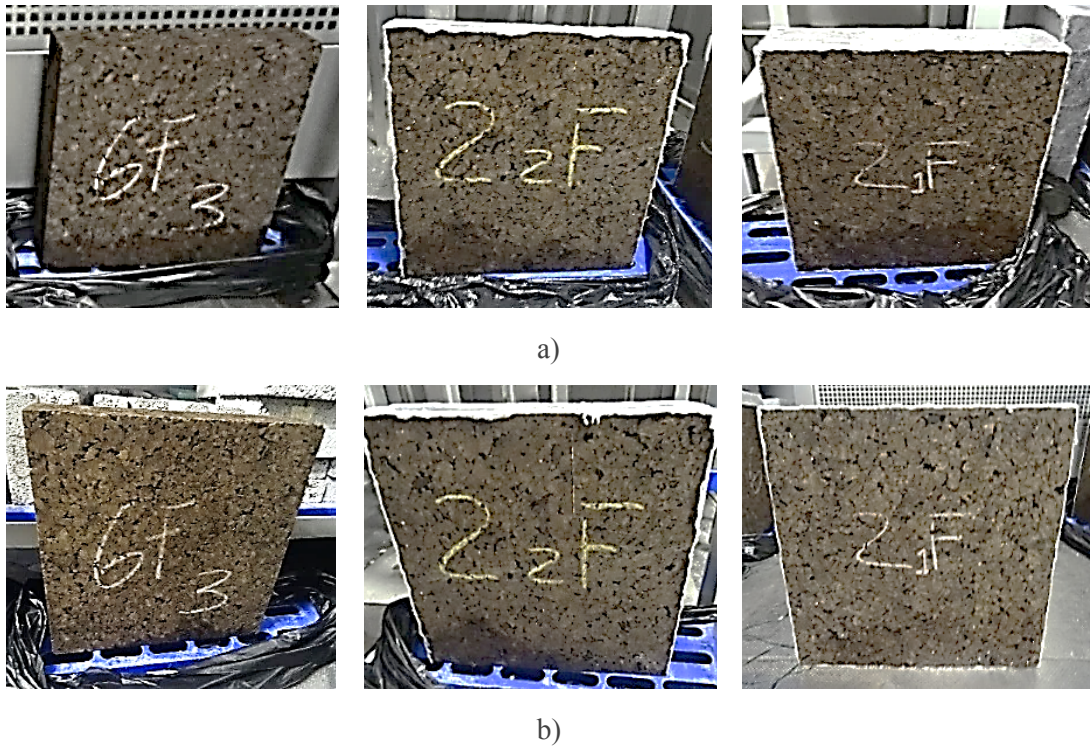


Figure 3-14: Expanded cork boards drying in climatic chamber (from left to right: Set 3, Set 2 and Set 1: a) $t = 3$ h; b) $t = 9$ h.

The drying curves after the first nine hours as a function of the square root of time, for the 3 Sets, are presented in Figure 3-15. It can be clearly seen that for the 3 Sets the drying process after the first nine hours is considerably slower than it was at the beginning. The movement of the liquid water is no longer dominated by the gravity effect but by capillary conduction and vapour and surface diffusion. As expected, the drying process of Set 6 is considerably faster than in the other two cases because of the greater exposed area. A linear trend line in a \sqrt{t} domain approaches the drying behaviour of Set 2 and Set 3. Likewise, Set 2, with two faces free, dries at a slightly higher rate than Set 1 (one face free).

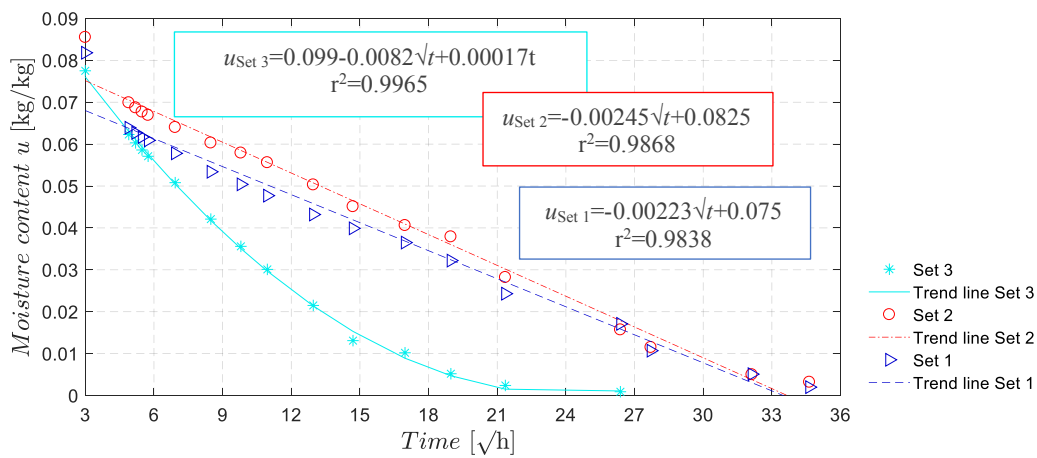


Figure 3-15: Mean moisture content u [kg/kg] change after the first nine drying hours.

3.4 Durability

Expanded cork board is a completely natural material and therefore its behaviour is expected to change over time and with its continuous exposure to the sun, temperature gradients and rain. This section describes the freeze-thaw cycles that were performed to evaluate the evolution of the compressive strength behaviour in dry and wet conditions. The long-term creep was then evaluated and the effects of temperature and humidity when the material is exposed to daylight were analysed. The results are presented in the following sections. As before, the equipment used to perform each test is described in Annex 1, Table A3.

3.4.1 Freeze-thaw cycles

The volume of water is known to expand by 9% when it changes from the liquid to the solid state. This expansion may cause alteration of the void structure in cellular materials and repeated of freeze-thaw cycles may result in internal cracking and degradation of the material [47]. The freeze-thaw test is characterized by the ability of a material to withstand repeated

moistening periods followed by freezing conditions (300 cycles over 45 days), quantified by the material water absorption and variation in behaviour under compression. To measure the variation of the compressive strength behaviour, initial tests of compressive behaviour were performed, according to EN 826:2013 [59]. Two additional tests, following the same standard, were performed in wet and dry conditions after the end of the freeze-thaw cycles.

The sample consists of 6 test specimens that were split into two groups of 3 test specimens each, Set B₁ and Set B₂, with nominal dimensions of (200×200×70) mm³. Three more test specimens with the same nominal dimensions were used to perform the initial compression test up to 10% of deformation to evaluate σ_{10} .

The six test specimens (Set B₁ plus Set B₂) were subjected to long term water absorption by immersion test (EN 12087:2013 [65]). W_{LT} [%] was calculated after the immersion time by measuring the test specimen's weight change. Then, the same test specimens were subjected to 300 freeze-thaw cycles [1 h at (-20±2) °C and then immersed in water at $T = (20 \pm 2)$ °C for 1 h]. At the end of the freeze-thaw cycles, the water absorption, W_m [%], that is equal to $((m_{1f} - m_{LT})/m_{LT}) \times 100$ in which m_{1f} [g] is the mass of the test specimen after the 300 freeze-thaw cycles, and m_{LT} [g] is the mass of the test specimen after the long-term water absorption test. Then Set B₁ was tested for compression in wet condition and Set B₂ was dried at $T = 70$ °C in a ventilated oven and tested in dry condition. The changes in the compressive behaviour obtained in wet and dry conditions are given by $\Delta\sigma_{10,wet} = (\sigma_{10,wet}/\sigma_{10}) \times 100$ and $\Delta\sigma_{10,dry} = (\sigma_{10,dry}/\sigma_{10}) \times 100$, respectively.

After testing, the test specimens were visually inspected and no signs of cracking or material desegregation were found.

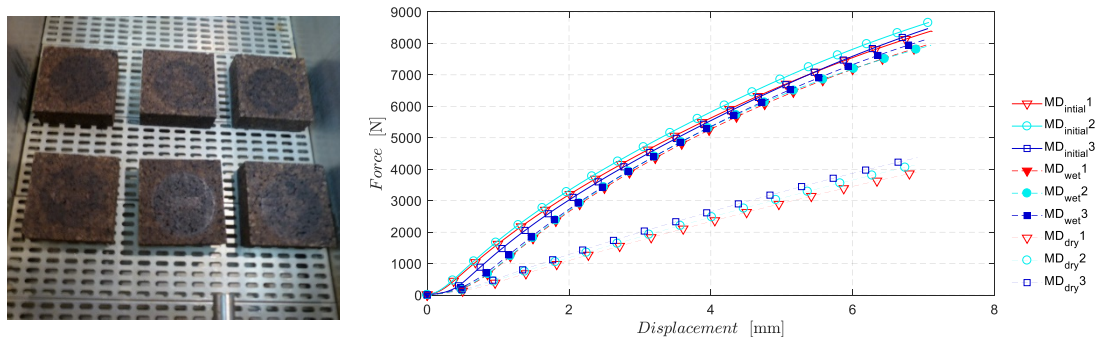


Figure 3-16: Test specimens during freezing conditioning (picture) and force-displacement curves of the compressive test.

Figure 3-16 shows the test specimens during freezing and the force-displacement curves for the test specimens in initial conditions and after the freeze-thaw cycles, in wet and dry conditions. Table 3-13 presents test results.

Table 3-13: Compressive results after freeze-thaw test.

$\sigma_{10,initial}=210.6$ (3.25) kPa	$\sigma_{10,wet}=199.0$ (165) kPa	$\sigma_{10,dry}=106.7$ (4.58) kPa
$\Delta\sigma_{10,wet}=94\%$	$\Delta\sigma_{10,dry}=51\%$	
$W_{LT}=13.0$ (0.43)%	$W_m=36.4$ (0.68)%	

In the force displacement curves (Figure 3-16) the similar behaviour of the material under compression before and after the freeze-thaw cycles for the wet condition should be noted. However, after the test specimens have been dried the force required to produce the same deformation drops considerably, which is reflected in the results presented in Table 3-13.

Even though the compressive stresses at 10% deformation in dry conditions (the most unfavourable), after the defrost cycles, have changed 51%, they are still within the values established in the EN 13170:2012+A1:2015 [14], with a level of CS(10)100 ($\sigma_{10} \geq 100$ kPa).

3.4.2 Compressive creep

The compression creep, X_{ct} was calculated by measuring the increase in deformation of the test specimen when subjected to a constant compressive stress with time, under specified conditions of temperature and humidity. The assumptions presented in EN 1606:2013 [73] to extrapolate the compressive creep up to 30 times the actual test time were followed. In this work the compressive creep was evaluated for 10 years, which corresponds to a measurement time of 122 days.

Nine square test specimens were cut with nominal dimensions of $(100 \times 100 \times 50)$ mm³, 3 for each of the compressive loads used to generate 15, 20 and 25% of the compressive stress $\sigma_{10}=205$ kPa (defined in section 3.2.4).

The relative deformation ε_t for a 10-year extrapolation for each load is presented in Figure 3-17 together with the evolution of the deformation, extrapolated until $t=88560$ h (blue line), for compressive loads of 30, 40 and 50 kPa. The red dots represent the measured values.

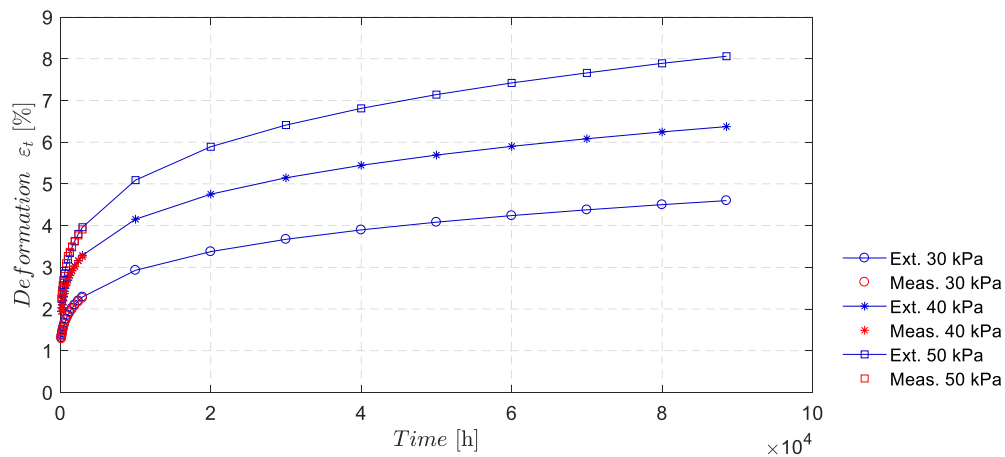


Figure 3-17: Medium measured values (Meas.) and evolution of the deformation for the compressive loads of 30, 40 and 50 kPa extrapolated until $t = 87600$ h (Ext.).

Table 3-14 presents the extrapolated values of deformation for 10 years. As expected, higher compressive loads correspond to larger long-term deformation. The highest extrapolated deformation was around 8%. It is important to note that if the material is used in roofs, knowledge of the compressive creep deformation can be important if heavy and sensitive equipment is likely to be installed.

Table 3-14: Expected relative deformation at the end of 10 years for compressive loads of 30, 40 and 50 kPa.

Density	Compressive stress [kPa]	ϵ_t [%]
Medium ICB	30	4.6
	40	6.4
	50	8.1

3.4.3 Ageing test by exposure to xenon-arc light

This test was used to evaluate the change in the colour of the test specimen under xenon arc light in the presence of moisture to reproduce the weathering effects (temperature, humidity) that occur when materials are exposed to daylight. The test was performed following method A in ISO 4892-2:2013 [74]. The test consists of performing cycles of 120 minutes each under xenon radiation for 102 minutes with the chamber in dry state and 18 minutes under xenon radiation and the chamber in wet state, i.e., radiation with the test specimens

submerged in water. A total of 120 cycles were performed, corresponding to 10 days of cycles. The sample consisted of 4 test specimens with nominal dimensions of $(300 \times 300 \times 70)$ mm³.

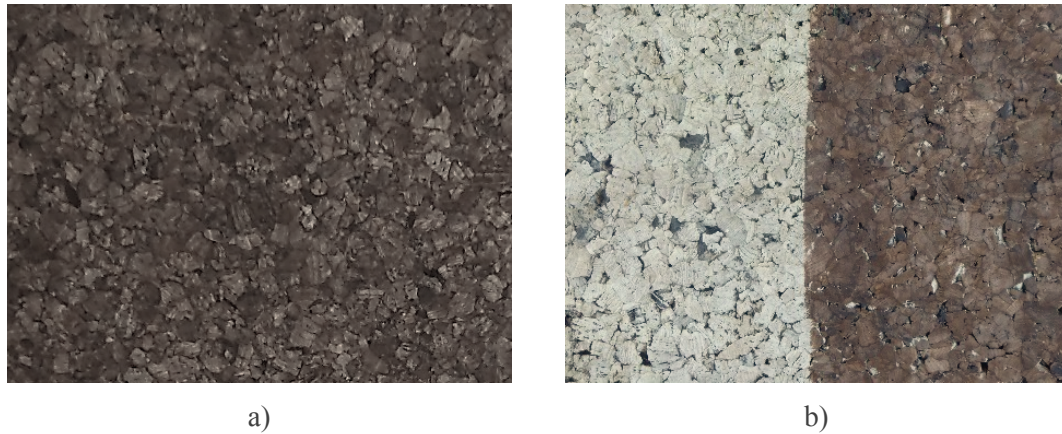


Figure 3-18: Test specimen subjected to ageing: a) Test specimen before test; b) Test specimen after the test with the right side slightly polished.

Figure 3-18 gives the initial (a) and the final (b) aspect of one of the test specimens subjected to the test. The right side of this board was slightly polished. As can be seen in Figure 3-18b, the final colour is noticeably lighter than the initial one. Although, as shown by the right side of the board, after a slight polishing the board recovers the original colour.

3.5 Final Remarks

Mechanical and hygrothermal tests were performed on MD ICB and ST ICB. The mechanical properties of the MD ICB far exceed the values obtained for the standard material, without substantial loss of the hygrothermal properties, thus confirming that MD ICB is more suitable for use as external insulation than ST ICB.

A comprehensive study of the MD ICB hygrothermal properties was carried out. The free saturation water content of 0.518 kg/kg was achieved. However, it was observed that for the same immersion time, if the air entrapped within the pores of the material is not forced out, the achieved water content is equal to 0.2468 kg/kg.

The measured thermal conductivity of the moist MD ICB shows a linear increase as a function of moisture content. A moisture correction factor of 0.0429 was calculated experimentally for the capillary range and also found to be valid for the hygroscopic range. It was found that the average material moisture content between the absorption and desorption process gives a more realistic representation of the material hygroscopic behaviour, because when used as an

external coating the board will be subjected to wetting /drying cycles. An increase of about 52.5% was recorded when the MD ICB state changes from dry to saturation. Meanwhile a relatively small increment of about 1.5% was noted when the MD ICB changes from dry to the so-called reference state ($\varphi=0.5$ and $T=23\text{ }^{\circ}\text{C}$).

Regarding the drying behaviour of MD ICB, it was observed that more than a half of the initial water content is lost in the first nine hours of drying, when the movement of the liquid is mainly due to gravity. The drying process becomes considerably slower after the initial period as the moisture movement is no longer due to the gravity effect but mainly due to capillary conduction and vapour and surface diffusion.

To evaluate the long-term behaviour, the MD ICB boards were exposed to freeze-thaw cycles, compressive creep test and ageing by exposure to xenon arc light. This process made it possible to conclude that the material is resistant even to a long-term exposure to external conditions. It is concluded that MD ICB is suitable for use as uncoated external insulation on building envelopes.

3.6 References

- [1] B. Soares, L. Reis, L. Sousa, Cork composites and their role in sustainable development, Eng. Procedia. 10 (2011) 3214–3219. doi:10.1016/j.proeng.2011.04.531.
- [2] J. Sierra-Pérez, I. López-Forniés, J. Boschmonart-Rives, X. Gabarrell, Introducing eco-ideation and creativity techniques to increase and diversify the applications of eco-materials: The case of cork in the building sector, J. Clean. Prod. 137 (2016) 606–616. doi:10.1016/j.jclepro.2016.07.121.
- [3] S.P. Silva, M.A. Sabino, E.M. Fernandes, V.M. Correlo, L.F. Boesel, R.L. Reis, Cork : properties , capabilities and applications, Int. Mater. Rev. 50 (2005) 345–365. doi:10.1179/174328005X41168.
- [4] A. Soares, M. Júlio, I. Flores-Colen, L. Ilharco, J. de Brito, J. Gaspar Martinho, Water-Resistance of Mortars with Lightweight Aggregates, Key Eng. Mater. 634 (2014) 46–53. doi:10.4028/www.scientific.net/KEM.634.46.
- [5] L. Gil, Effect of hot pressing densification on the cellular structure of black agglomerated cork board, Eur. J. Wood Wood Prod. 52 (1994).

- doi:10.1007/BF02615479.
- [6] S. Knapic, C.P. dos Santos, H. Pereira, J.S. Machado, Performance of expanded high-density cork agglomerates, *J. Mater. Civ. Eng.* 29 (2017) 1–6. doi:10.1061/(asce)mt.1943-5533.0001718.
 - [7] A.S. Tártaro, T.M. Mata, A.A. Martins, J.C.G. Esteves da Silva, Carbon footprint of the insulation cork board, *J. Clean. Prod.* 143 (2017) 925–932. doi:10.1016/j.jclepro.2016.12.028.
 - [8] M. Demertzi, J. Sierra-Pérez, J.A. Paulo, L. Arroja, A.C. Dias, Environmental performance of expanded cork slab and granules through life cycle assessment, *J. Clean. Prod.* 145 (2017) 294–302. doi:10.1016/j.jclepro.2017.01.071.
 - [9] R.T. Jardim, F.A.O. Fernandes, A.B. Pereira, R.J.A. de Sousa, Static and dynamic mechanical response of different cork agglomerates, *Mater. Des.* 68 (2015) 121–126. doi:10.1016/j.matdes.2014.12.016.
 - [10] A. Díaz-Parralejo, M.A. Díaz-Díez, A. Macías-García, P. de la Rosa Blanco, V.G. Serrano, Study of black and composite agglomerates of cork as thermal insulating materials, *Mater. Lett.* 57 (2003) 4004–4008. doi:10.1016/S0167-577x(03)00255-6.
 - [11] N. Lakreb, B. Bezzazi, H. Pereira, Mechanical strength properties of innovative sandwich panels with expanded cork agglomerates, *Eur. J. Wood Wood Prod.* 73 (2015) 465–473. doi:10.1007/s00107-015-0908-y.
 - [12] R. Ferreira, D. Pereira, A. Gago, J. Proença, Experimental characterisation of cork agglomerate core sandwich panels for wall assemblies in buildings, *J. Build. Eng.* 5 (2016) 194–210. doi:10.1016/j.job.2016.01.003.
 - [13] O. Castro, J.M. Silva, T. Devezas, A. Silva, L. Gil, Cork agglomerates as an ideal core material in lightweight structures, *Mater. Des.* 31 (2010) 425–432. doi:10.1016/j.matdes.2009.05.039.
 - [14] EN 13170:2012+A1:2015 - Thermal insulation products for buildings- Factory made products of expanded cork (ICB) – Specification, European Committee for Standardisation, (2012).
 - [15] K.B. Najim, External load-bearing walls configuration of residential buildings in Iraq and their thermal performance and dynamic thermal behaviour, *Energy Build.* 84 (2014) 169–181. doi:10.1016/j.enbuild.2014.07.064.

- [16] L. Škerget, A. Tadeu, BEM numerical simulation of coupled heat and moisture flow through a porous solid, *Eng. Anal. Bound. Elem.* 40 (2013) 154–161. doi:10.1016/j.enganabound.2013.12.006.
- [17] A. Korjenic, V. Petránek, J. Zach, J. Hroudová, Development and performance evaluation of natural thermal-insulation materials composed of renewable resources, *Energy Build.* 43 (2011) 2518–2523. doi:10.1016/j.enbuild.2011.06.012.
- [18] E. Latif, S. Tucker, M.A. Ciupala, D.C. Wijeyesekera, D. Newport, Hygric properties of hemp bio-insulations with differing compositions, *Constr. Build. Mater.* 66 (2014) 702–711. doi:10.1016/j.conbuildmat.2014.06.021.
- [19] M. Jerman, R. Černý, Effect of moisture content on heat and moisture transport and storage properties of thermal insulation materials, *Energy Build.* 53 (2012) 39–46. doi:10.1016/j.enbuild.2012.07.002.
- [20] T. Vrána, F. Björk, A laboratory equipment for the study of moisture processes in thermal insulation materials when placed in a temperature field, *Constr. Build. Mater.* 22 (2008) 2335–2344. doi:10.1016/j.conbuildmat.2007.10.007.
- [21] M. Reif, J. Zach, J. Hroudová, Studying the Properties of Particulate Insulating Materials on Natural Basis, *Procedia Eng.* 151 (2016) 368–374. doi:10.1016/j.proeng.2016.07.390.
- [22] ISO 12571:2013- Hygrothermal performance of building materials and products - Determination of hygroscopic sorption properties, International Organization for Standardisation, (2013).
- [23] M. Ibrahim, E. Wurtz, P.H. Biwolé, P. Achard, H. Sallee, Hygrothermal performance of exterior walls covered with aerogel-based insulating rendering, *Energy Build.* 84 (2014) 241–251. doi:10.1016/j.enbuild.2014.07.039.
- [24] A. Korjenic, J. Zach, J. Hroudová, The use of insulating materials based on natural fibers in combination with plant facades in building constructions, *Energy Build.* 116 (2016) 45–58. doi:10.1016/j.enbuild.2015.12.037.
- [25] H.M. Künzeli, A.H. Holm, M. Krus, Hygrothermal Properties and Behaviour of Concrete, *WTA-Almanach.* (2008) 161–181.
- [26] A. Lagorce-Tachon, T. Karbowiak, D. Champion, R.D. Gougeon, J. Bellat, Mechanical properties of cork : Effect of hydration, *Mater. Des.* 82 (2015) 148–154.

- doi:10.1016/j.matdes.2015.05.034.
- [27] C. Feng, H. Janssen, C. Wu, Y. Feng, Q. Meng, Validating various measures to accelerate the static gravimetric sorption isotherm determination, *Build. Environ.* 69 (2013) 64–71. doi:10.1016/j.buildenv.2013.08.005.
- [28] A. Ronzino, V. Corrado, Measuring the Hygroscopic Properties of Porous Media in Transient Regime. From the Material Level to the Whole Building HAM Simulation of a Coated Room, *Energy Procedia.* 78 (2015) 1501–1506. doi:10.1016/j.egypro.2015.11.177.
- [29] ISO 15148:2002 Hygrothermal performance of building materials and products- Determination of water absorption coefficient by partial immersion, International Organization for Standardisation, (2002).
- [30] EN 1609:2013 - Thermal insulation for building applications - Determination of short term water absorption by partial immersion, European Committee for Standardisation, (2013).
- [31] C. Feng, H. Janssen, Hygric properties of porous building materials (II): Analysis of temperature influence, *Build. Environ.* 99 (2016) 107–118. doi:10.1016/j.buildenv.2016.01.016.
- [32] M. Krus, Moisture transport and storage coefficients of porous mineral building materials. Theoretical principles and new test methods. Technical Report, IRB-Verlag Stuttgart. (1996) 1–172.
- [33] M. Krus, K. Kießl, Determination of the moisture storage characteristics of porous capillary active materials, *Mater. Struct.* 31 (1998) 522–529. doi:10.1007/BF02481533.
- [34] F. Ochs, W. Heidemann, H. Müller-Steinhagen, Effective thermal conductivity of moistened insulation materials as a function of temperature, *Int. J. Heat Mass Transf.* 51 (2008) 539–552. doi:10.1016/j.ijheatmasstransfer.2007.05.005.
- [35] I. Torres, Rising damp in historical buildings walls, FCTUC ; PhD Thesis [in portuguese], 2004.
- [36] F. Björk, T. Enochsson, Properties of thermal insulation materials during extreme environment changes, *Constr. Build. Mater.* 23 (2009) 2189–2195. doi:10.1016/j.conbuildmat.2008.12.006.

- [37] Y. Liu, C. Ma, D. Wang, Y. Wang, J. Liu, Nonlinear Effect of Moisture Content on Effective Thermal Conductivity of Building Materials with Different Pore Size Distributions, *Int. J. Thermophys.* 37 (2016) 56. doi:10.1007/s10765-016-2062-0.
- [38] M. Campanale, L. Moro, Thermal Conductivity of Moist Autoclaved Aerated Concrete: Experimental Comparison Between Heat Flow Method (HFM) and Transient Plane Source Technique (TPS), *Transp. Porous Media.* 113 (2016) 345–355. doi:10.1007/s11242-016-0697-8.
- [39] M. Campanale, M. Deganello, L. Moro, Effect of Moisture Movement on Tested Thermal Conductivity of Moist Aerated Autoclaved Concrete, *Transp. Porous Media.* 98 (2013) 125–146. doi:10.1007/s11242-013-0136-z.
- [40] A.H.-C. Shin, U. Kodide, Thermal conductivity of ternary mixtures for concrete pavements, *Cem. Concr. Compos.* 34 (2012) 575–582. doi:10.1016/j.cemconcomp.2011.11.009.
- [41] A. Karamanos, S. Hadiarakou, A.M. Papadopoulos, The impact of temperature and moisture on the thermal performance of stone wool, *Energy Build.* 40 (2008) 1402–1411. doi:10.1016/j.enbuild.2008.01.004.
- [42] H.Q. Jin, X.L. Yao, L.W. Fan, X. Xu, Z.T. Yu, Experimental determination and fractal modeling of the effective thermal conductivity of autoclaved aerated concrete: Effects of moisture content, *Int. J. Heat Mass Transf.* 92 (2016) 589–602. doi:10.1016/j.ijheatmasstransfer.2015.08.103.
- [43] A. Abdou, I. Budaiwi, The variation of thermal conductivity of fibrous insulation materials under different levels of moisture content, *Constr. Build. Mater.* 43 (2013) 533–544. doi:10.1016/j.conbuildmat.2013.02.058.
- [44] M. Bianchi Janetti, T.A. Carrubba, F. Ochs, W. Feist, Heat flux measurements for determination of the liquid water diffusivity in capillary active materials, *Int. J. Heat Mass Transf.* 97 (2016) 954–963. doi:10.1016/j.ijheatmasstransfer.2016.02.047.
- [45] A. Silva, P.L. Gaspar, J. De Brito, Durability of current renderings: A probabilistic analysis, *Autom. Constr.* 44 (2014) 92–102. doi:10.1016/j.autcon.2014.04.002.
- [46] N. Belayachi, D. Hoxha, M. Slaimia, Impact of accelerated climatic aging on the behavior of gypsum plaster-straw material for building thermal insulation, *Constr. Build. Mater.* 125 (2016) 912–918. doi:10.1016/j.conbuildmat.2016.08.120.

- [47] P. Klößeiko, K. Varda, T. Kalamees, Effect of freezing and thawing on the performance of “capillary active” insulation systems: A comparison of results from climate chamber study to HAM modelling, *Energy Procedia*. 132 (2017) 525–530. doi:10.1016/j.egypro.2017.09.714.
- [48] T.C. Ling, K.H. Mo, L. Qu, J. Yang, L. Guo, Mechanical strength and durability performance of autoclaved lime-saline soil brick, *Constr. Build. Mater.* 146 (2017) 403–409. doi:10.1016/j.conbuildmat.2017.04.106.
- [49] B.P. Jelle, Accelerated climate ageing of building materials, components and structures in the laboratory, *J. Mater. Sci.* 47 (2012) 6475–6496. doi:10.1007/s10853-012-6349-7.
- [50] L. Graziani, E. Quagliarini, F. Bondioli, M. D’Orazio, Durability of self-cleaning TiO₂ coatings on fired clay brick façades: Effects of UV exposure and wet & dry cycles, *Build. Environ.* 71 (2014) 193–203. doi:10.1016/j.buildenv.2013.10.005.
- [51] H. Derbyshire, E.R. Miller, The photodegradation of wood during solar irradiation, *Holz Als Roh- Und Werkst.* 39 (1981) 341–350. doi:10.1007/BF02608404.
- [52] J.F. Mano, Creep-recovery behaviour of cork, *Mater. Lett.* 61 (2007) 2473–2477. doi:10.1016/j.matlet.2006.03.157.
- [53] I. Gnyp, S. Vaitkus, V. Keršulis, S. Vėjelis, Predicting the deformability of mineral wool slabs under constant compressive stress, *Constr. Build. Mater.* 23 (2009) 1928–1934. doi:10.1016/j.conbuildmat.2008.09.008.
- [54] I.Y. Gnyp, S. Vaitkus, V. Keršulis, S. Vėjelis, Experiments for the long-term prediction of creep strain of expanded polystyrene under compressive stress, *Polym. Test.* 29 (2010) 693–700. doi:10.1016/j.polymertesting.2010.05.011.
- [55] EN 1604:2013 - Thermal insulation products for building applications- Determination of dimensional stability under specified temperature and humidity conditions, European Committee for Standardisation, (2013).
- [56] EN 12089:2013 - Thermal insulating products for building applications. Determination of bending behaviour, European Committee for Standardisation, (2013).
- [57] EN 1607:2013 - Thermal insulation for building applications - Determination of tensile strength perpendicular to faces, European Committee for Standardisation, (2013).
- [58] ETAG 004- External Thermal Insulation Composite Systems with Rendering,

- European Organisation for Technical Approvals, (2011).
- [59] EN 826:2013 - Thermal insulation for building applications - Determination of compression behaviour, European Committee for Standardisation, (2013).
- [60] EN 12090:2013 - Thermal insulation for building applications - Determination of shear behaviour, European Committee for Standardisation, (2013).
- [61] EN 12430:2013 - Thermal insulation for building applications - Determination of behaviour under point load, European Committee for Standardisation, (2013).
- [62] EN 1605:2013 - Thermal insulation products for building applications- Determination of deformation under specified compressive load and temperature conditions, European Committee for Standardisation, (2013).
- [63] EN 12086:2013 - Thermal insulation for building applications - Determination of water vapour transmission properties, European Committee for Standardisation, (2013).
- [64] M.Zeitler, Thermal insulation materials for building equipment, in: M.R. Hall (Ed.), *Mater. Energy Effic. Therm. Comf. Build.*, Woodhead Publishing, Limited, Cambridge, 2010: pp. 274–303.
- [65] EN 12087:2013 - Thermal insulating products for building applications. Determination of long term water absorption by immersion, European Committee for Standardisation, (2013).
- [66] I. Flores-Colen, L. Silva, J. de Brito, V.P. de Freitas, Drying index for in-service physical performance assessment of renders, *Constr. Build. Mater.* 112 (2016) 1101–1109. doi:10.1016/j.conbuildmat.2016.03.034.
- [67] NP EN 1936:2008 -Métodos de ensaio para pedra natural. Determinação das massas volúmicas real e aparente e das porosidades total e aberta, (2008).
- [68] WUFI PC-Program for calculating the coupled heat and moisture transfer in building components.
- [69] ISO 10051:2008 Thermal insulation - Moisture effects on heat transfer - Determination of a thermal transmissivity of a moist material, International Organization for Standardisation, (2008).
- [70] IUPAC The International Union of Pure and Applied Chemistry, Reporting Physiosorption data for Gas/Solid Systems with Special Reference to the

- Determination of Surface Area and Porosity, *Pure Applied Chemistry*. 57 (1985) 603–619.
- [71] H.M. Künzeli, *Simultaneous Heat and Moisture Transport in Building Components One- and two-dimensional calculation using simple parameters -Technical Report*, 1995.
- [72] EN 15026: 2007 *Hygrothermal performance of building components and building elements - Assessment of moisture transfer by numerical simulation*; European Committee for Standardisation, (2007).
- [73] EN 1606:2013 - *Thermal insulation products for building applications - Determination of compressive creep*, European Committee for Standardisation, (2013).
- [74] ISO 4892-2:2013 - *Plastics -- Methods of exposure to laboratory light sources -- Part 2: Xenon-arc lamps*, International Organization for Standardisation, (2013).

Annex 1- Equipment used

This annex lists all equipment used to perform the experimental tests. It also identifies the section of the paper where the results have been reported.

Table A1: Mechanical tests equipment's

	Dimensional stability (section 2.1)	Bending (section 2.1)	Tensile (section 2.3)	Compression (section 2.3)	Shear test (section 2.5)	Point load (section 2.6)	Deformation (section 2.7)	Observations
Universal testing machine INSTRON 2530		×	×	×	×	×		Load cell: 30 kN (traction – class 0.5; compression – class 1).
Climatic chamber Fitoclima 300 EC 10	×	×	×	×	×	×		Accuracy T: ± 0.5 °C and φ : ± 0.02
Climatic chamber Walk in Fitoclima 13800 EDTU							×	Accuracy T: ± 1 °C and φ : ± 0.03
Digital caliper rule	×	×	×	×	×	×	×	Accuracy of ± 0.05 mm
LVDTHBM model WA- Electronic							×	Measurement range: 0 – 50 mm; accuracy ± 0.1 mm

Table A2: Hygrothermal tests equipment's

	Water vapour transmission (section 3.1.1)	Water absorption (section 3.1.2)	Thermal conductivity (section 3.1.3)	Open Porosity (section 3.2.1)	Free saturation water content (section 3.2.2)	Thermal conductivity variation with moisture (section 3.2.3)	Hygroscopic sorption curves (section 3.2.4)	Water absorption coefficient (section 3.2.5)	Drying (section 3.2.7)	Observations
Ventilated Owen			×			×	×		×	Accuracy of ± 2 °C
Climatic chamber Fitoclima 300 EC 10	×		×			×	×			Accuracy of T: ± 0.5 °C and ϕ : ± 0.02
Climatic chamber Walk in Fitoclima 13800 EDTU									×	Accuracy of T: ± 1 °C and ϕ : ± 0.03
Digital caliper rule				×			×	×	×	Accuracy of ± 0.05 mm
Balance	×	×	×		×	×	×	×	×	Accuracy of ± 0.01 g
Desiccator			×			×	×			Desiccant: Silica gel
Water tank			×						×	-
Water tank with level control		×						×		Water temperature accuracy of ± 3 °C
Chronograph	×	×						×	×	Accuracy of ± 5 s
Lambda meter NETZSCH HFM 436/3/1			×			×				Accuracy of $\pm 3\%$.
Hydrostatic balance				×						Accuracy of ± 0.05 g
Vacuum tank				×						-
Thermographic camera Flir, T640b		×								-
Container with desiccant	×									Desiccant: Silica gel
Drainer		×							×	-

Table A3: Durability tests equipment's

	Freeze-thaw cycles (section 4.1.1)	Ageing test (section 4.1.2)	Compressive creep (section 4.1.3)	Observations
Climatic chamber Fitoclíma 300 EC 10	×		×	Accuracy of T: ± 0.5 °C and φ : ± 0.02
Digital caliper rule	×		×	Accuracy of ± 0.05 mm
Balance	×			Accuracy of ± 0.01 g
Climatic chamber Walk in Fitoclíma 13800 EDTU			×	Accuracy T: ± 1 °C and φ : ± 0.03
Freeze-thaw tank Aralab Fitoterm 700GD25	×			-
Universal testing machine INSTRON 2530	×			Load cell: 30 kN (traction – class 0.5; compression – class 1)
Solarbox CO.FO.ME.GRA, model Solarbox 3000 e RH		×		-
LVDTHBM model WA- Electronic			×	Measurement range: 0 – 50 mm; accuracy ± 0.1 mm

Chapter 4

Importance of Moisture on the Thermal Performance

4.1 Introduction

Buildings are the largest energy consuming sector in the world. They account for over one-third of the total final energy consumption and are an equally important source of carbon dioxide (CO₂) emissions [1]. Article 9 of European Directive 2010/31/EU on the energy performance of buildings states that by 31 December 2020 all new buildings must have almost zero energy needs. For public buildings, this date has been brought forward to 2018. Therefore, energy efficiency in buildings is a priority, and the use of efficient technologies and solutions is essential, for both new buildings and for rehabilitation works. This ambitious objective will be more easily achieved through the use of eco-efficient insulation materials which can be easily recycled at the end of their life cycle.

Because of its resistance to adverse weather conditions, cork is the only thermal insulation material that can be used, uncoated, on the exterior [2]. It is a solution in line with the objectives established by Horizon 2020 for more sustainable development, thanks both to its known hygrothermal and mechanical properties and to it being a renewable material. Cork comes from the outer sheath of bark of the *Quercus Suber* L., a type of oak tree that is native to the western Mediterranean region, being a natural resource that grows without chemical herbicides, fertilizers or irrigation. After harvesting, cork is subjected to a cooking process that yields two product categories: natural cork, from which stoppers are produced, and granules, a by-product of the first quality cork [3,4]. Some raw cork is automatically rejected because it is poor quality. However, this rejected raw material is used to produce cork granules [5–7]. These are agglutinated with their own resin, suberin, in a pressure and heating process [8–10] to form a compact block of expanded cork, which then are cut with the desired thickness. This material has been the subject of environmental life cycle assessment by several authors [4,11]. Silvestre et al. [11] confirmed that expanded cork boards can be seen as a sustainable choice for the thermal insulation of buildings.

The heat and moisture transfer that occurs through the building envelope determines its hygrothermal performance and, consequently, its energy consumption [12]. If there is an excessive level of moisture in porous building materials then, besides its effect on the hygrothermal properties of building materials, it can lead to the development of anomalies like such as frost attack, steel corrosion, timber rot, cracking and mould growth.

The combined effect of surface condensation, wind-driven rain, drying, and the hygrothermal behaviour of the exterior wall layer can lead to high surface moisture content [13]. As

concluded by Coelho et al. [14], wind-driven rain has a key influence on the hygrothermal behaviour of high capillary water uptake walls, such as solid brick walls. In their work, Finken et al. [15] conclude that the facade should be protected against driving rain when rehabilitating solid bare masonry walls using internal capillary active insulation. Regarding concrete walls, in which water seepage is a common problem, Yu et al. [16] developed an engineered cementitious composite for waterproofing applications in concrete walls. In their review about the implemented approaches to waterproof concrete, Muhammad et al. [17] concluded that the technique adopted by the majority of the researchers is the use of waterproofing surface coatings. Therefore, researchers and building industry players have been developing construction techniques to prevent water seepage through the building envelope.

Since expanded cork board of medium density ($140\text{--}160\text{kg/m}^3$) is used as an uncoated wall cover, without any protection, it is not technically feasible to prevent water absorption. In addition to water absorption by capillarity, common to most of building materials in current use, rainwater gets into the expanded cork boards by percolation through the channels created by the spaces between the cork granules. The wind-driving effect (whereby the wind causes the rain to fall obliquely and forces it against the windward facade of buildings [18]) probably helps this process of water penetration. It should be noted that those small channels might also help the incoming rainwater to seep out of the material more easily. Previous work performed by the authors [19] confirmed that once expanded cork board was fully saturated and left to dry it lost more than a half of its initial water content in the first nine hours of drying, mostly due to the action of gravity. The influence of gravity and water percolation are considered negligible in the drying process of most porous building materials and therefore they have not been regarded as very relevant in heat and moisture transfer modelling tools.

The literature contains various numerical simulation tools that can handle the coupled heat, air and moisture phenomena and accurately capture the hygrothermal behaviour of building components and their influence on the internal environment. To study the moisture transport in building walls and the interface phenomena, Freitas et al. [20] developed a finite difference computer program based on the Luyk and Philip-De Vries theory. The numerical results were found to be satisfactory when compared with experimental water content profiles obtained by using gamma-ray equipment. Künzle [21] developed a calculation method for one and two dimensional simultaneous heat and moisture transport in multi-layered building components, using vapour pressure and relative humidity as driving potentials for vapour and liquid transport. The model also takes into account rain and solar radiation so that the effect

of the weather conditions on the heat and moisture transfer in building components could be calculated more realistically. The validation of the model against several experimental results shows its relative suitability for simulating two-dimensional moisture transport processes in building components. Škerget and Tadeu [22] developed a two-dimensional time dependent boundary element formulation to solve the coupled heat and mass transfer through a porous medium. The numerical results were found to be in good agreement with benchmark examples, even in the presence of highly nonlinear coupled heat and moisture transfer. The authors concluded that, in this case, because of the several orders of magnitude difference between heat and mass diffusion coefficients, the time and length scales are very different, and the numerical solution becomes arduous. More recently, Škerget et al. [23] further developed that formulation to include the airflow through the porous medium. A good agreement was achieved between the numerical results and benchmark examples, indicating that this technique can be used to simulate the hygrothermal performance of building envelope components. Evrard et al. [24] simulated the hygrothermal performance of a brick wall insulated on its interior surface with LH plaster, which was coated with a traditional lime render and no vapour barrier was considered. The simulations were performed using WUFI® Pro. The liquid transfer coefficients were calculated based on the absorption coefficient, following Künzle's exponential law. The results showed that results can be unrealistic if the absorption coefficient of materials is neglected, especially when the wall is exposed to high levels of driving rain.

Besides the complexity of the algorithms, they all require a reliable set of properties of porous materials that are very difficult to evaluate and not always available in the literature. The experimental approach is an alternative to the numerical simulation tools.

Some researchers conducted their studies using external test cells or in situ monitoring. Ibrahim et al. [25] used the south wall test cell of a small-scale building to evaluate the hygrothermal performance, under real weather conditions, of an insulating rendering based on silica-aerogels. The results were used to validate a numerical model developed using WUFI® pro 5.1. Bianco et al. [26], used a test cell located in Turin and a long term monitoring campaign to assess both the biometric parameters and the energy-related issues of a vertical greenery module system. Barreira and Freitas [27] monitored a building with four facades covered with ETICS for one year to assess its hygrothermal behaviour, that is, to study the influence of cardinal orientation on surface humidification induced by wind-driven rain and condensation.

Although the use of exterior test cells or in-situ monitoring will yield results for real weather conditions, these methods require long term monitoring, with long term availability of the measurement devices. An alternative for both steady-state and transient conditions is to use a hot-box, which can test full-scale samples such as construction elements of building envelopes. It has many advantages: the desired conditions in both chambers are easily imposed; transient or steady-state regimes that simulate winter and summer weather conditions can be studied in a relatively short period of time; and the same test conditions can be replicated for other wall assemblies.

Research on building elements using a hot-box apparatus has been carried out by several authors. Gao et al. [28] focused their research on heat transfer through two types of walls made of small-size hollow concrete blocks in dynamic conditions. To validate a simplified numerical tool developed by the authors, a hot-box apparatus was used to validate the numerical model. Adam and Jones [29] defined the thermal properties of stabilized hollow earth blocks using the guarded hot-box method. A calibrated hot-box was used by Wakili and Tanner to study the U-value of a dried wall made from vertically perforated porous clay bricks [30]. The heterogeneity and rough surface characteristics of wall blocks made of pumice aggregate concrete, which are increasingly used as a masonry wall unit in Turkey, led Kus et al. [31] to conduct a study on the hygrothermal performance of these blocks using the calibrated hot-box method. Nardi et al. [32] validated the thermographic methods used to determine the thermal transmittance of building components by imposing different operational conditions on the controlled environment of a guarded hot-box.

In this work, a hot-box is adapted to simulate the action of driving rain. A wetting apparatus that creates horizontal water spray was developed to study the hygrothermal behaviour of medium density expanded cork boards under exposure to various weather conditions, in both dry and wet conditions.

The main purpose of this study is to assess the importance of moisture content on the thermal behaviour of a wall coated with medium density expanded cork boards when exposed to rain. Since expanded cork board is a heterogeneous aggregated porous material, when it rains the water gets inside and percolates throughout the wall under the action of gravity. As all the phenomena involved are complex and difficult to model numerically, experimental tests on a full-scale model are used to study its hygrothermal behaviour in the presence of rain. Then the importance of moisture content to the wall's thermal behaviour is quantified using an

analytical model that simulates the heat transfer phenomenon and the results compared with those obtained experimentally.

This chapter first describes the analytical model used to simulate the transient heat conduction. The test procedures, specimens and data acquisition chain are also described. Steady- and unsteady-state conditions for both the winter and summer environment are studied for the dry and wet conditions. Finally, the experimental results are presented and compared with the analytical ones.

4.2 Methodology

To study the influence of varying moisture content on the heat transfer, a wooden wall covered with uncoated medium density expanded cork was tested in a hot-box, for both dry and wet conditions. This equipment is composed of three parts: a chamber that simulates the outside environment (OUT), a chamber that simulates the internal conditions (IN) and a frame that holds the test specimen that is placed between these two chambers. The tests were performed for both steady and unsteady conditions (summer and winter conditions). All the tests simulated the exposure of the wall to dry and wet weather. The experimental results were compared with those obtained analytically, using a simple model that only takes into account the transient heat diffusion by conduction phenomena in a multilayer system. This analytical model was solved by imposing the temperature on the outer and inner surfaces.

This section describes the analytical model for conduction and the experimental set-up.

4.2.1 Analytical model for conduction

Figure 4-1 shows a multilayer system consisting of m layers of infinite size. This system is subjected to temperatures t_{0t} and t_{0b} on the top and bottom external surfaces. The layers are assumed to be infinite in the x and z directions. The thermal properties and thicknesses (h_j) of the various layers vary.

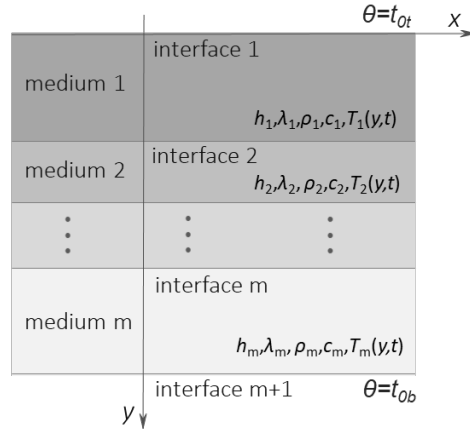


Figure 4-1: Geometry of the multilayer system.

The heat transfer by conduction in each layer is given by the following equation:

$$\lambda_j \frac{\partial^2 T(t, y)}{\partial y^2} = \rho_j c_j \frac{\partial T(t, y)}{\partial t} \quad (4-1)$$

in which t [h] is the time, $T(t, y)$ [K] is the temperature, j [1,2,3...] identifies the number of the layer, λ_j [W/(m K)] is the thermal conductivity coefficient, ρ_j [kg/m³] is the density and c_j [J/(kg K)] is the specific heat of the layer j .

Applying the Fourier transform to eqn. (4-1) in the time domain, the following expression is obtained:

$$\left(\frac{\partial^2}{\partial y^2} + \frac{-i\omega}{K_j} \right) \hat{T}(\omega, y) = 0 \quad (4-2)$$

in which $i = \sqrt{-1}$, $K_j = \lambda_j / (\rho_j c_j)$ [m²/s] is the diffusivity of the layer j , and ω [rad/s] is the frequency.

The heat field in the multilayer system is determined by adding the incident field to the reflected and transmitted heat field generated by each layer, at each interface, and modelled by a set of surface terms. The amplitude of these surface terms within each layer and each interface is defined by imposing continuity of temperatures and normal flows between layers. For layer j the surface term on the upper and lower surface is given by:

$$\hat{T}_{j1}(\omega, y) = E_{0j} \frac{E_{j1}}{v_{0j}} A_{0j}^t \quad (4-3)$$

$$\hat{T}_{j2}(\omega, y) = E_{0j} \frac{E_{j2}}{v_{0j}} A_{0j}^b \quad (4-4)$$

in which, $E_{0j} = \frac{1}{\lambda_j}$, $E_{j1} = e^{-iv_{0j}|y-\sum_{l=1}^{j-1} h_l|}$, $E_{j2} = e^{-iv_{0j}|y-\sum_{l=1}^j h_l|}$, $v_{0j} = \sqrt{\frac{-i\omega}{K_j}}$ and h_l is the thickness of the layer l ; A_{0j}^t and A_{0j}^b are the amplitudes (initially unknown).

Imposing the temperatures \hat{t}_{0t} and \hat{t}_{0b} on the top and bottom surfaces, respectively, and ensuring temperature and heat flux continuity at the $(m-1)$ interfaces, between layers, will lead to a system of $2m$ equations. \hat{t}_{0t} and \hat{t}_{0b} are defined through the Fourier transform of t_{0t} and t_{0b} in the time domain.

$$\begin{bmatrix} \frac{1}{\lambda_1 v_{01}} & \frac{e^{-iv_{01}h_1}}{\lambda_1 v_{01}} & \dots & 0 & 0 \\ e^{-iv_{01}h_1} & -1 & \dots & 0 & 0 \\ \frac{e^{-iv_{01}h_1}}{\lambda_1 v_{01}} & \frac{1}{\lambda_1 v_{01}} & \dots & 0 & 0 \\ \dots & \dots & \dots & \dots & \dots \\ 0 & 0 & \dots & -1 & e^{-iv_{0m}h_m} \\ 0 & 0 & \dots & \frac{1}{\lambda_1 v_{0m}} & -\frac{e^{-iv_{0m}h_m}}{\lambda_m v_{0m}} \\ 0 & 0 & \dots & \frac{e^{-iv_{0m}h_m}}{\lambda_m v_{0m}} & \frac{1}{\lambda_m v_{0m}} \end{bmatrix} \begin{bmatrix} A'_{01} \\ A^b_{01} \\ \dots \\ A^b_{0m} \\ A'_{0m} \end{bmatrix} = \begin{bmatrix} \hat{t}_{0t} \\ 0 \\ 0 \\ \dots \\ 0 \\ 0 \\ \hat{t}_{0b} \end{bmatrix} \quad (4-5)$$

The system is solved to define the amplitude of the surface terms at each interface, in which the temperatures and heat fluxes at each layer j are given by eqn. (4-6) and eqn. (4-7), respectively.

$$\hat{T}(\omega, y) = E_{0j} \left(\frac{E_{j1}}{v_{0j}} A_{0j}^t + \frac{E_{j2}}{v_{0j}} A_{0j}^b \right) \quad \text{if} \quad \sum_{l=1}^{j-1} h_l < y < \sum_{l=1}^j h_l \quad (4-6)$$

$$\frac{\partial \hat{T}}{\partial y}(\omega, y) = E_{0j} (-iE_{j1} A_{0j}^t + iE_{j2} A_{0j}^b) \quad \text{if} \quad \sum_{l=1}^{j-1} h_l < y < \sum_{l=1}^j h_l \quad (4-7)$$

The responses in the time domain are obtained by applying an inverse Fourier transform (Fast Fourier Transform type). To prevent the phenomenon of aliasing, complex frequencies are used. These solutions do not require any kind of spatial domain discretization. Since the static response is obtained by limiting the frequency to zero and ensuring that the high frequency contribution to the response is small, no constraint is placed on the source time dependence. This goes beyond some of the limitations of other methods that require the use of simplifications, such as layer discretization in a large number of identical thin layers [33,34].

4.2.2 Experimental Set-up

This section describes the procedure used to perform the experimental tests and to record the temperatures and heat fluxes within a multilayer system. The test procedures, test specimens and data acquisition chain are described in the following sections.

4.2.3 Test procedures

First, the specimen (described in section 4.2.4) was prepared and installed inside the hot-box. Before starting the measurements, a long conditioning period was kept, imposing $(23 \pm 2)^\circ\text{C}$ and 0.5 ± 0.05 of relative humidity.

Afterward, three test conditions were considered to simulate both steady and unsteady/transient conditions (winter and summer conditions), as shown in Figure 4-2.

- Under the steady-state condition, the external (OUT chamber) and the internal (IN chamber) temperatures were maintained at 0°C and 20°C , respectively (Figure 4-2a).
- Under the winter unsteady-state condition, the IN chamber was kept at 20°C , while in the OUT chamber the temperatures varied periodically between -10°C and $+10^\circ\text{C}$, according to Figure 4-2 b).
- Under the summer unsteady-state condition in the OUT chamber, a periodic 24 h cycle with temperatures between $+15^\circ\text{C}$ and $+35^\circ\text{C}$ was set. In this case, the heating system in the IN chamber was turned off. The temperature in the IN chamber is a response to the induced temperature cycles in the OUT chamber. Figure 4-2c illustrates the imposed temperatures evolution.

A ventilation system was used to prevent air stratification. To mitigate the effect of the variation in heat loss through the hot chamber envelope, the room where the hot-box is installed was kept at $(20 \pm 2)^\circ\text{C}$ throughout the test.

Rainy periods were simulated by setting up a water system in the OUT chamber to wet the test specimen with a spray flow of $1 \text{ L}/(\text{m}^2 \text{ min})$, following the recommendations given in ETAG 004 [35] for testing ETICS. The system is composed of 12 sprinklers of $0.5 \text{ L}/(\text{m}^2 \text{ min})$, equally spaced 60 cm horizontally and 70 cm vertically. To estimate the mean water content of the wall, preliminary tests were performed and sub-blocks removed from the wall and weighed. The water content of each sub-block was then calculated.

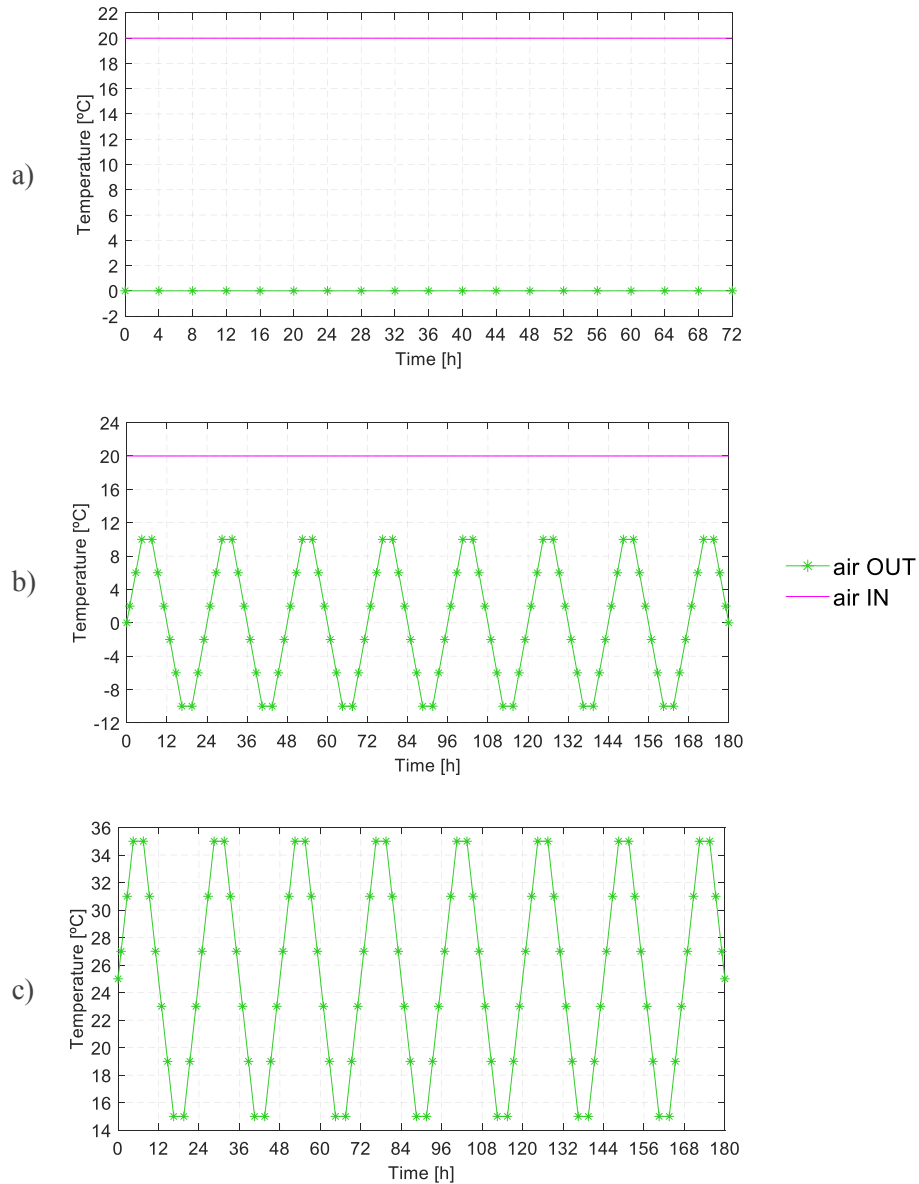


Figure 4-2: Set-point of temperatures for both chambers (the marked line relates to the OUT chamber while the solid line relates to the IN chamber): a) Steady-state; b) Winter unsteady-state condition; c) Summer unsteady-state condition (the temperature in the IN chamber was not imposed).

4.2.4 Test specimen

An 18 mm OSB panel (2200×2400) mm² (height × width), supported by a wood frame, was coated with (500×1000×70) mm³ medium density expanded cork boards (Figure 4-3a). A waterproofing mortar, 5 mm thick, was used to bond the boards to the OSB panel. This wall was built into the hot-box frame. The medium density expanded cork boards were numbered individually, from 1 to 18 (Figure 4-3b).

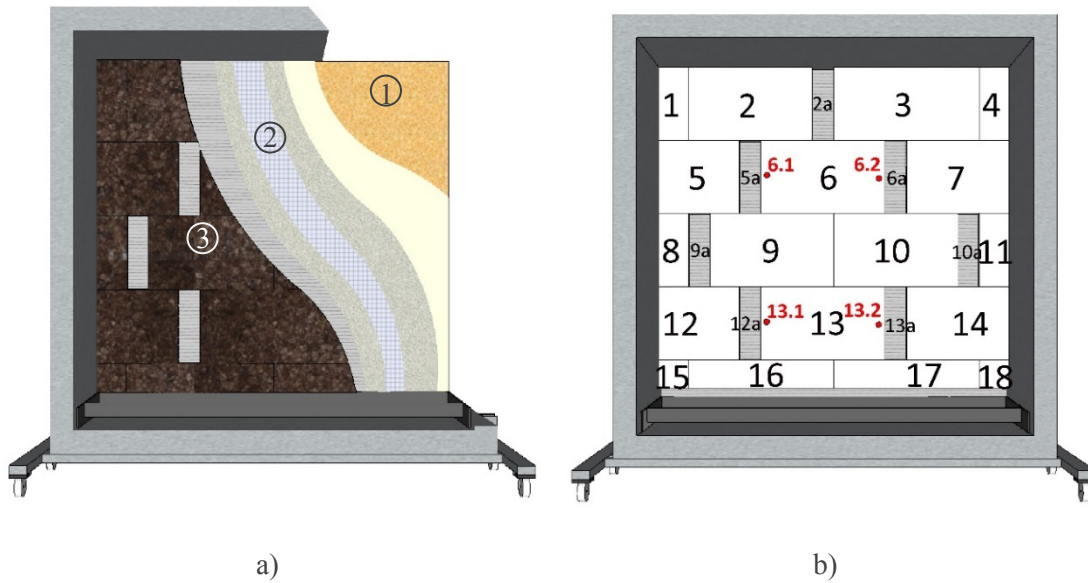


Figure 4-3: Wall test specimen: a) Composition: 1- OSB; 2- waterproofing and bonding mortar; 3- medium density expanded cork board); b) Numbering of the expanded cork board panels and of the sub-blocks; Measuring points.

To evaluate the board's water content after each wetting test, sub-blocks were cut from panels 2, 5, 6, 9, 10, 12 and 13 with nominal dimensions of (500×15×70) mm³, and these were numbered 2a, 5a, 6a, 9a, 10a, 12a and 13a. The water content of the sub-blocks at reference conditions was determined by placing them in a climatic chamber at $T = (23 \pm 2) ^\circ\text{C}$, 0.5 ± 0.05 relative humidity, until constant mass was achieved, and they were then weighed. Their mass m , was then calculated. To obtain the dry density ($\rho_0 = m_0/V$ [kg/m³]), they were left to dry for 72 h in a ventilated oven at 70 °C. At the end of that time, each sub-block was weighed to obtain its mass m_0 [kg], and its volume V [m³] was calculated. The moisture content was then obtained as $u = (m - m_0)/m_0$ [kg/kg].

All relevant material properties are presented in Table 4-1.

Table 4-1: Material properties (mean values).

	^(a) OSB	^(a) Bonding mortar	Expanded cork board
λ [W/(m K)]	0.130	0.800	0.042±0.0011 ^(b)
c [J/(kg K)]	1500	850	1530±105 ^(c)
ρ [kg/m]	595	1350	156±4.95 ^(d)
u [kg/kg]	-	-	0.022±0.001 ^(e)

^(a) *Wufi* materials database [36].

^(b) Thermal conductivity obtained following the procedure described in EN 12667:2001 [37], using the guarded hot plate *Meter-Meßtechinck EP500*, at reference conditions.

^(c) Specific heat obtained by differential scanning calorimetry, following the ratio method.

^(d) Mass density determined using the procedure described in EN 1602:2013 [38].

^(e) Water content of the sub-blocks evaluated as described above.

4.2.5 Data acquisition chain

Thermocouples and heat flux sensors were installed to monitor the testing specimen in several measurement points. Four groups of thermocouples (numbered 6.1, 6.2, 13.1, 13.2 - the first index is the number of the panel on which the group was placed) were installed within the test specimen (Figure 4-3b), away from the expanded cork panel lateral boundaries. Each group consists of seven thermocouples: on both surfaces of the test specimen and at different depths, as illustrated in Figure 4-4. Four heat flux sensors were installed on the OSB surface, at the same relative thermocouples positions.

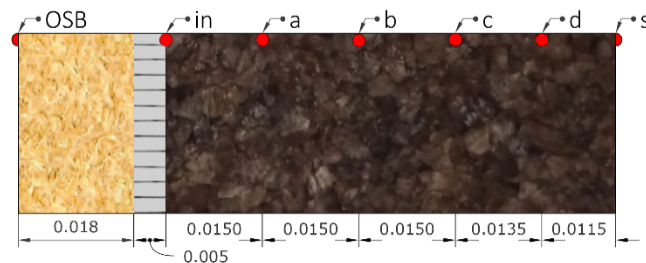


Figure 4-4: Cross section of the specimen. Position identification of the thermocouples and heat flux sensors along the constructive solution.

The results will only be presented for position 6.1, since the measurements for the other groups of thermocouples showed similar behaviour and are therefore not included in this work.

In addition to measuring the ambient temperature of the air along the centre line of each chamber in front of the specimen, a vertical line of 3 thermocouples spaced 51 cm apart was also installed. All thermocouples were type T (copper), with a diameter of less than 0.25 mm and a maximum measurement uncertainty of ± 0.16 °C. The heat flux sensors are ultrathin flat plate sensors. The accuracy of the heat flux sensors is $\pm 5\%$. Data were recorded at 2-minute intervals, both for the thermocouples and for the heat flux sensors, by a data logger system, Agilent 34980A. The measurement system was calibrated beforehand by an accredited laboratory.

4.3 Heat transfer under dry conditions

This section examines the heat transfer under dry conditions. The temperatures and heat fluxes obtained for the steady-state condition are first presented, then, a transient summer condition is imposed.

All analytical results are compared with the experimental data, using either the surface temperatures or the air temperatures once the thermal surface resistance has been evaluated using the experimental data (Table 4-2 relates the receiver number to the thermocouple positions (Figure 4-4)).

The time lag and the decrement factor provided by the test specimen are calculated, both experimentally and analytically. The analytical results were obtained using the material properties listed in Table 4-1 and imposing the boundary conditions t_{0t} and t_{0b} , using either the air or specimen surface temperature.

Table 4-2: Receiver numbering used in the analytical model.

Thermocouple position (as in Figure 4-4)	OSB	in	a	b	c	d	s
Receivers	r1	r2	r3	r4	r5	r6	r7

4.3.1 Steady-state conditions

Constant temperatures of 0 °C and 20 °C were programmed in the OUT and in the IN chamber, respectively (see Figure 4-2a), under dry conditions.

Figure 4-5 presents both the experimental and analytical temperatures for the thermocouple group and heat fluxes (position 6.1). The analytical results were found by imposing the measured surface temperatures (6.1_OSB and 6.1_s). The temperatures recorded in the air are also given.

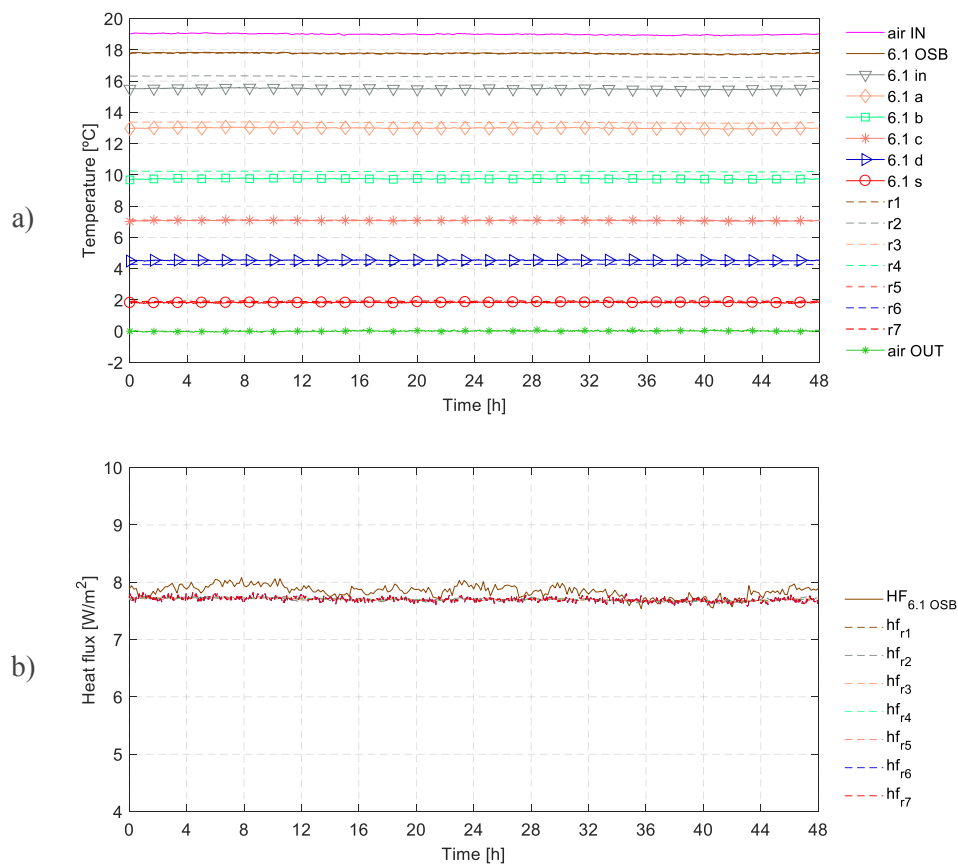


Figure 4-5: Heat transfer under dry steady-state conditions: a) Temperatures; b) Heat fluxes.

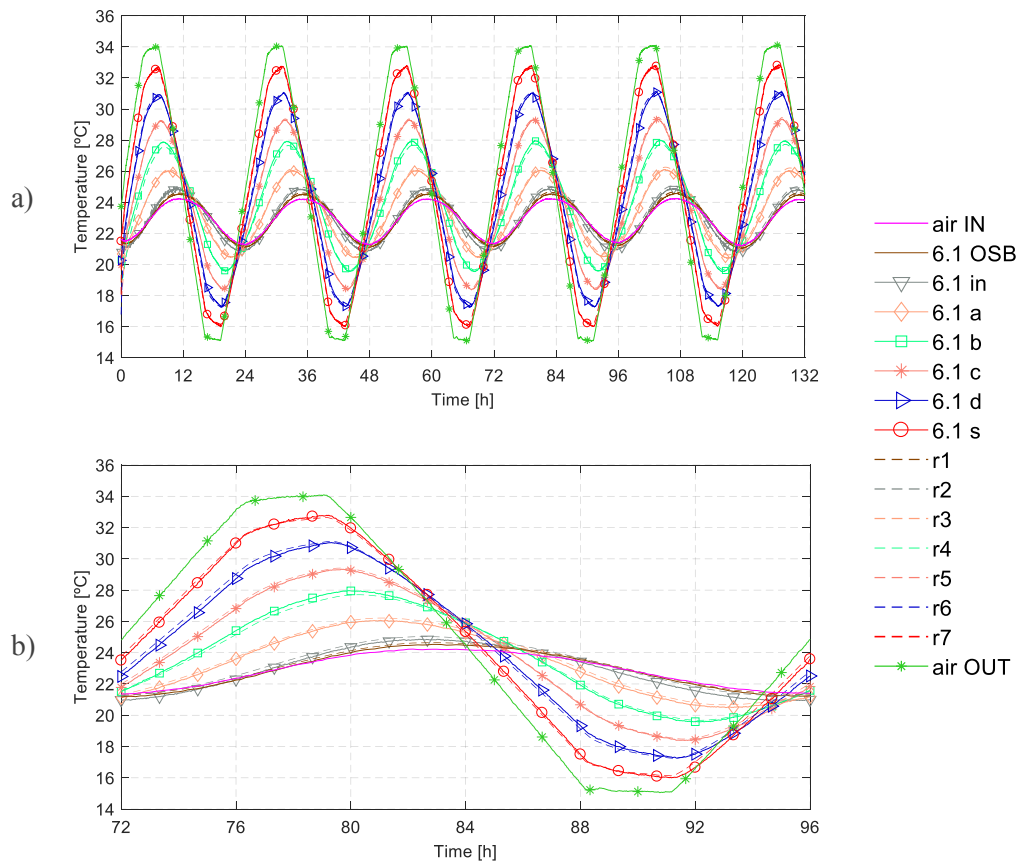
As can be seen in Figure 4-5a, the analytical and the experimental temperatures show good agreement. The largest difference, with a mean value of 0.4 °C is obtained for point “in”, located at the expanded cork board-bonding mortar interface.

Figure 4-5b shows the experimental heat flux registered at 6.1_OSB. The experimental readings are similar to the heat fluxes obtained through the analytical solutions.

The recorded experimental heat flux obtained in the steady-state condition tests were used to calculate the thermal surface resistance for both the outer and inner sides of the wall. Values of $R_{si} = 0.16 \text{ (m}^2 \text{ K)/W}$ for the inner and $R_{se} = 0.24 \text{ (m}^2 \text{ K)/W}$ for the outer surfaces were recorded. To simulate these thermal surface resistances in the analytical model, two fictitious layers of air with 3.0 mm were considered. An equivalent thermal conductivity of $\lambda_{airin} = 0.0188 \text{ W/(m K)}$ and $\lambda_{airout} = 0.0125 \text{ W/(m K)}$, was respectively used in inner and outer layer of the model. The density and the specific heat of air take the values of $\rho = 1.2928 \text{ kg/m}^3$ and $c = 1000 \text{ J/(kg K)}$.

4.3.2 Unsteady-state conditions

Figure 4-6 presents the experimental and analytical temperatures and heat fluxes obtained for unsteady-state summer condition (Figure 4-2c), in the first 132 h of testing. A zoom of the results for the period $72 \text{ h} \leq t \leq 96 \text{ h}$ is included to provide a detailed view. The analytical results were found by imposing the measured air temperatures.



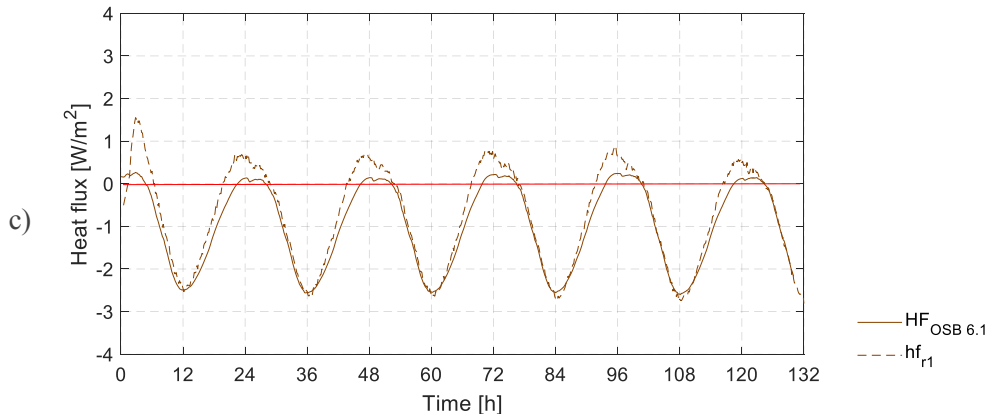


Figure 4-6: Experimental and analytical results in dry conditions a) Temperatures for the first 132 h of testing; b) Temperatures for $72 \text{ h} < t < 96 \text{ h}$; c) Heat fluxes.

The analytical results obtained using two additional fictitious layers (3.0 mm thick) present a very good agreement with the experimental results. A maximum difference of 0.2°C between analytical and experimental temperatures was obtained for position b (receiver r4 and thermocouple 6.1_b).

Regarding the heat fluxes (Figure 4-6c), when positive values were obtained, i.e. the heat transfer on the inner surface was towards the cold chamber, the analytical values are approximately 0.5 W/m^2 higher than the experimental ones. When the heat flux direction was reversed (heading towards the IN chamber), the experimental and numerical results show a good agreement.

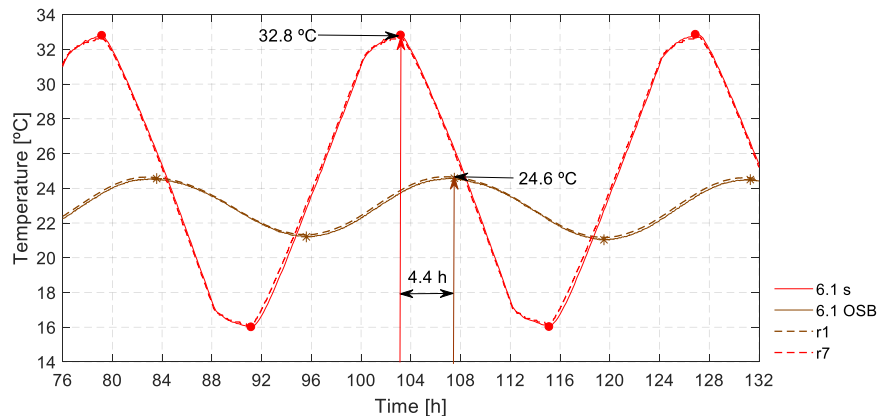


Figure 4-7: Time lag and decrement factor provided by the constructive solution under dry conditions.

Analysing the experimental responses through the wall, the existence of a time lag is well defined. Indeed, the time that the heat wave takes to propagate from the outer surface to the inner surface is very visible. This phenomenon is associated with a decreasing amplitude of

temperatures from the outer to the inner surface; the ratio between inner and outer surface temperature is called the decrement factor. Figure 4-7 shows this phenomenon for the time domain of 78-132 h. The mean time lag exhibited is 4.4 h, with a decrement factor of 0.75.

4.4 Heat transfer under wet conditions

As previously mentioned, tests under wet conditions were performed to analyse the influence of moisture on the heat transfer through the wall. To perform the wet tests, the wall was wetted for 1 h at a flow rate of 1 L/(m² min). To estimate the water content of the wall after being wetted, a preliminary test using 7 sub-blocks (2a to 13a) was performed. The registered initial water content, u , was 0.0886 ± 0.0006 kg/kg. It was found that the initial water content of the expanded cork boards after wetting is similar to that found 8 h after being immersed in water and left to dry, according to previous experimental work performed by the authors [19].

Next are shown the experimental temperatures and heat fluxes, first for steady-state wet conditions, and afterwards for transient conditions; both winter and summer wet conditions were analysed. By comparing the analytical results with the experimental ones for the three situations, the importance of the moisture content in the heat transfer was assessed. Notice that analytical simulations assume that the moisture content of the material does not change. Following this approach, pronounced deviations between the experimental and analytical results would mean that the moisture has a strong impact in the heat transfer. If the results are similar, the conclusion is the opposite.

4.4.1 Steady state conditions

Figure 4-8a presents the temperature evolution across the wall when constant temperature conditions according to Figure 4-2a were imposed, while Figure 4-8c shows the heat fluxes. After reaching a steady-state condition, the wall was subjected to wetting at $t = 28.8$ h, for 1 h, with water at (17 ± 0.5) °C. Comparing the first few hours, temperature differences were found as shown in Figure 4-8a. The rain system installation led to a change in the ventilation system, thus the air flow inside the chamber was changed, resulting in a slight temperature increase inside the OUT chamber. Also, the surface thermal resistance changed to a value of $R_{se} = 0.13$ (m² K)/W ($\lambda_{airout} = 0.0231$ W/(m K)). To evaluate the importance of moisture in the heat transfer, Figure 4-8 includes both the experimental and the analytical results. The analytical simulations were obtained by imposing the measured surface temperatures.

As in the dry conditions, a very good agreement was obtained between the experimental and the analytical results after initial stabilization. The largest difference between them was registered at position “in”, with a mean value of 0.6 °C (Figure 4-8a).

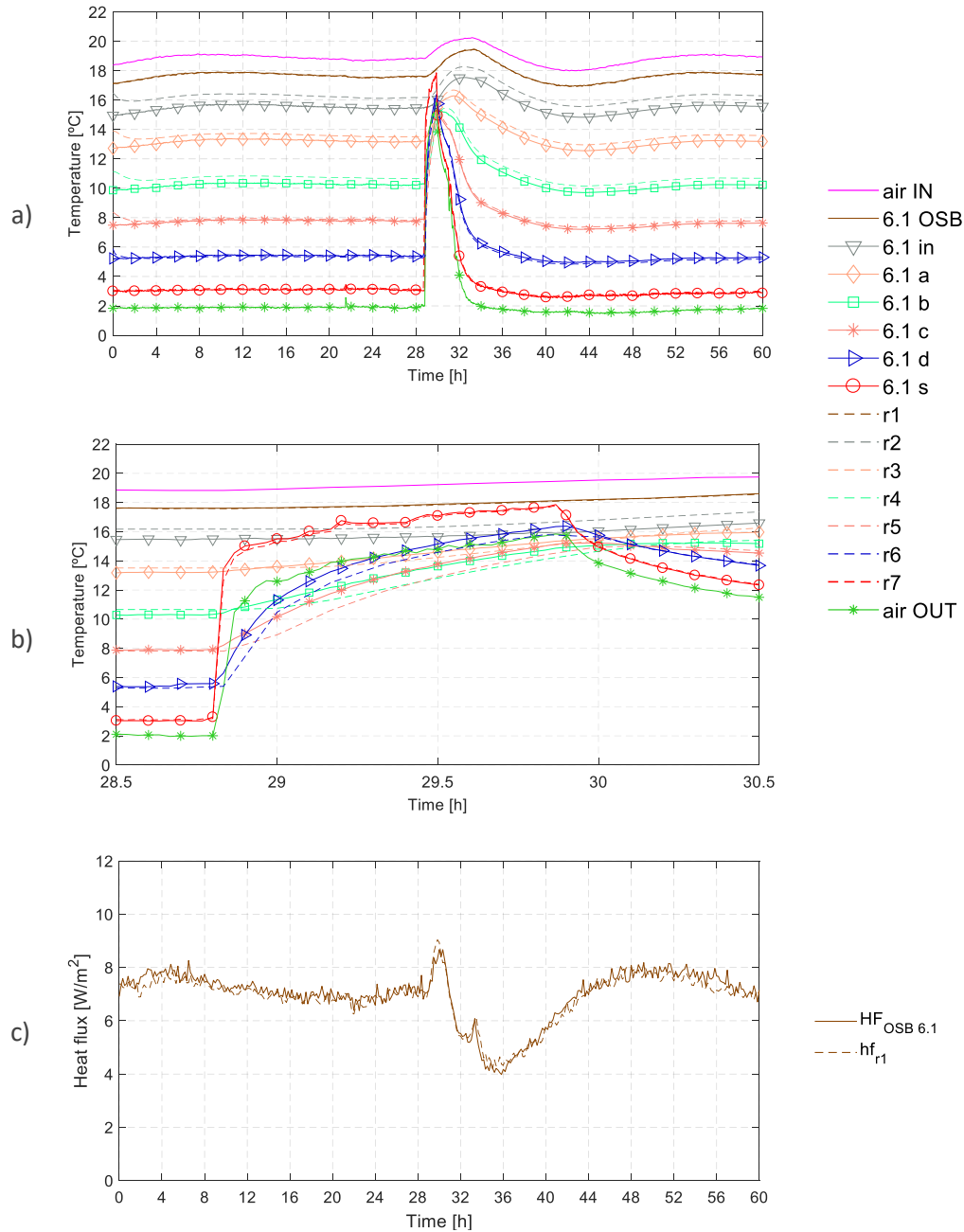


Figure 4-8: Experimental (solid lines) and analytical (dashed lines) results in wet conditions
a) Temperatures for the first 68 h of testing; b) Temperatures for 28.5 h < t < 30.5 h; c) Heat fluxes.

For better understanding of the importance of the wetting period, Figure 4-8b presents the experimental and analytical temperatures for the wetting period and just after wetting.

A sudden increase in the temperature occurred during the wetting phase because of the water temperature, $(17 \pm 0.5)^\circ\text{C}$, at the outer layer of the expanded cork boards. At measurement point 6.1_s the temperature rose from 3°C to 13.4°C immediately after the wetting period started. After this initial period, the temperature increased at a slower rate, rising from 13.4°C up to the maximum value of 17.8°C . A sudden increase in the temperature is also noticeable at the thermocouples placed at 10 mm (6.1_d), 25 mm (6.1_c) and 40 mm (6.1_b) from the surface. This temperature increment indicates that the water penetrated 40 mm in the first 4 min. At position 6.1_a, the initial temperature rise is negligible and at interface (6.1_in), there is none. The temperature increase in these positions is only visible after a longer period of time. There are two different physical mechanisms involved: temperature rise due to the water penetration, and temperature rise due to heat conduction (a phenomenon linked to the moisture transfer). The analytical model does not take into account the coupling of the heat and moisture transfer phenomena and assumes that the material properties remain constant.

At positions 6.1_a and 6.1_in the analytical and experimental temperatures rise at the same rate (parallel lines), indicating that there was no influence from significant moisture variation there, and thus any variation in the hygrothermal properties can be assumed to be negligible. For positions 6.1_d, 6.1_c and 6.1_b, the experimental temperatures rise at a higher rate than the analytical ones. This indicates that the water reached these depths. It did so by percolating through the ICB along the channels created by the space between cork granules and should not be confused with moisture transport phenomenon. Once the drying process begins, the analytical and experimental temperatures decrease at same rate, illustrated by parallel lines. The registered temperature differences are similar to those found before wetting. It can be concluded that the temperature difference observed during wetting is mainly caused by the temperature of the water that reached the surface and penetrated into the material.

Regarding the heat fluxes, presented in Figure 4-8c, a very good agreement was obtained between the experimental and the analytical results.

At the end of the test, the water content was measured again in the same sub-blocks, and the result was 0.0248 ± 0.0048 kg/kg. This value is close to the one obtained for the reference conditions and is stated in Table 4-1.

4.4.2 Unsteady state conditions

The same test specimen was subjected to experimental transient conditions (summer and winter), for both dry and wet environments. Again, analytical results were obtained using the same material properties listed in Table 4-1, imposing the surface temperatures during the test.

4.4.2.1 Summer environment conditions

The temperature cycles were performed as illustrated in Figure 4-2c, for summer conditions, for 180 h. The wall was sprayed with water at instant $t = 81.4$ h (point W in Figure 4-9), for 1 h, at the beginning of the descending temperature cycle, following the procedure described above. The water temperature was (22 ± 0.5) °C. Figure 4-9 presents the experimental temperatures.

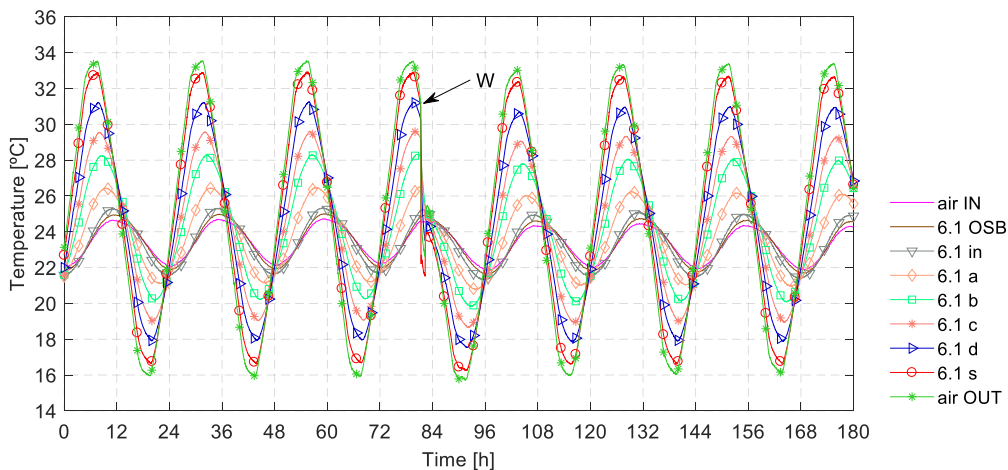


Figure 4-9: Experimental temperatures registered for unsteady summer conditions in the first 180 h; water spray lasting 1 h occurred at instant $t = 81.4$ h.

As can be seen in Figure 4-9, the temperature in the air of the cold chamber oscillated between +16 °C to +33.5 °C. Right after the wall was wetted, the air temperature in the cold chamber varied from 15 °C to 32.2 °C. As before, it can be seen that the temperature is only affected during wetting and the first few hours of the drying period. To illustrate this behaviour Figure 4-10a presents a 24 h cycle before wetting (cycle 1: $56 \text{ h} \leq t < 80 \text{ h}$) superimposed with a 24 h cycle that includes the wetting period (cycle 2: $80 \text{ h} \leq t < 104 \text{ h}$). In Figure 4-10b, the same before-wetting 24 h cycle is now superimposed with the second after-wetting 24 h cycle (cycle 3: $104 \text{ h} \leq t < 128 \text{ h}$).

Figure 4-10a shows that in the first hours after wetting the difference in temperature between cycle 1 and cycle 2 is relevant, although this decreased over time. Part of that difference is attributed to the variation in the air temperature within the OUT chamber during wetting.

Figure 4-10b, which includes cycle 3, shows that the temperature along the wall after wetting was slightly lower in the first 5 h of the cycle than that observed in cycle 1. It should be noted that the air temperature was also lower. As time progressed, the air temperature within the chamber after wetting tended to return to the air temperature before wetting. Simultaneously, the temperature at the various thermocouples tended to reach those registered before wetting.

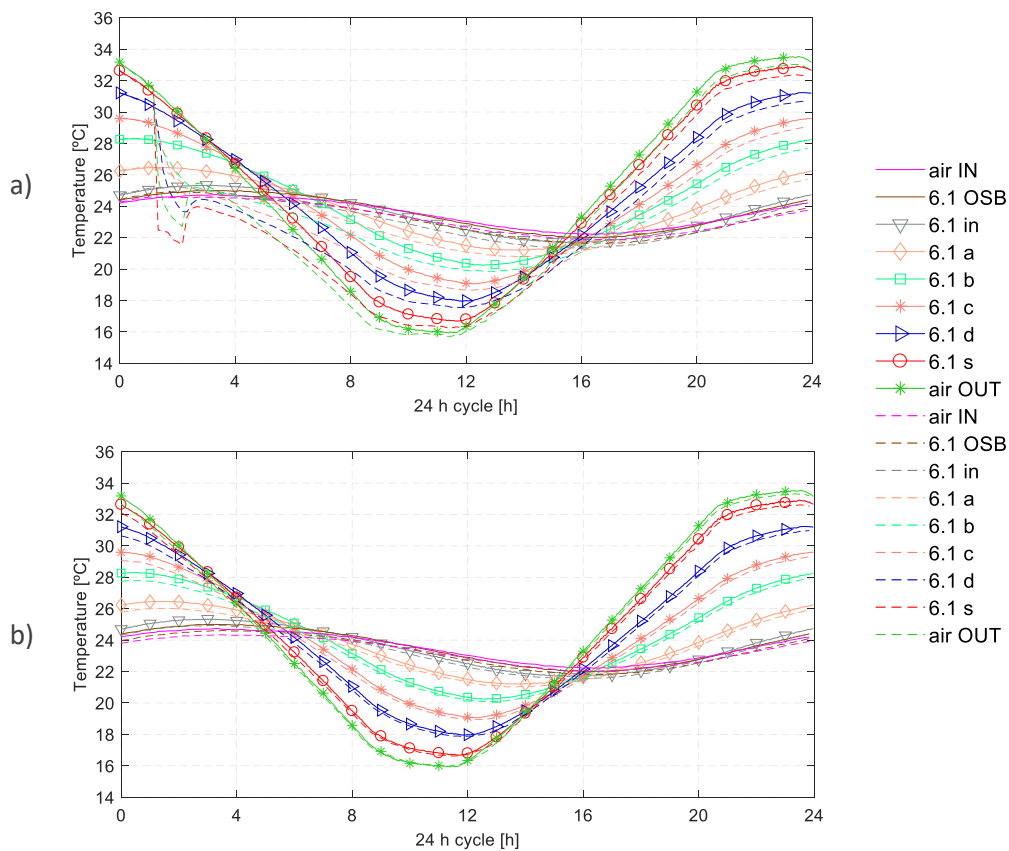


Figure 4-10: Temperatures before, during and after wetting for a 24 hours cycle: a) Before wetting ($56 \text{ h} \leq t < 80 \text{ h}$ – solid lines) and during wetting ($80 \text{ h} \leq t < 104 \text{ h}$ – dashed lines); b) Before wetting ($56 \text{ h} \leq t < 80 \text{ h}$ – solid lines) and after wetting ($104 \text{ h} \leq t < 128 \text{ h}$ – dashed lines).

To better assess the importance of the moisture in the heat transfer through the wall, Figure 4-11 presents both the experimental and the analytical temperatures and heat fluxes, before, during and after wetting (between $t = 70 \text{ h}$ to $t = 110 \text{ h}$). In this figure, W indicates the beginning of the wetting period. The period from $t = 81 \text{ h}$ to $t = 83 \text{ h}$ is zoomed to allow a better analysis of the temperature variation immediately after the water spray has been applied.

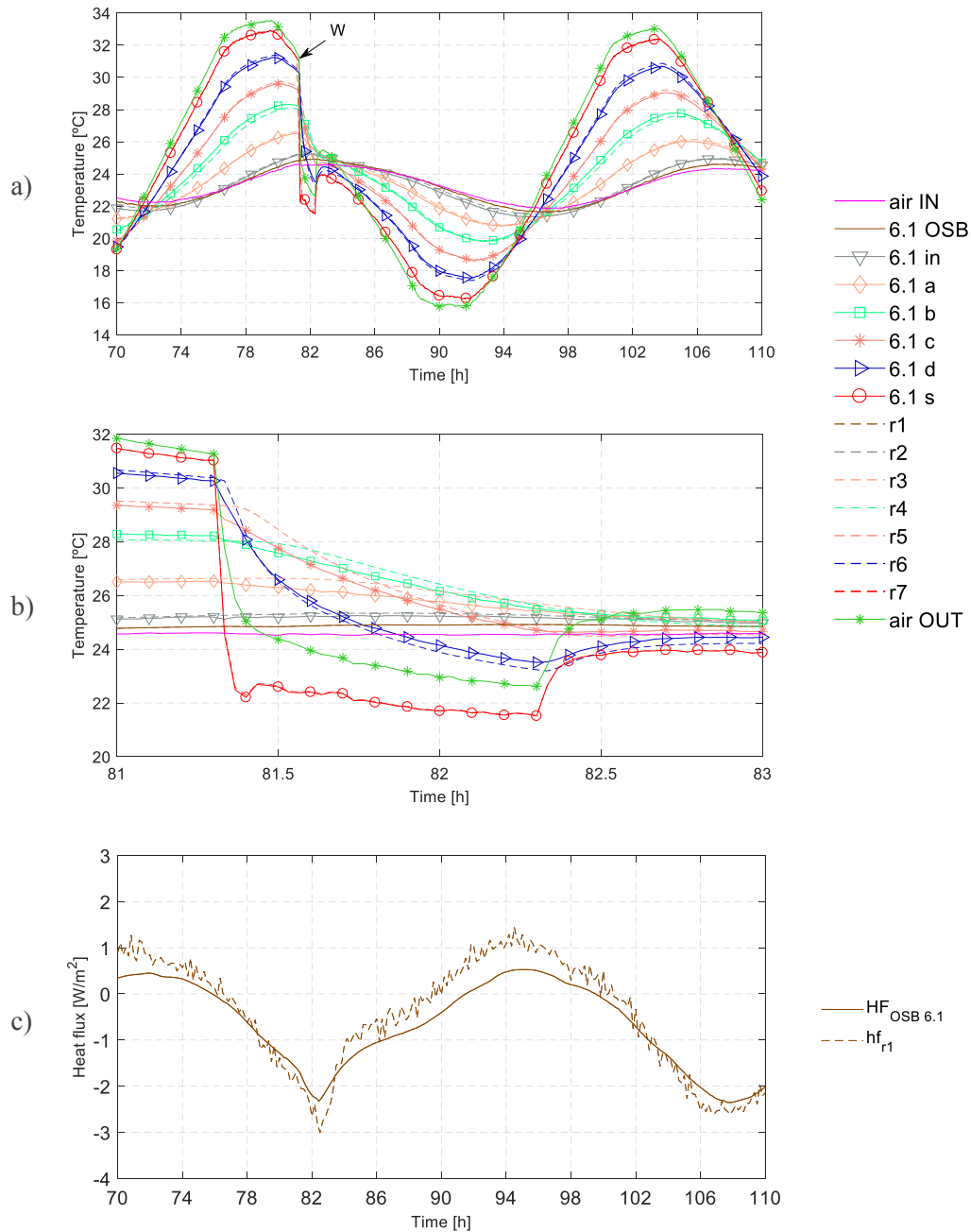


Figure 4-11: Experimental (solid lines) and analytical results (dashed lines) in summer wet conditions
a) Temperatures for 70 h < t < 110 h; b) Temperatures for 81 h < t < 83 h; c) Heat fluxes for 70 h < t < 110 h.

During the wetting phase (Figure 4-11b) there is a quick drop in temperature because of the water. At measurement point 6.1_s, the temperature decreased from 32 °C to 22.2 °C. After this initial period the temperature decreased at a slower rate, falling from 22.7 °C to the minimum value of 21.5 °C. A sudden drop in temperature is also noticeable at the thermocouples located at 10 mm (6.1_d), 25 mm (6.1_c) and 40 mm (6.1_b) from the surface. This temperature decrease is smaller as the distance to the surface increases. Analyses of the

results indicates that the water penetrated 40 mm in the first 4 min. A decrease in the temperature in the first minutes of wetting was also observed at position 6.1_a, although the rate was slower. This indicates that the water penetrated deeper (55 mm) in this test than in the steady-state test (40 mm). No decrease in temperature was observed at position 6.1_in.

Other than in the water spray period, a good agreement was found between the experimental and the analytical temperatures (see Figure 4-11a). Approximately two hours after the wetting period has finished, the analytical and experimental temperatures almost coincide, as they did before wetting. It can be concluded that the presence of water in the material does not significantly change the thermal behaviour. The main force driving the temperature variation inside the wall is the water temperature. It can thus be said that the moisture transfer across expanded cork board and the changes in the hygrothermal properties (dependent on moisture and temperature) only have an impact in the first two hours, after which point they can be considered negligible. As before, the time lag and a decrement factor were found to be only slightly affected during wetting and in the first hours of drying.

During the wetting period, the thermal behaviour is the result of the combination of two physical mechanisms, the temperature of the water and heat/moisture transfer, which depend on the expanded cork board's hygrothermal properties. The existence of a time delay in the analytical temperature variation is clearly visible at the beginning of the wetting stage. This time delay is larger for points further away from the surface being wetted.

Looking at the results shown in Figure 4-11c, it can be seen that the analytical heat flux registered at r1 is slightly higher than the experimental ones (6.1_OSB). This difference is more accentuated when the heat flow is towards the cold chamber. This behaviour is even maintained in the wetting period. It can also be seen that the heat fluxes are only slightly affected during wetting and during the first hours of drying periods. Although the analytical heat fluxes are slightly higher than the experimental ones, it can be concluded that the behaviour is similar.

4.4.2.2 Winter environment conditions

Unsteady winter conditions were imposed according to the temperature variation given in Figure 4-2b. Figure 4-12 gives the experimental registered temperatures during the first 144 h. The wetting period was started at $t = 52.8$ h (point W), for 1 h, using the same spraying set-up as before. The water temperature was $(18 \pm 0.5)^\circ\text{C}$.

As can be seen in Figure 4-12, the air temperature in the OUT chamber oscillates between -7 and $+10^{\circ}\text{C}$. Although the temperature set point was set at 20°C , the air temperature in the IN chamber exhibited a sinusoidal behaviour, with temperatures ranging between 17.5°C and 20.7°C , in response to the conditions in the OUT chamber. Right after the wall was wet, the minimum temperature of the cold chamber rose to -6°C while the maximum remained at 10°C . In the hot chamber, a slight increase in the maximum temperature was registered (from 20.7°C to 21°C), while the minimum remained equal. As observed before, the presence of the water only affected the thermal behaviour during the wetting period and up to few hours into the drying period.

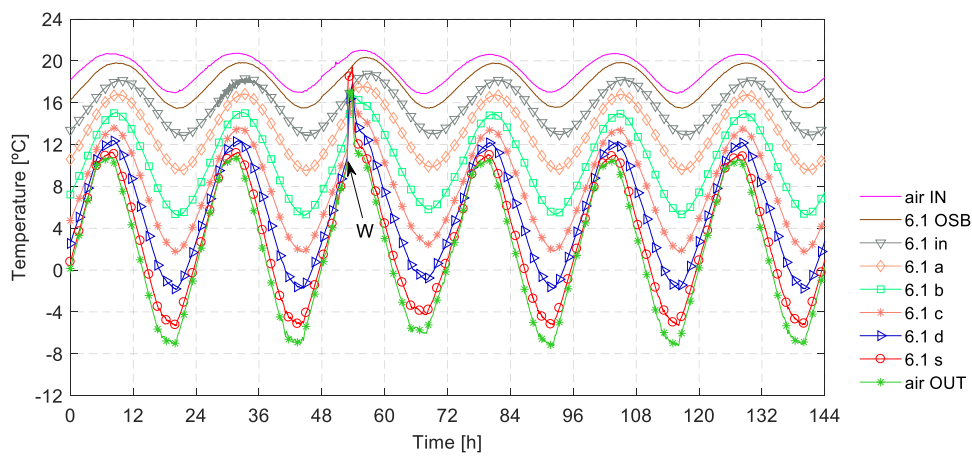


Figure 4-12: Experimental temperatures for unsteady wet winter conditions for the first 144 h.

To illustrate this behaviour, Figure 4-13a presents a 24 h cycle before wetting (cycle 1: $24\text{ h} \leq t < 48\text{ h}$) superimposed with a 24 h cycle that includes the wetting period (cycle 2: $48\text{ h} \leq t < 72\text{ h}$). Figure 4-13b, shows the same 24 h cycle before wetting with a superimposition of the second 24 h cycle after wetting (cycle 3: $72\text{ h} \leq t < 96\text{ h}$).

Analysis of the temperature rise (see Figure 4-13a) allows to verify that the water penetrates to a depth of 55 mm. Once the wetting period ends, these temperatures start to drop and rapidly reach the pre-wetting values. The same is seen in Figure 4-13b. Despite this, during the first post-wetting period cycle the temperatures at the outer surface registered some perturbations at very low temperatures, probably due to the water freezing / thawing. This perturbation was negligible at the end of cycle 3, indicating that there was no longer a significant amount of water in liquid state. Compared with the results obtained for summer conditions, the temperatures after wetting return to their initial values considerably faster.

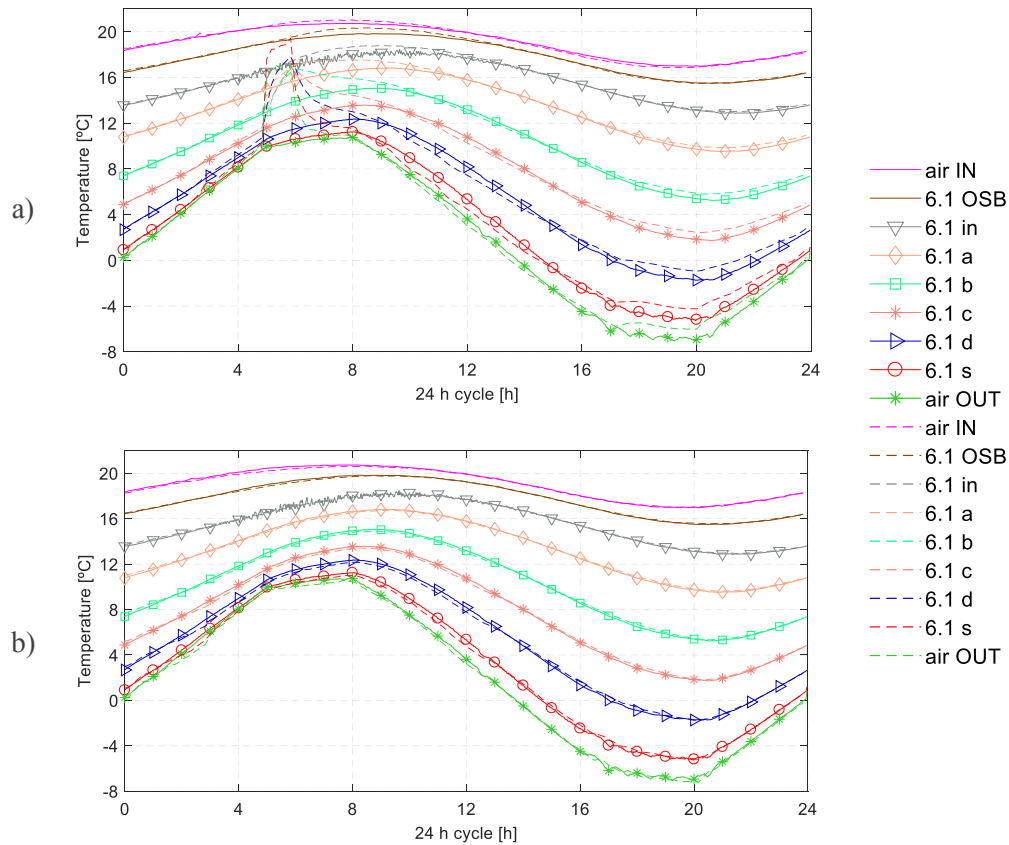


Figure 4-13: Temperature comparison between the wall before and after wetting for a 24-hour cycle, for winter conditions: a) Before wetting ($24 \text{ h} \leq t < 48 \text{ h}$ – solid lines) and during wetting ($48 \text{ h} \leq t < 72 \text{ h}$ – dashed lines); b) Before wetting ($24 \text{ h} \leq t < 48 \text{ h}$ – solid lines) and after wetting ($72 \text{ h} \leq t < 96 \text{ h}$ – dashed lines).

As before, the analytical results have been superimposed with those obtained experimentally to show the importance of the moisture transfer. Figure 4-14a shows the experimental and analytical temperatures in winter conditions before, during and after wetting, taking the surface temperatures as boundary conditions. Figure 4-14b shows the wetting period.

As with the previously presented conditions, a good agreement was found between the experimental and analytical temperatures, both before and after wetting (Figure 4-14a).

As can be seen in Figure 4-14b, the experimental and analytical temperatures along the wall during wetting have similar behaviour to those in wet steady-state conditions. However, due to the smaller temperature difference between the air and water temperature, the air and the boards' surface temperature rises at a slower rate and, once wetting has ended, this temperature falls at a higher rate than for steady-state condition. Although, as before, it was found that the water temperature is the factor with most impact on the wall temperature

variation soon after the start of the wetting period, and that the water penetrates to a depth of 40 mm in the first 4 min.

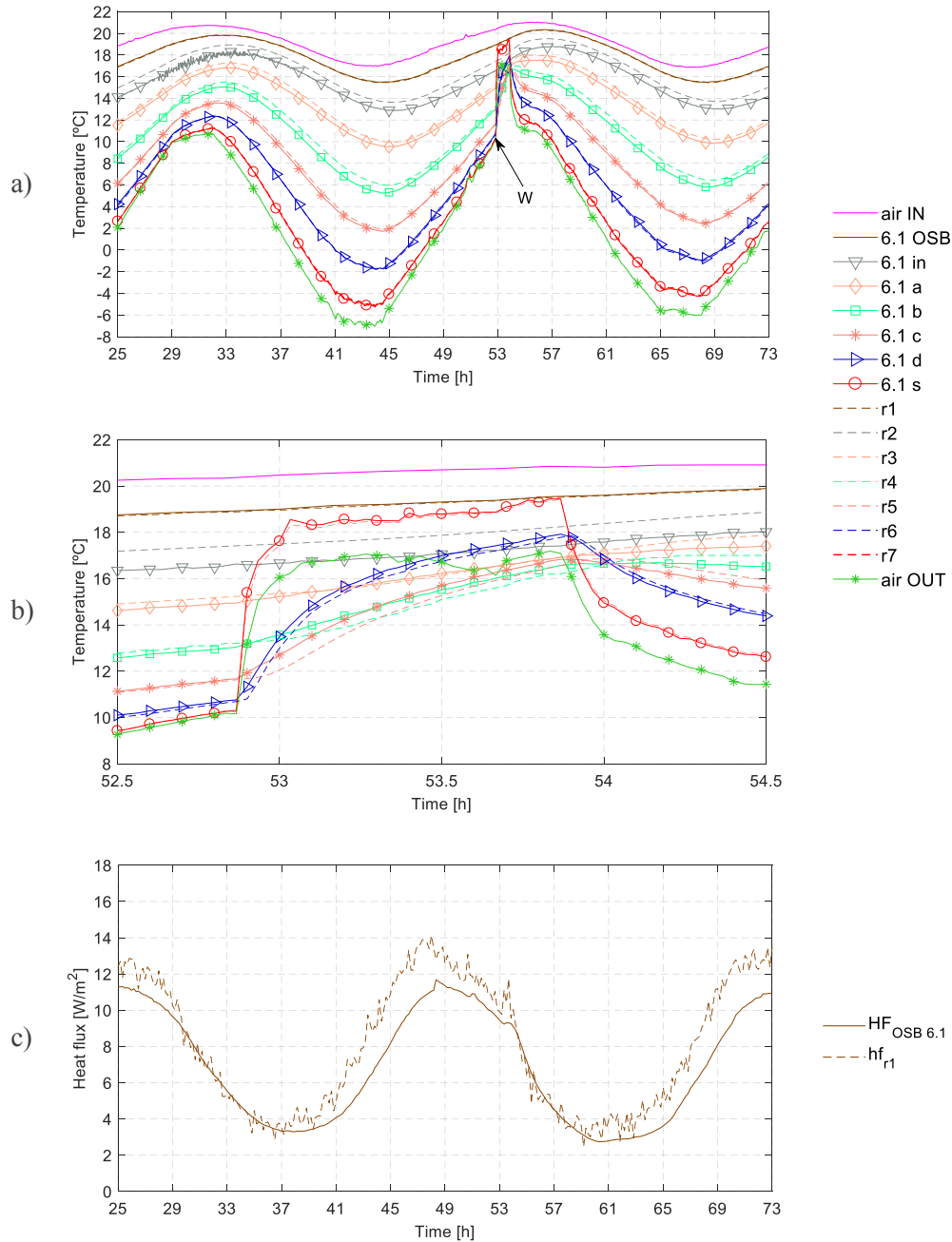


Figure 4-14: Experimental (solid lines) and analytical (dashed lines) temperatures taking the wall surface temperatures in winter conditions as boundary conditions: a) Before, during and after wetting ($25 \text{ h} \leq t \leq 73 \text{ h}$); b) During wetting ($52.5 \text{ h} \leq t \leq 54.5 \text{ h}$); c) Heat fluxes ($25 \text{ h} \leq t \leq 73 \text{ h}$).

Almost immediately after the wetting period ended, the registered temperature differences could be seen to be similar to the pre-wetting ones. The same was found for the steady-state condition. It can thus be considered that, under winter conditions, the effect of the change in

the hygrothermal properties of expanded cork boards as a function of their water content is negligible.

Regarding the heat fluxes presented in Figure 4-14c, it can be seen that although the analytical heat fluxes are slightly higher than the experimental ones, the behaviour is similar, even during the wetting period.

4.5 Final remarks

In this work, a wall covered with uncoated medium density expanded cork board was studied experimentally and numerically during exposure to rain under steady and unsteady state conditions. Winter and summer environmental conditions were simulated. For comparison purposes, all tests simulated the exposure of the wall to dry and wet weather. In order to quantify the importance of moisture in the heat transfer across the wall, the experimental results were compared with those obtained using a simple analytical model, which simulated the heat transfer phenomenon after an indirect estimation of the surface thermal resistance.

The results show that during the rainy period, water penetration in the wall is limited to the surface layers. It was noted that the depth reached by the water was similar for steady and unsteady state conditions. However, it was found that under summer conditions the rainwater reached a slightly greater depth. It was also observed that the influence of moisture was limited to the wetting period and to the first hours after wetting. However, this influence was significantly lower for winter conditions.

In all the studied cases it was found that the changes in the wall temperature and heat transfer through the wall in rainy conditions are mainly caused by the temperature of the water. Thus, the moisture transport phenomenon and the changes in the hygrothermal material properties are almost entirely limited to the first layers of the expanded cork board and to the rainy period.

Therefore, the heat transfer across a wall covered with uncoated medium density expanded cork can be simulated when only the temperature boundary conditions (external and internal air temperatures) are prescribed. It was also found that the time lag and the decrement factor provided by the expanded cork board constructive solution can also be estimated, with good agreement, by applying a simple analytical model to simulate the heat transfer phenomenon.

4.6 References

- [1] Transition to Sustainable Buildings - Strategies and opportunities to 2050, International Energy Agency (IEA), 2013. doi:10.1787/9789264202955-en.
- [2] J. Sierra-Pérez, I. López-Forniés, J. Boschmonart-Rives, X. Gabarrell, Introducing eco-ideation and creativity techniques to increase and diversify the applications of eco-materials: The case of cork in the building sector, *J. Clean. Prod.* 137 (2016) 606–616. doi:10.1016/j.jclepro.2016.07.121.
- [3] F. Pacheco-Torgal, Eco-efficient construction and building materials research under the EU Framework Programme Horizon 2020, *Constr. Build. Mater.* 51 (2014) 151–162. doi:10.1016/j.conbuildmat.2013.10.058.
- [4] M. Demertzi, J. Sierra-Pérez, J.A. Paulo, L. Arroja, A.C. Dias, Environmental performance of expanded cork slab and granules through life cycle assessment, *J. Clean. Prod.* 145 (2017) 294–302. doi:10.1016/j.jclepro.2017.01.071.
- [5] S.P. Silva, M.A. Sabino, E.M. Fernandes, V.M. Correlo, L.F. Boesel, R.L. Reis, Cork : properties , capabilities and applications, *Int. Mater. Rev.* 50 (2005) 345–365. doi:10.1179/174328005X41168.
- [6] B. Soares, L. Reis, L. Sousa, Cork composites and their role in sustainable development, *Eng. Procedia.* 10 (2011) 3214–3219. doi:10.1016/j.proeng.2011.04.531.
- [7] A. Soares, M. Júlio, I. Flores-Colen, L. Ilharco, J. de Brito, J. Gaspar Martinho, Water-Resistance of Mortars with Lightweight Aggregates, *Key Eng. Mater.* 634 (2014) 46–53. doi:10.4028/www.scientific.net/KEM.634.46.
- [8] L. Gil, Effect of hot pressing densification on the cellular structure of black agglomerated cork board, *Eur. J. Wood Wood Prod.* 52 (1994). doi:10.1007/BF02615479.
- [9] L. Gil, P. Silva, Characterization of insulation corkboard obtained from demolitions, *Ciência Tecnol. Dos Mater.* 23 (2011), <http://repositorio.lneg.pt/handle/10400.9/1387>.
- [10] L. Gil, Insulation corkboard for sustainable energy and environmental protection, *Ciência Tecnol. Dos Mater.* 25 (2013) 38–41. doi:10.1016/j.ctmat.2013.12.008.

- [11] J.D. Silvestre, N. Pargana, J. De Brito, M.D. Pinheiro, V. Durão, Insulation cork boards-environmental life cycle assessment of an organic construction material, *Materials (Basel)*. 9 (2016) 1–16. doi:10.3390/ma9050394.
- [12] J.M. Pérez-Bella, J. Domínguez-Hernández, E. Cano-Suñén, J.J. Del Coz-Díaz, F.P. Álvarez Rabanal, A correction factor to approximate the design thermal conductivity of building materials. Application to Spanish façades, *Energy Build.* 88 (2015) 153–164. doi:10.1016/j.enbuild.2014.12.005.
- [13] E. Barreira, V.P. de Freitas, External Thermal Insulation Composite Systems: Critical Parameters for Surface Hygrothermal Behaviour, *Adv. Mater. Sci. Eng.* 2014 (2014) 1–16. doi:10.1155/2014/650752.
- [14] G.B.A. Coelho, F.M.A. Henriques, Influence of driving rain on the hygrothermal behaviour of solid brick walls, *J. Build. Eng.* 7 (2016) 121–132. doi:10.1016/j.jobbe.2016.06.002.
- [15] G.R. Finken, S.P. Bjarløv, R.H. Peuhkuri, Effect of façade impregnation on feasibility of capillary active thermal internal insulation for a historic dormitory - A hygrothermal simulation study, *Constr. Build. Mater.* 113 (2016) 202–214. doi:10.1016/j.conbuildmat.2016.03.019.
- [16] J. Yu, H. Li, C.K.Y. Leung, X. Lin, J.Y.K. Lam, I.M.L. Sham, *et al.*, Matrix design for waterproof Engineered Cementitious Composites (ECCs), *Constr. Build. Mater.* 139 (2017) 438–446. doi:10.1016/j.conbuildmat.2017.02.076.
- [17] N.Z. Muhammad, A. Keyvanfar, M.Z. Muhd, A. Shafaghat, J. Mirza, Waterproof performance of concrete: A critical review on implemented approaches, *Constr. Build. Mater.* 101 (2015) 80–90. doi:10.1016/j.conbuildmat.2015.10.048.
- [18] B. Blocken, D. Derome, J. Carmeliet, Rainwater runoff from building facades: A review, *Build. Environ.* 60 (2013) 339–361. doi:10.1016/j.buildenv.2012.10.008.
- [19] R. Fino, N. Simões, A. Tadeu, Numerical and Experimental Evaluation of the Drying Behaviour of Medium Density Expanded Cork Boards Used as an External Coating, *Int. J. Sustain. Dev. Plan.* 12 (2017) 315–325. doi:10.2495/SDP-V12-N2-315-325.
- [20] V.P. De Freitas, V. Abrantes, P. Crausse, Moisture migration in building walls—Analysis of the interface phenomena, *Build. Environ.* 31 (1996) 99–108. doi:10.1016/0360-1323(95)00027-5

- [21] H.M. Künzeli, Simultaneous Heat and Moisture Transport in Building Components One - and two-dimensional calculation using simple parameters -Technical Report, 1995.
- [22] L. Škerget, A. Tadeu, BEM numerical simulation of coupled heat and moisture flow through a porous solid, *Eng. Anal. Bound. Elem.* 40 (2013) 154–161. doi:10.1016/j.enganabound.2013.12.006.
- [23] L. Škerget, A. Tadeu, J. Ravnik, BEM numerical simulation of coupled heat, air and moisture flow through a multilayered porous solid, *Eng. Anal. Bound. Elem.* 74 (2017) 24–33. doi:10.1016/j.enganabound.2016.10.004.
- [24] A. Evrard, C. Flory-celini, M. Claeys-Bruno, A. De Herde, Influence of liquid absorption coefficient on hygrothermal behaviour of an existing brick wall with Lime e Hemp plaster, *Build. Environ.* 79 (2014) 90–100. doi:10.1016/j.buildenv.2014.04.031.
- [25] M. Ibrahim, E. Wurtz, P.H. Biwolé, P. Achard, H. Sallee, Hygrothermal performance of exterior walls covered with aerogel-based insulating rendering, *Energy Build.* 84 (2014) 241–251. doi:10.1016/j.enbuild.2014.07.039.
- [26] L. Bianco, V. Serra, F. Larcher, Thermal behaviour assessment of a novel vertical greenery module system: first results of a long-term monitoring campaign in an outdoor test cell, *Energy Effic.* (2016). doi:10.1007/s12053-016-9473-4.
- [27] E. Barreira, V.P. de Freitas, Experimental study of the hygrothermal behaviour of External Thermal Insulation Composite Systems (ETICS), *Build. Environ.* 63 (2013) 31–39. doi:10.1016/j.buildenv.2013.02.001.
- [28] Y. Gao, J.J. Roux, C. Teodosiu, L.H. Zhao, Reduced linear state model of hollow blocks walls, validation using hot-box measurements, *Energy Build.* 36 (2004) 1107–1115. doi:10.1016/j.enbuild.2004.03.008.
- [29] E.A. Adam, P.J. Jones, Thermophysical properties of stabilised soil building blocks, *Build. Environ.* 30 (1995) 245–253. doi:10.1016/0360-1323(94)00041-P.
- [30] K. Ghazi Wakili, C. Tanner, U-value of a dried wall made of perforated porous clay bricks: Hot box measurement versus numerical analysis, *Energy Build.* 35 (2003) 675–680. doi:10.1016/S0378-7788(02)00209-8.
- [31] H. Kus, E. Özkan, Ö. Göcer, E. Edis, Hot box measurements of pumice aggregate

- concrete hollow block walls, *Constr. Build. Mater.* 38 (2013) 837–845. doi:10.1016/j.conbuildmat.2012.09.053.
- [32] I. Nardi, D. Paoletti, D. Ambrosini, T. De Rubeis, S. Sfarra, U-value assessment by infrared thermography: A comparison of different calculation methods in a Guarded Hot Box, *Energy Build.* 122 (2016) 211–217. doi:10.1016/j.enbuild.2016.04.017.
- [33] D. Maillet, S. André, J.C. Batsale, A. Degiovanni, C. Moyne, *Thermal Quadrupoles Solving the Heat Equation through Integral Transforms*, Wiley, 2000.
- [34] A. Joanni, E. Kausel, Heat diffusion in layered media via the thin-layer method, *Int. J. Numer. Methods Eng.* 78 (2008) 696–712. doi:10.1002/nme.2504.
- [35] ETAG 004- External Thermal Insulation Composite Systems with Rendering, European Organisation for Technical Approvals, (2011).
- [36] WUFI PC-Program for calculating the coupled heat and moisture transfer in building components.
- [37] EN 12667:2001 - Thermal performance of building materials and products — Determination of thermal resistance by means of guarded hot plate and heat flow meter methods — Products of high and medium thermal resistance, European Committee for Standardisation, (2001).
- [38] EN 1602:2013 - Thermal insulation products for building applications- Determination of the apparent density, European Committee for Standardisation, (2013).

Chapter 5

Modelling Moisture

5.1 Introduction

In recent years, the use of building materials of natural origin or/and from industrial waste has been gaining interest [1]. They allow a drastic reduction in the consumption of fossil energy and the CO₂ emissions associated with their production, when compared to conventional materials, thereby leading to a more sustainable construction [2]. One example of the use of by-products and waste from the industry is expanded cork agglomerate, a natural, renewable and fully recyclable thermal insulating material [3]. It is composed solely of cork granules, and made exclusively by the volumetric expansion and exudation of cork and its natural resins under the action of steam from water [4]. The energy used in the industrial process is mainly obtained from the combustion of cork powder, a waste generated by the cork transformation process [5]. Internationally, and in current technical documentation, expanded cork agglomerate is often referred to as ICB (insulation cork board). Compared with other insulation materials, ICB has the lowest value of carbon footprint, with a negative value of - 116.229 kg CO₂ equivalent per m³ of ICB [6].

The use of uncoated ICB as an external layer covering building facades is increasing worldwide, especially in Portugal, Spain, France, Germany, United States, Japan and Saudi Arabia. The hygrothermal performance of the building envelope depends on difference of conditions between the inside and the outside environment. When there is a water vapour pressure or temperature gradient through a wall, transport occurs from the higher to the lower potential [7]. A wall covered with uncoated medium density expanded cork can be exposed to very different climates and, in most cases, to summer and winter conditions that differ considerably. It is therefore relevant to study the hygrothermal behaviour of the wall when subjected to different levels of solar radiation, temperature and moisture gradients, which are determinant factors in reducing energy loss, managing solar gains and providing healthy conditions indoors [8,9].

Two main approaches can be followed to simulate the phenomena: experimental and numerical. Several experimental studies that evaluate the hygrothermal behaviour of buildings and building components can be found in the literature. Antonyová et al. [10] studied the hygrothermal properties of building envelopes to develop a non-destructive method for measuring the temperature and moisture in the space between the insulation panel and the outer wall of buildings, so that the effectiveness of energy saving can be evaluated. Rahim et al. [11] used an experimental laboratory facility to investigate the hygrothermal behaviour

of a straw concrete wall under static and dynamic conditions of temperature and relative humidity. Odgaard et al. [12] monitored the relative humidity and temperature of two solid masonry spandrels over a period of 2 years and 8 months, to study the effect of installing interior insulation on the spandrels in a historic building with solid masonry walls in Copenhagen. Labat et al. [13] studied the dynamic coupling between vapour and heat transfer under real climate conditions, testing a 20 m² wood-frame house in Grenoble, France that was fitted with six different wall assemblies, over a period of more than 3 years.

Experimental work is time consuming and can be very expensive. Numerical modelling may be more useful than laboratory testing or in-situ measurements since it is cheaper to implement [14]. Different numerical models have been developed over a number of years to simulate the combined transport of heat and moisture, starting in the area of soil sciences, with the studies by Philip and De Vries [15] and Luikov [16]. Their work was then extrapolated to the field of building physics, in which, depending on the chosen potential, the final set of equations varies from one author to another [17]. Krejčí et al. [18] performed numerical analyses of coupled heat and moisture transfer in masonry structures by using two computational methods that are based on the diffusion model proposed by Künzels and Kiessl [19]. For both methods, the results of the 2D numerical simulation of coupled heat and moisture transfer in a brick wall showed good agreement with those obtained with the original finite element method, but with a clear reduction of computational time. Abahri et al. [20] developed an analytical model for the coupled heat and mass transfer in porous building materials. To validate the proposed analytical solutions the results were compared with those of several numerical simulations that used a finite element method. Good agreement was found. Škerget and Tadeu [21] developed a numerical model based on the boundary element method (BEM) to simulate the coupled heat and moisture flow through a porous solid. To validate the model, the authors used two benchmark examples, one of which was a relatively simple transient linear vapour diffusion while the other was a highly nonlinear coupled moisture and heat transport, and good agreement was found for both. Although in the second case, since the difference between the heat and mass diffusion coefficient has several orders of magnitude, better stability and accuracy was obtained by using the linear variation of the functions throughout the time step model than with the constant variation in terms. Min et al. [22] developed a method, based on Lukiov's model to simulate the coupled heat and moisture transport in concrete. The numerical results were compared with the experimental ones and a good agreement was obtained. Škerget et al. [23] include the airflow in their coupled heat and moisture model, thereby enabling the simulation of air, moisture and heat flows.

Heat and moisture transfer models are useful when the intention is to evaluate the risk of condensation on building components and any related moisture problems. However, an external building component is also exposed to solar radiation, which increases its temperature. Failure to consider the solar heat flux could underestimate the materials' temperature and thus the heat and mass transport phenomena.

Holm and Künzle [24] used WUFI [25], a computer program which calculates the transient heat and moisture transport in building components, to predict, under natural climatic conditions, the moisture and temperature strains that act on an ETICS with mineral wool insulation. Coons et al. [26] used ANSYS CFX 16.1 software to model solar energy as one of the heat sources that affect the external and internal temperatures in residential buildings. The intention was to evaluate the benefits of using a selective solar-beam absorbing paint. The study was undertaken for three cities that represent extreme climates in the United States, under summer and winter conditions. The authors concluded that the positive outcome obtained for the summer season, with a reduction of the cooling loads, has to be balanced against the negative impact in the winter season once the heating loads increase. Kant et al. [27] evaluate the thermal behaviour of building bricks containing phase change materials (PCMs), when subjected to solar radiation and ambient temperature. A finite element analysis method was used in a two-dimensional numerical study of heat and mass transfer through the bricks containing PCMs. The simulations, performed using the meteorological data of Rae Bareilly for the period 14–16 March 2014, indicate that building bricks with PCMs, when exposed to direct solar radiation, are suitable to be used as passive thermal conditioners in buildings since they stabilise the room temperature and so reduce energy consumption. Cho et al. [28] used a finite elements method to experimentally and numerically study the heat and moisture transfer in concrete under real weather data. The model was validated with experimental results. The authors noticed that because of the effects of solar radiation and radiation cooling effect the temperature inside the concrete is 6 °C higher in summer and 2 °C lower in winter. Škerget et al. [29] conducted a study on the transient heat and moisture transfer of a multilayer porous solid building components exposed to solar heat flux and submitted to convective heat and mass exchange with the surrounding environment. The BEM numerical model that was used proved to be suitable for the numerical simulation of transient transport phenomena in cases of building envelopes exposed to real weather data.

The main purpose of this study was to evaluate the hygrothermal behaviour, in terms of temperature, relative humidity and moisture content variation, of walls made of OSB and

concrete and covered with uncoated medium density expanded cork board, when exposed to real weather data. For this purpose, a numerical model that could simulate the coupled heat and moisture transfer in a building component under solar radiation was used. However, the quality of the numerical results depends on appropriate input data [30,31], and these are not always available, even in the simulation tool databases which often provide only generic data. Thus, a reliable set of hygrothermal properties as a function the material moisture content must be known before a reasonable assessment of the building's energy-related envelope can be made with sufficient accuracy [32,33]. To ensure the accuracy of the numerical results, the properties of medium density ICB were evaluated experimentally and validated by comparing the numerical results with the transient heat and moisture flow through a wall inserted between two chambers of a calibrated hot-box. The properties of all other materials were defined using data from WUFI database.

This paper first presents the numerical model that was used to simulate the hygrothermal behaviour of the constructive solutions. The medium density ICB hygrothermal properties were then evaluated and the experimental validation performed. The importance of moisture and heat flow through an OSB wall covered with uncoated medium density ICB was assessed. Finally, the numerical results obtained for Bragança (Portugal) and Seville (Spain) for summer and winter conditions are presented and discussed.

5.2 Governing transport equations for a two-phase system

The moisture transport phenomena, in a porous solid, of a thermodynamic system comprising the liquid and vapour phases are governed by a series of partial differential equations. If Ω is the domain of the porous solid, bounded by a surface Γ , these equations, or the moisture diffusion transport equation, can be formulated as shown below [23,34],

$$\theta \frac{\partial \varphi}{\partial t} = \vec{\nabla} \cdot (D_\varphi \vec{\nabla} \varphi + D_T \vec{\nabla} T - D_l \rho_l \vec{g}) \quad (5-1)$$

where $\theta = dW/d\varphi$ is the slope of the sorption isotherm $W = W(\varphi)$, and W [kg/m³], T [K], ρ_l [kg/m³] and \vec{g} [m/s²] are quantities representing the mass moisture content, temperature, liquid water mass density and the gravity acceleration. The primitive variable in eqn. (5-1) is the relative humidity field function $\varphi(r_j, t)$. D_φ [kg/(m s)] and D_T [kg/(m s K)] are transport coefficients, given as [23,34]:

$$D_\varphi = \delta_p p_s + D_l R_w \rho_l \frac{T}{\varphi} \quad \text{and} \quad D_T = \delta_p \frac{dp_s}{dT} \varphi + D_l R_w \rho_l \ln(\varphi) \quad (5-2)$$

in which δ_p [s] is the vapour permeability and D_l [s] is the liquid permeability of a solid material, these transport properties being defined by the constitutive models below for vapour diffusion \vec{j}_v [kg/(m² s)] and liquid conduction \vec{j}_l [kg/(m² s)] mass flows:

$$\vec{j}_v = -\delta_p \vec{\nabla} p_v \quad \text{and} \quad \vec{j}_l = -D_l \vec{\nabla} p_l + D_l \delta_l \vec{g} = D_l \vec{\nabla} p_{\text{suc}} + D_l \delta_l \vec{g} \quad (5-3)$$

in which p_v [Pa], p_l [Pa] and $p_{\text{suc}} = p_a - p_l$ [Pa] are driving potentials for vapour pressure, pore liquid pressure and suction pressure, respectively, when p_a [Pa] is the atmospheric pressure and R_w [J/(kg K)] and p_s [Pa] are, respectively, the gas constant of the water vapour and the vapour saturation pressure. The coupling of eqn. (5-1) to the heat energy transport equation is explicit in terms of temperature gradients and implicit in terms of nonlinear transport properties.

The heat energy balance equation accounts for the accumulation within the solid matrix, sensible and latent heat energy fluxes in and out of the control volume, as follows:

$$\rho_m c_{p,eff} \frac{\partial T}{\partial t} = -\vec{\nabla}(\vec{q}_{\text{sens}} + \vec{q}_{\text{lat}}) \quad (5-4)$$

where the specific capacities per mass $c_{p,eff} = c_{pm} + c_{pl} W / \rho_m$ [J/(kg K)], c_{pm} [J/(kg K)] and c_{pl} [J/(kg K)] refer to the effective dry porous material and to liquid water, ρ_m [kg/m³] denotes solid matrix mass density, whilst the sensible \vec{q}_{sens} [W/m²] and the latent \vec{q}_{lat} [W/m²] heat energy fluxes are,

$$\vec{q}_{\text{sens}} = -\lambda_{eff} \vec{\nabla} T \quad \text{and} \quad \vec{q}_{\text{lat}} = h_{\text{lat}} \vec{j}_v = [h_e + (c_{pv} - c_{pl}) T] \vec{j}_v \quad (5-5)$$

in which specific latent enthalpy is represented by h_{lat} [kJ/kg], specific latent enthalpy of evaporation or condensation by h_e [kJ/kg] and c_{pv} [J/(kg K)] is the specific heat per mass of water vapour; $\lambda_{eff} = \lambda_m + (\lambda_{mst} W) / \rho_l$ [W/(m K)] and λ_m [W/(m K)] are thermal conductivities relating, respectively, to the effective and dry porous material (λ_{mst} defines the influence of the moisture) If the heat flux eqn. (5-5) is substituted into conservation eqn. (5-4) we get:

$$c_{eff} \frac{\partial T}{\partial t} = \vec{\nabla} [\lambda_{eff} \vec{\nabla} T - h_{lat} \vec{J}_v] \quad (5-6)$$

where the coefficient $c_{eff} = \rho_m c_{p,eff}$ [J/(m³ K)] is the effective specific heat per unit volume.

5.2.1 Initial and boundary conditions

The distribution of field functions in the solution domain and their normal derivatives on the boundary comprise the initial and boundary conditions. They are given by,

$$\begin{aligned} \varphi = \bar{\varphi} \text{ and } T = \bar{T} \text{ in } \Omega \text{ at } t = t_0 \\ \frac{\partial \varphi}{\partial n} = \frac{\partial \bar{\varphi}}{\partial n} \text{ and } \frac{\partial T}{\partial n} = \frac{\partial \bar{T}}{\partial n} \text{ on } \Gamma \text{ for } t = t_0 \end{aligned} \quad (5-7)$$

The Dirichlet or first-type boundary conditions are derived from the known surface value of the driving potentials:

$$T = \bar{T} \text{ and } \varphi = \bar{\varphi} \text{ on } \Gamma_1 \text{ for } t > t_0 \quad (5-8)$$

The heat or mass flow at the surface must be known for the Neumann or second-type boundary conditions, which are given by the surface temperature prescribed for the surface and relative humidity normal derivative values, thus:

$$\frac{\partial T}{\partial n} = \frac{\partial \bar{T}}{\partial n} \text{ and } \frac{\partial \varphi}{\partial n} = \frac{\partial \bar{\varphi}}{\partial n} \text{ on } \Gamma_2 \text{ for } t > t_0 \quad (5-9)$$

Third-type (Cauchy) boundary conditions are the most common kind of moisture and heat flux transfer across the boundary, from the domain surface Γ_3 to the ambient. The following expressions for the relative humidity and temperature normal derivatives are expressed as follows:

$$\frac{\partial \varphi}{\partial n} = - \left(\frac{\beta_p}{\delta_p} + \frac{1}{p_s} \frac{dp_s}{dT} \frac{\partial T}{\partial n} \right) \varphi + \frac{\beta_p p_{v,a}}{\delta_p p_s} \quad (5-10)$$

$$\frac{\partial T}{\partial n} = \frac{1}{\lambda_{eff}} [\alpha(T_a - T) + q_{sol} + (h_{lat} - h_{lat,a})j_v] \quad (5-11)$$

in which the vapour transfer coefficient is β_p [s/m], the heat transfer coefficient is α [W/(m² K)] and q_{sol} [W/m²] and p_v [Pa] are the solar heat flux and vapour pressure. The index "a" signifies the ambient.

5.3 Integral representations for energy and moisture transport equations

The transport differential energy model, which is written for the primitive field function temperature, and the moisture conservation model, written for the relative humidity, can be rewritten as a general nonhomogeneous parabolic diffusion equation, based on the BEM [23,35,36],

$$L[u] + \frac{\partial b_j}{\partial x_j} + b = a_0 \frac{\partial^2 u}{\partial x_j \partial x_j} - \frac{\partial u}{\partial t} + \frac{\partial b_j}{\partial x_j} + b = 0 \quad (5-12)$$

in which $u(r_j, t)$ is an arbitrary continuous field function, $L[\cdot]$ is the diffusion linear differential operator, and the terms $b_j(r_j, t)$ and $b(r_j, t)$ stand for nonhomogeneous or source effects arising from the nonlinear transport coefficients and the production of the conservative field function, respectively. The corresponding integral representation written for a time step $\Delta t = t_F - t_{F-1}$ can be expressed as:

$$\begin{aligned} c(\xi)u(\xi, t_F) + a_0 \int_{\Gamma} \int_{t_{F-1}}^{t_F} u q^* dt d\Gamma &= a_0 \int_{\Gamma} \int_{t_{F-1}}^{t_F} q_j n_j u^* dt d\Gamma \\ &+ \int_{\Omega} \int_{t_{F-1}}^{t_F} \left(\frac{\partial b_j}{\partial x_j} + b \right) u^* dt d\Omega + \int_{\Omega} u_{i,F-1} u_{F-1}^* d\Omega \end{aligned} \quad (5-13)$$

The application of the Gaussian divergence theorem gives the following integral representation:

$$\begin{aligned}
c(\xi)u(\xi, t_F) + a_0 \int_{\Gamma} \int_{t_{F-1}}^{t_F} u q^* dt d\Gamma = \int_{\Gamma} \int_{t_{F-1}}^{t_F} (a_0 q_j + b_j) n_j u^* dt d\Gamma \\
- \int_{\Omega} \int_{t_{F-1}}^{t_F} b_j q_j^* dt d\Omega + \int_{\Omega} \int_{t_{F-1}}^{t_F} b u^* dt d\Omega + \int_{\Omega} u_{i,F-1} u_{F-1}^* d\Omega
\end{aligned} \tag{5-14}$$

in which the field function normal flux is represented by $q = q_j n_j$ and $u^*(\xi, s, t_F, t)$ is the parabolic diffusion fundamental solution [37], given by:

$$u^*(\xi, s, t_F, t) = \frac{1}{(4\pi a_0 \tau)^{d/2}} \exp \left[-\frac{r^2}{4a_0 \tau} \right] \tag{5-15}$$

in which, in the solution domain, the field point is represented by (s, t) while (ξ, t_F) is the source point; d is the dimensionality of the problem, r is the distance from the field to the source point and $\tau = t_F - t$.

The nonhomogeneous terms b_j and b in eqn. (5-12) are given by the following relations, i.e. for energy transport,

$$b_j = \frac{1}{c_0} \left(\tilde{\lambda} \frac{\partial T}{\partial x_j} - h_{lat} j_{vj} \right) \quad \text{and} \quad b = -\frac{\tilde{c}}{c_0} \frac{\partial T}{\partial t} \tag{5-16}$$

with $c_{eff} = c_0 + \tilde{c}$, $\lambda_{eff} = \lambda_0 + \tilde{\lambda}$ and $a_0 = \lambda_0/c_0$, and for the moisture transport:

$$b_j = \frac{1}{\theta_0} \left(\widetilde{D}_\varphi \frac{\partial \varphi}{\partial x_j} + D_T \frac{\partial T}{\partial x_j} - D_1 \rho_1 g_j \right) \quad \text{and} \quad b = -\frac{\tilde{\theta}}{\theta_0} \frac{\partial \varphi}{\partial t} \tag{5-17}$$

with $\theta = \theta_0 + \tilde{\theta}$, $D_\varphi = D_{\varphi 0} + \widetilde{D}_\varphi$ and $a_0 = D_{\varphi 0}/\theta_0$. Eqn.(5-14) is solved numerically by discretizing the boundary, Γ , into a number of boundary elements, while the domain, Ω , is discretized into a number of internal cells. It is assumed, moreover, that field functions and their derivatives vary within each element/cell and each time step, depending on the space, $\{\Phi\}$ or $\{\emptyset\}$ and time $\{\Psi\}$ interpolation functions, such that,

$$\begin{aligned}
u(S, t) &= \{\Phi\}^T \{\Psi\} \{u\}_m^n, & q(S, t) &= \{\Phi\}^T \{\Psi\} \{q\}_m^n \\
b_j(S, t) &= \{\Phi\}^T \{\Psi\} \{b_j\}_m^n, & b_j(s, t) &= \{\emptyset\}^T \{\Psi\} \{b_j\}_m^n \quad \text{etc.}
\end{aligned}
\tag{5-18}$$

in which the index n is the number of nodes in the element or cell, and m is the degree of variation of the function, $\{\Psi\}$. In the case of mixed boundary elements, discretization could take the form of approximating the continuous quadratic field function over the boundary element and the internal cell. Its derivative is then approximated in the normal direction to the boundary element [23].

5.4 Material properties

ICB is being applied as an insulation coating in a number of buildings, not only in Portugal and Spain, the main producers of cork, but, as mentioned above, to some extent around the world. In Portugal and Spain, the most usual support wall is a concrete wall. However, in the north of Europe and the United States, timber construction is frequently used. Thus, two types of constructive solutions were considered in this study. One in which the base wall consists of OSB panels and another in which the base wall is made of concrete.

So that numerical simulations can be performed, a set of reliable material properties of the ICB, OSB, concrete and bonding mortar are needed, namely the liquid water conductivity/diffusivity, vapour diffusivity and the thermal conductivity of the solid matrix. These properties depend on other properties which have to be determined experimentally, such as the sorption isotherm, porosity, free saturation water content, water absorption coefficient and variation of the thermal conductivity with moisture content. For the medium density expanded cork, these hygrothermal properties were evaluated in this work (see Chapter 3), following the relevant normative procedures. OSB, mortar and the concrete hygrothermal properties were taken from the WUFI materials database. The method used to calculate the required properties and subsequent results are presented in the paragraphs that follow.

The capillary liquid transport is the predominant moisture transport mechanism in capillary porous materials, such that it is basically a convective phenomenon. In the context of building physics, however, it is sufficiently accurate to regard the liquid transport in the pore spaces as a diffusion phenomenon [38] given by the following constitutive model for the liquid flux j_l :

$$j_l = -D_w(W)\vec{\nabla}W \quad (5-19)$$

where $D_w(W)$ [m²/s] is the liquid transport coefficient, which is generally strongly dependent on the moisture content W [kg/m³].

If a material's water content has a linear increase over the square root of time, the liquid transport can be described by the diffusion formula. There are two liquid transport coefficients: D_{ws} [m²/s] is the liquid transport coefficient for suction and D_{ww} [m²/s] the liquid transport for redistribution. The water absorption coefficient, A_w [kg/(m² s^{0.5})], is the standard parameter used to describe the capillary suction of a material. The increase of D_{ws} as moisture content increases can be estimated using eqn. (5-20) [38,39].

$$D_{ws}(\varphi) = 3.8 \left(\frac{A_w}{W_{sat}} \right)^2 1000^{W/W_{sat} - 1} \quad (5-20)$$

The coefficient D_{ww} is neglected in the present work because of its small values.

Considering constitutive eqs. (5-3) and (5-19) for the liquid flux j_l the following equality can be formulated:

$$j_l = D_l \vec{\nabla} p_{suc} = -D_w(W) \vec{\nabla} W = -D_w \frac{\partial W(\varphi)}{\partial p_{suc}} \vec{\nabla} p_{suc} \quad (5-21)$$

yielding the following relation for the transport coefficients

$$D_l(\varphi) = -D_w(W) \frac{\partial W(\varphi)}{\partial p_{suc}} \quad (5-22)$$

The sorption isotherm $W(\varphi)$ is given by:

$$W(\varphi) = W_{sat} \frac{k_1}{[1 + (a_1 h)^{n_1}]^{m_1}} \text{ and } h = \frac{p_{suc}}{\rho_l g} = -\frac{R_w T \ln(\varphi)}{g} \quad (5-23)$$

with the exponent $m_1 = 1 - 1/n_1$. Manipulating eqn. (5-23) the following derivative can be obtained:

$$\frac{\partial W(\varphi)}{\partial p_{\text{suc}}} = - \frac{k_1 (a_1 h)^{n_1} [1 + (a_1 h)^{n_1}]^{-m_1 - 1}}{\rho_l g h} \quad (5-24)$$

resulting in the following equality for the transport coefficient:

$$D_l(\varphi) = - 3.8 \left(\frac{A_w}{W_{\text{sat}}} \right)^2 1000^{W/W_{\text{sat}} - 1} \cdot \frac{-k_1 (a_1 h)^{n_1} [1 + (a_1 h)^{n_1}]^{-m_1 - 1}}{\rho_l g h} \quad (5-25)$$

The vapour permeability δ_p [s] is given by:

$$\delta_p(W, T) = \frac{D_{\text{va}}}{\mu R_w T} \frac{1 - \frac{W}{W_{\text{sat}}}}{(1 - p) \left(1 - \frac{W}{W_{\text{sat}}} \right)^2 + p} \quad (5-26)$$

where μ [–] is diffusion resistance factor, $D_{\text{va}} = 26.1 \cdot 10^{-6} \text{ m}^2/\text{s}$ is the vapour diffusivity in air and p [m^3/m^3] is the porosity.

Next, the ICB experimental data, measured in Chapter 3, and data from WUFI database for mortar, concrete and OSB were used to compute the coefficients k_1, a_1 and n_1 , summarized in Table 5-1, based on the best fit of the experimental data, Figure 5-1.

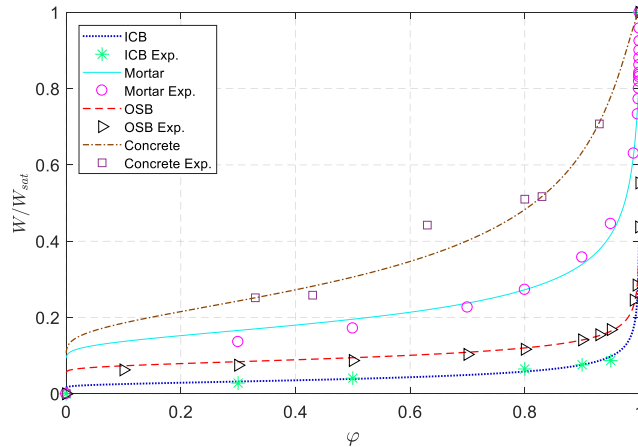


Figure 5-1: Sorption isotherm at $T= 296.15$ K. The markers represent experimental data.

The liquid water conductivity/diffusivity and the water vapour permeability were then computed as a function of the relative humidity, using the material properties listed in Table 5-1, see Figure 5-2.

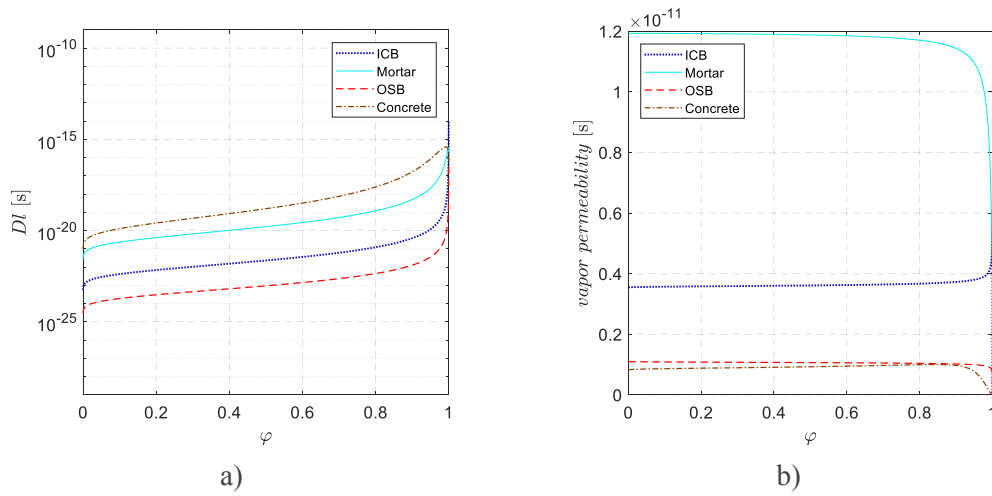


Figure 5-2: Hygrothermal behaviour ($T = 296.15$ K): a) Liquid water conductivity/diffusivity; b) Water vapour permeability.

Table 5-1: Materials' properties: ICB - measured in Chapter 3; OSB, mortar and concrete - WUFI materials database.

Parameter	ICB	OSB	Mortar	Concrete
Water retention				
$W_{\text{sat}} [\text{kg}/\text{m}^3]$	80.64	814.00	163.15	147.00
$k_1 [-]$	1.0000	1.0000	0.8325	1.0000
$a_1 [1/\text{m}]$	0.9884	7.0600	$1.40 \cdot 10^{-2}$	$1.70 \cdot 10^{-3}$
$n_1 [-]$	1.35400	1.21190	1.29525	1.42120
Vapour/liquid diffusion				
$\mu [-]$	54.61	165.00	16.12	248.00
$p [\text{m}^3/\text{m}^3]$	0.09	0.90	0.44	0.18
$A_w [\text{kg}/(\text{m}^2 \text{ s}^{0.5})]$	0.001433	0.002000	0.007000	0.009000
Thermal conduction				
$\lambda_m [\text{W}/(\text{m K})]$	0.041	0.130	0.80	1.60
$\lambda_{\text{mst}} [\text{W}/(\text{m K})]$	0.274	0.328	2.696	2.638
Heat capacity				
$\rho_m [\text{kg}/\text{m}^3]$	156.0	595.0	1350.0	2220.0
$c_{\text{pm}} [\text{J}/(\text{kg K})]$	1530.0	1500.0	850.0	850.0

5.5 Validation of the material properties

The obtained material properties were validated by running the laboratory and numerical experiment.

For the purpose of the laboratory evaluation of the material properties, the dynamic heat and moisture flow through a wall was conducted using a calibrated hot-box.

The hot-box apparatus is composed of three parts: (1) an OUT chamber that simulates the external environment, in which a periodic 24 h sinusoidal temperature variation, between +15.0 °C and +35.0 °C was imposed; (2) an IN chamber that simulates the internal conditions, in which the temperature is a response to the temperature imposed in the OUT chamber; (3) a frame that holds the constructive solution presented in Figure 5-3, a (2.2×2.4) m² 0.018 m OSB panel (supported by a wood frame) coated with 0.070 m medium density expanded cork boards that are bonded to it with a 0.005 m thick bonding mortar.

A ventilation system was used to prevent air stratification. The hot-box was installed in a room with temperature of (20±2) °C throughout the test, so that the effect of the heat loss variation through the IN chamber envelope could be minimized. Thermocouples were installed to monitor the temperature at several measurement points as indicated in Figure 5-3.

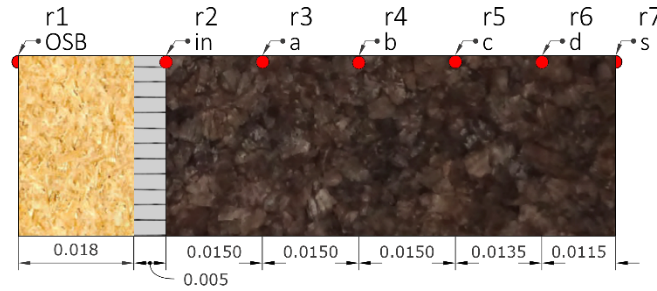


Figure 5-3: Position and identification of the thermocouples and corresponding numerical receivers in the cross section of the test specimen (dimensions in m).

The heat and moisture transfer through the three-layer porous wall, a schematic of which is given in Figure 5-4 was numerically simulated using the BEM formulation presented above, under the same dynamic conditions as in the experimental simulations. A uniform dense mesh of $M = 200 \times 1$ macro-elements was applied. The convergence criterion selected was $\epsilon = 10^{-7}$ and the under-relaxation parameters were set to $ur = 0.01 - 0.0001$ for the driving potentials, whilst the value $ur = 0.0001$ was selected for the nonlinear transport properties.

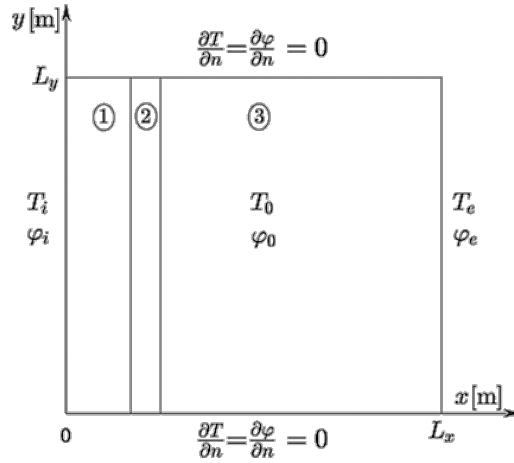


Figure 5-4: Three-layer OSB (1)/mortar (2)/ICB (3) porous wall: initial and boundary conditions;
 $L_x = 0.093\text{m}$, $L_y = 0.006\text{m}$; $d_{\text{OSB}} = 0.018\text{m}$, $d_{\text{mortar}} = 0.005\text{m}$, $d_{\text{ICB}} = 0.070\text{m}$.

For comparison purposes the numerical simulation was performed without solar radiation. The internal and external environments were imposed as boundary conditions. The time dependent analysis was performed by running the simulation from the initial state with a time step values $\Delta t = 120\text{ s}$. The simulation time was 132 hours. The initial hygrothermal conditions for the transient numerical simulation were determined by the steady state numerical computation of coupled heat and moisture flow through a multilayered porous structure. The following Dirichlet boundary conditions were prescribed at the left internal boundary at $x = 0\text{ m}$ and $0 \leq y \leq L_y$:

$$T_i = 21.45\text{ °C} \quad \text{and} \quad \varphi_{a,i} = 0.5373 \quad \text{at} \quad t = 0 \quad (5-27)$$

on the right external boundary at $x = L_x$ and $0 \leq y \leq L_y$,

$$T_e = 21.49\text{ °C} \quad \text{and} \quad \varphi_{a,e} = 0.6546 \quad \text{at} \quad t = 0 \quad (5-28)$$

and zero Neumann boundary conditions were prescribed elsewhere:

$$\frac{\partial \varphi}{\partial n} = 0 \quad \text{and} \quad \frac{\partial T}{\partial n} = 0 \quad \text{for} \quad t = 0 \quad (5-29)$$

These numerical simulation results were compared with the experimental data. The numerical receivers (r1 to r7) were placed at the same depths as the thermocouples. The experimental

and the numerical results are presented in Figure 5-5, and a quite good agreement can be seen. The greatest difference was found for the receiver r4 (b), with a maximum value of 0.4 °C.

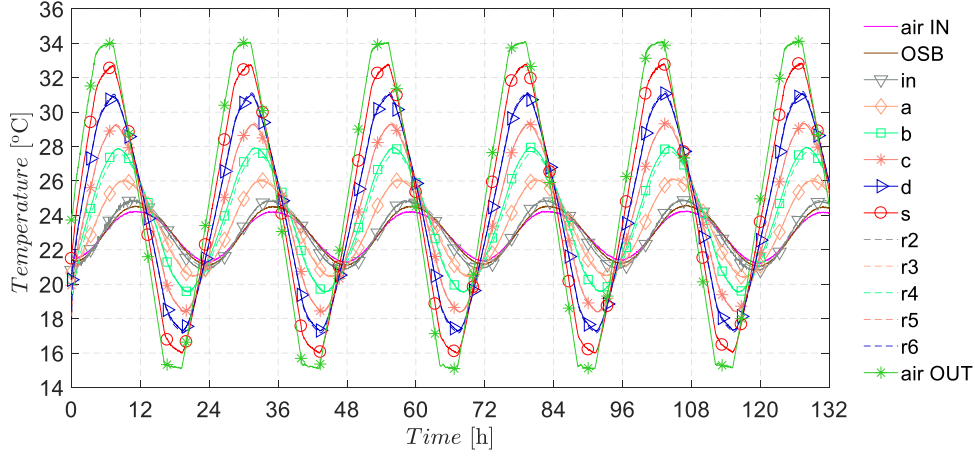


Figure 5-5: Experimental versus numerical results.

5.6 Importance of the moisture and heat flow through walls coated with expanded cork

Initially, the wall solution described above was subjected to steady state conditions ($T = 20$ °C and $\phi = 0.5$). At time $t = 0$ h the surface conditions changed abruptly.

Two cases were studied: Case 1 assumed that only the outer surface changes to $T = 30$ °C and $\phi = 1$, while in Case 2 the inner and outer surface are both subjected to $T = 30$ °C and $\phi = 1$.

Non-uniform symmetric dense mesh of $M = 100 \times 1$ macro-elements was applied, with aspect ratio $R_x = 4$ between the largest and the smallest boundary element. The convergence criterion selected was $\epsilon = 10^{-7}$, and the under-relaxation parameters were set to $ur_T = 0.1$ and $ur_\phi = 0.001$ for the driving potentials.

Figure 5-6 illustrates how the driving potentials such as relative humidity $\phi(t)$, water content $W(t)$, and temperature $T(t)$ throughout the wall cross section change with time ($t = 1, 5, 10, 20, 40, 100$ and 200 days).

On the basis of the figure, it can be concluded that the transport of heat against the transport of moisture in porous media is a considerably more intense transport phenomenon by a ratio of several orders of magnitude. Relative humidity profiles with time are sharp compared to temperature profiles, making the numerical simulation of moisture transport very demanding.

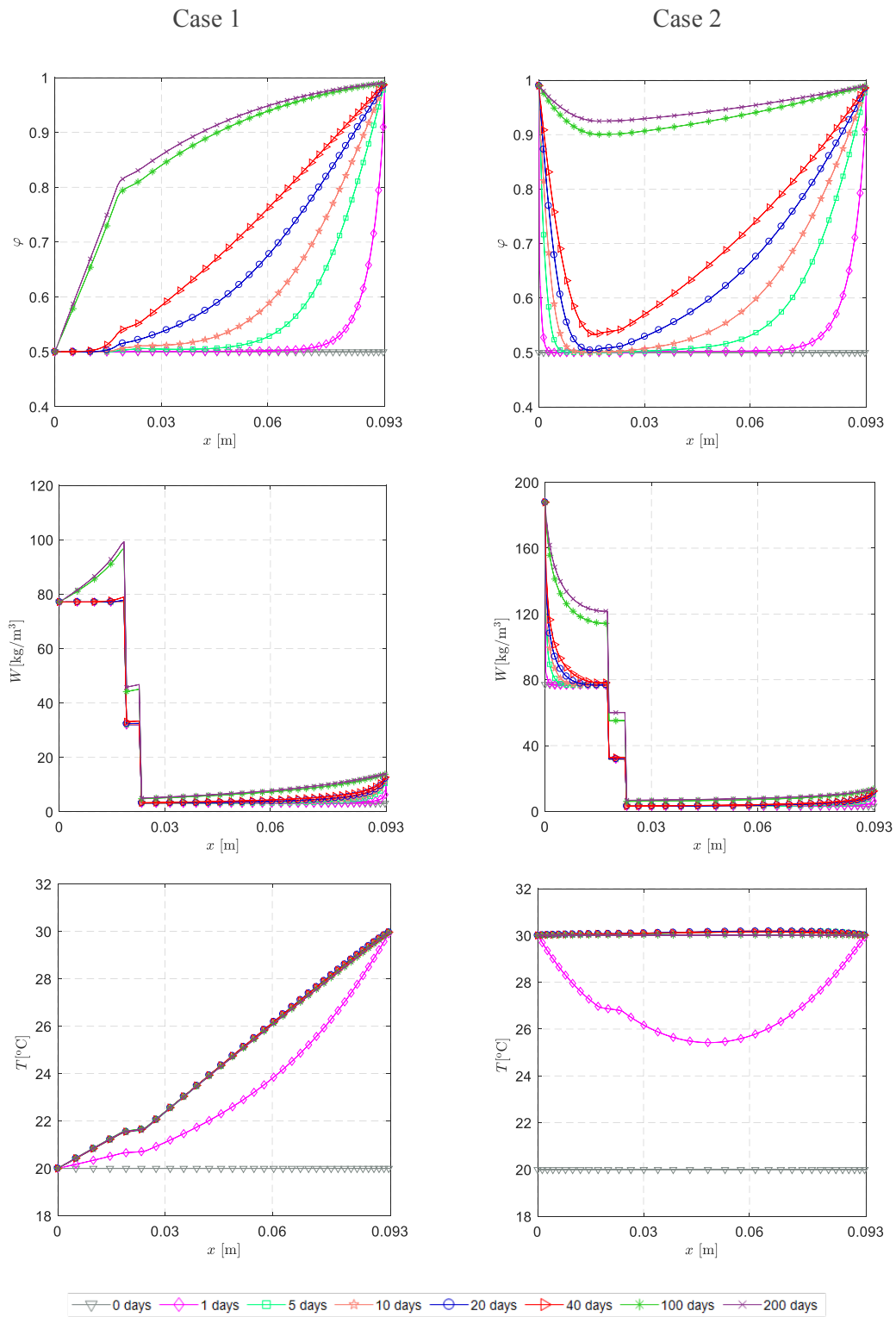


Figure 5-6: Evolution of the relative humidity, water content and temperature throughout the cross section of the constructive solution with ICB 0.070 m thick: Case 1 and Case 2.

It can be concluded that effect of the daily variation in relative humidity on the hygrothermal behaviour of an ICB coated wall is negligible. Thus, it is only relevant when there are

significant weather changes during the course of the year. Therefore, a series of cases were studied in which the weather changed significantly between the winter and the summer.

5.7 Case studies

5.7.1 Constructive solutions

Two constructive hypothetical solutions were simulated: an OSB board, 0.018 m thick, supports the ICB; a concrete wall, 0.100 m thick, is coated with ICB. A 0.005 m layer of mortar is used to bond the ICB layer to the support in both cases. For each constructive solution, the ICB layer is either 0.070 m or 0.150 m thick. The constructive solutions are represented in Figure 5-7.

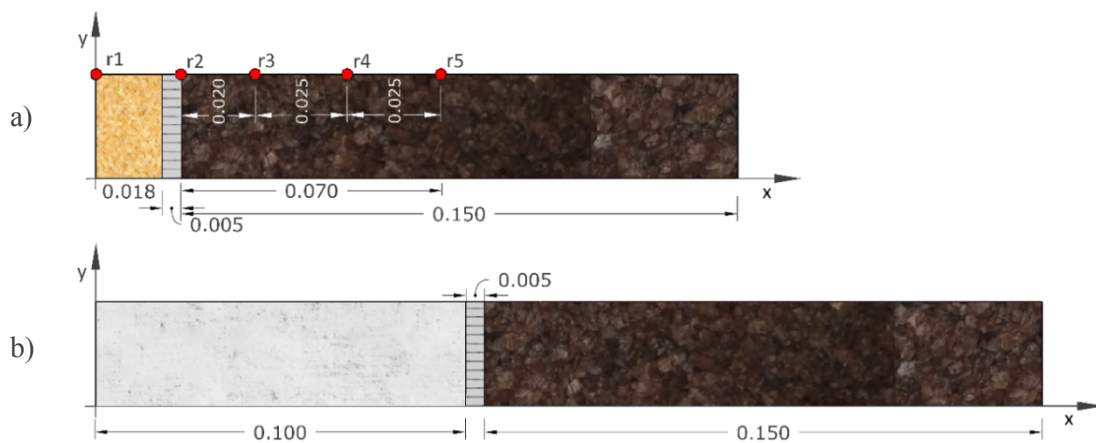


Figure 5-7: Constructive solutions: a) OSB (0.018m)/mortar (0.005m) and ICB (0.070/0.150m); b) Concrete (0.100m)/mortar (0.005m) and ICB (0.070/0.150m).

5.7.2 Real climate data

As shown before, the relative humidity within the wall varies quite slowly over time. In light of this, two cities with distinct climatic characteristics were selected, Bragança and Seville, to illustrate the main findings. Bragança has a mild summer with low humidity levels and the winter is cold and damp, while Seville has a sunny warm summer with low humidity levels, and although the mean temperature in winter is also low, the relative humidity levels are considerably lower than in Bragança. The data used in the numerical simulations were obtained from Meteonorm [40], which can generate a representative year. Periods of 132 h were used for both summer and winter to represent the climatic behaviour of the two cities.

5.7.3 Simulation results

This section first examines the evolution of the relative humidity and temperature across the OSB constructive solution coated with 0.070 m thick ICB, when exposed to the transient summer and winter conditions in Bragança and Seville. The influence of the solar heat flux was also analysed. The cross-sectional relative humidity, moisture content and temperature are then presented for the OSB wall in Bragança summer conditions, for 4 selected time instants, and considering two different ICB thicknesses: 0.070 m and 0.150 m. To analyse the influence of the inner layer on the constructive solution hygrothermal behaviour, the same study was conducted for concrete and OSB constructive solutions coated with ICB 0.150 m thick, under exposure to Bragança winter conditions.

Uniform meshes with $M=200 \times 1$ macro elements were used to model the three-layer porous structures. The convergence criterion selected was $\epsilon = 10^{-7}$ and the under-relaxation parameters were set to $ur_T = 0.1$ and $ur_\phi = 0.01$ for the time dependent numerical simulation running with a time step value of $\Delta t = 120$ sec; values of underrelaxation parameters approximately 10 times smaller were selected for the steady-state case computations, used to define the initial cross-section conditions.

5.7.3.1 Summer and winter conditions for Bragança and Seville: OSB constructive solution

Figure 5-8 presents the relative humidity and temperature simulation results when the OSB constructive solution coated with 0.070 m thick ICB is subjected to summer and winter conditions in Bragança. In these plots the solar heat flux, the IN and OUT curves, correspond to the climate data used in the simulations.

The initial hygrothermal conditions of the structure for the Bragança summer and (winter) period were determined by steady-state numerical simulation subjected to the temperature and relative humidity at $t = 0$ h (Figure 5-8b and Figure 5-8c). Therefore, the following boundary conditions of the third kind were prescribed at the left internal boundary at $x = 0$ m and $0 \leq y \leq L_y$,

$$T_{a,i} = 25 \text{ °C (18 °C) and } \alpha_i = 15.00 \text{ W/(m}^2 \text{ K) for } t = 0 \text{ h} \quad (5-30)$$

$$\varphi_{a,i} = 0.5 \text{ (0.5)} \text{ and } \beta_{p,i} = 3.00 \cdot 10^{-8} \text{ s/m for } t = 0 \text{ h}$$

on the right external boundary at $x = L_x$ and $0 \leq y \leq L_y$,

$$T_{a,e} = 21.8 \text{ °C (0.4 °C)} \text{ and } \alpha_e = 50.00 \text{ W/(m}^2 \text{ K)} \text{ for } t = 0 \text{ h} \quad (5-31)$$

$$\varphi_{a,e} = 0.46 \text{ (0.91)} \text{ and } \beta_{p,e} = 2.00 \cdot 10^{-7} \text{ s/m for } t = 0 \text{ h}$$

and zero boundary conditions of the second kind were prescribed elsewhere,

$$\frac{\partial \varphi}{\partial n} = 0 \text{ and } \frac{\partial T}{\partial n} = 0 \text{ for } t = 0 \text{ h} \quad (5-32)$$

The time dependent computations were running with the heat and mass transfer coefficients defined above using the real data for the external and internal ambient values of the driving potentials.

Figure 5-8b and Figure 5-8c include the temperature and relative humidity evolution for the 5 receivers. For both cases (summer and winter), the influence of the solar radiation is clearly visible on the surface temperature and relative humidity. As was expected, when the solar heat flux increases, the surface temperature increases and the relative humidity decreases. However, when comparing the relative humidity and temperature across the wall within the two seasons, the behaviour is quite different. In summer, the outer surface's relative humidity has a daily periodic behaviour because of the daily variation of the surface temperature, which is highly influenced by the solar heat flux. It should be noted that along the wall, the relative humidity is lower than that imposed on the inner side of the wall, except at receiver r1 that is located in the inner surface of the constructive solution. This receiver exhibits a daily periodic variation as a consequence of the variation of the temperature. The receiver r4 (depth of 0.025 m), is clearly affected by the external conditions.

As Figure 5-8 shows, when the solar heat flux increases, the surface temperature also increases and the surface relative humidity decreases in a daily periodic variation. Although, the relative humidity in r4 increases/decreases with the increasing/decreasing temperature, indicating that there is a moisture flux from/to the exterior. A relative humidity time delay in relation to the surface variation can also be seen.

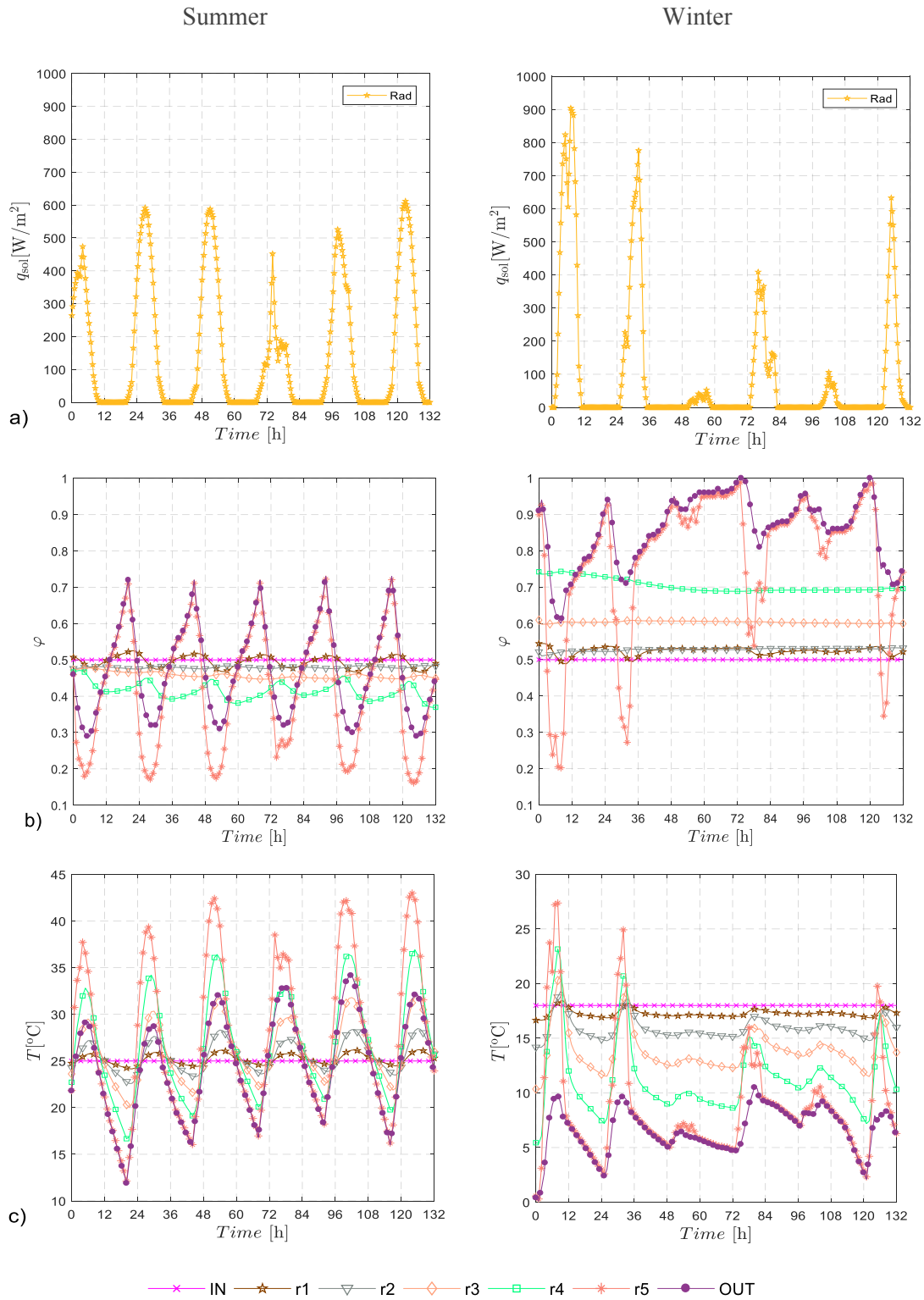


Figure 5-8: OSB constructive solution coated with ICB 0.070 m thick, subjected to Bragança climate:
a) Solar heat flux; b) Relative humidity; c) Temperature.

The variation of the external conditions has a very small influence on r3 (depth of 0.050 m). At r2 (depth of 0.070 m) the external influence is negligible as the relative humidity value remains almost constant over the entire simulation time.

In winter, the wall behaviour is quite different. Although the outer surface's relative humidity has low values when the solar heat flux is high, the relative humidity along the wall is always significantly higher than the relative humidity imposed at the inner surface, and remains almost constant throughout the simulation time. The exception was receiver r1, in which the variation of the relative humidity is a response to the temperature variation, as it had been for the summer conditions.

Under both summer and winter conditions, the temperature variation across the wall is highly dependent on the temperature and solar heat flux. For high heat fluxes, even for lower exterior air temperatures (around 10 °C), the inner surface temperature might reach values higher than the imposed air temperature of 18 °C.

As before, the initial hygrothermal conditions of the structure for the Seville summer and (winter) period were determined by steady-state numerical simulation subjected to the temperature and relative humidity at $t = 0$ h (Figure 5-9b and Figure 5-9c). The following boundary conditions of the third kind were prescribed at the left internal boundary at $x = 0$ m and $0 \leq y \leq L_y$,

$$\begin{aligned} T_{a,i} &= 25.0 \text{ °C (18.0 °C)} \text{ and } \alpha_i = 15.00 \text{ W/(m}^2 \text{ K)} \text{ for } t = 0 \text{ h} \\ \varphi_{a,i} &= 0.5 \text{ (0.5)} \text{ and } \beta_{p,i} = 3.00 \cdot 10^{-8} \text{ s/m for } t = 0 \text{ h} \end{aligned} \quad (5-33)$$

on the right external boundary at $x = L_x$ and $0 \leq y \leq L_y$,

$$\begin{aligned} T_{a,e} &= 27.1 \text{ °C (9.8 °C)} \text{ and } \alpha_e = 50.00 \text{ W/(m}^2 \text{ K)} \text{ for } t = 0 \text{ h} \\ \varphi_{a,e} &= 0.56 \text{ (0.59)} \text{ and } \beta_{p,e} = 2.00 \cdot 10^{-7} \text{ s/m for } t = 0 \text{ h} \end{aligned} \quad (5-34)$$

and zero boundary conditions of the second kind were prescribed elsewhere,

$$\frac{\partial \phi}{\partial n} = 0 \quad \text{and} \quad \frac{\partial T}{\partial n} = 0 \quad \text{for} \quad t = 0 \text{ h} \quad (5-35)$$

The summer air temperatures in Seville (Figure 5-9) are quite high and its daily variation is smaller when compared to Bragança. The relative humidity also presents a daily periodic variation, although with higher values than in Bragança. Consequently, the relative humidity at r3 and r2 were higher than the relative humidity imposed at the inner surfaces with small variations during the simulation time, in which these are a function of the local temperature variation. The inner surface relative humidity (r1), as before, is also a function of the temperature variation. Receiver r4, as in Bragança, was affected by the external conditions and a moisture flux was observed.

In winter conditions, the relative humidity daily periodic variation at r1 and r5 are caused by the temperatures variation. Receivers r2 and r3 maintain almost a constant value, close to $\phi = 0.5$ (the inner boundary condition) during the simulation time. Receiver r4 registered a slight higher relative humidity than the interior ambient, exhibiting a weak variation, lower than 0.1.

Therefore, it can be concluded that moisture along the ICB coated wall is high when the outer moisture is high and remains high. When the relative humidity, despite being high, suffers a periodic variation, the relative humidity along the wall is close to what was imposed for the inner environment.

To better illustrate the hygrothermal variation with depth, the left column in Figure 5-10 shows for Bragança's summer condition, the relative humidity, water content and temperatures along the cross section of the OSB constructive solution coated with 0.070 m thick for 4 time instants: $t = 20 \text{ h}$, 24 h , 28 h and 32 h . These time instants were selected so as to represent scenarios with high, low, and medium relative humidity levels.

This figure confirms that the relative humidity variation in the wall is limited to the surface layers (shallow depths up to 0.02 m), given that moisture flow is very slow. Similarly, the water content variation only affects the outer surface layers. In contrast, as expected, the temperature variation changes through the full cross section.

To assess the importance of the ICB thickness on the hygrothermal behaviour, Figure 5-10 (right column) gives the results for ICB 0.150 m thick. The relative humidity results for the surface layers appears to be shifted from the former results found for the 0.070 m thick ICB.

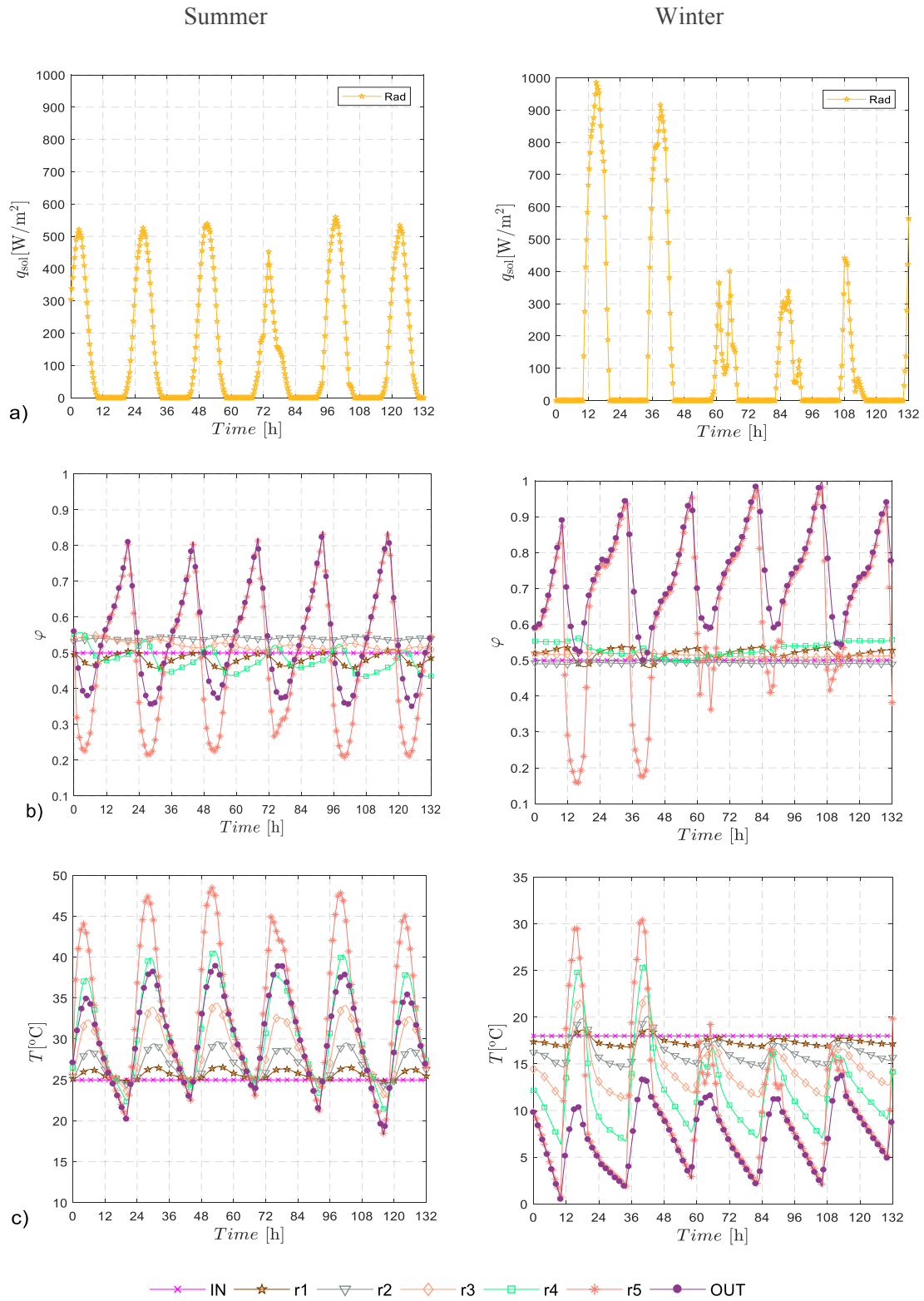
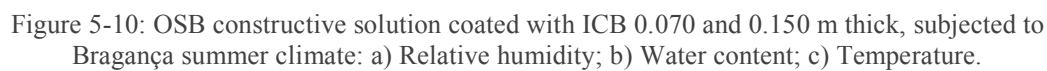


Figure 5-9: OSB constructive solution coated with ICB 0.070 m thick, subjected to Seville climate:
a) Solar heat flux; b) Relative humidity; c) Temperature.



The water content evolution (Figure 5-10b) clearly shows the adsorption and desorption processes in the vicinity of the outer boundary. When the temperature decreases (Figure 5-10c), the relative humidity increases (Figure 5-10a), as does the moisture content, indicating that moisture is absorbed from the surrounding air and thereby increasing the absolute humidity in the outer layer of the ICB. The opposite also occurs. An increase in the temperature leads to a decrease in the relative humidity but also induces a desorption process in which moisture is released into the surrounding air. It can therefore be said that on and in the vicinity of the surface the relative humidity varies as a function of the temperature variation, as previously stated, but also due to water content variation, in a cyclic adsorption/desorption process.

The temperatures across the two walls for the 4 time instants are quite different and depend strongly on the boundary conditions.

5.7.3.2 OSB versus concrete constructive solutions

To analyse the influence of the inner layer (the supporting layer) on the constructive solution hygrothermal behaviour, the same study was repeated for concrete and OSB constructive solutions coated with ICB 0.150 m thick, when exposed to Bragança winter conditions. Figure 5-11 gives the relative humidity, water content and temperature variation along the cross section of both OSB (left column) and concrete (right column) walls. As before, 4 time instants were selected that are representative of high, low, and medium relative humidity levels: $t = 8$ h, 16 h, 25 h and 32 h.

The numerical simulations were performed using the above prescribed boundary conditions.

As in the previous case, the relative humidity, water content and temperature at the outer wall surface are similar for both walls.

For both cases the relative humidity drops within the supporting layer until it reaches the mortar/ ICB bonding interface. The relative humidity then increases up to a depth of 0.025 m from the outer surface, after which the daily periodic climate variations affects the hygrothermal behaviour. This happens for all the 4 time instants and for both walls, showing that, as before, the variation of the external relative humidity does not have a short-term effect in the wall's inner layers.

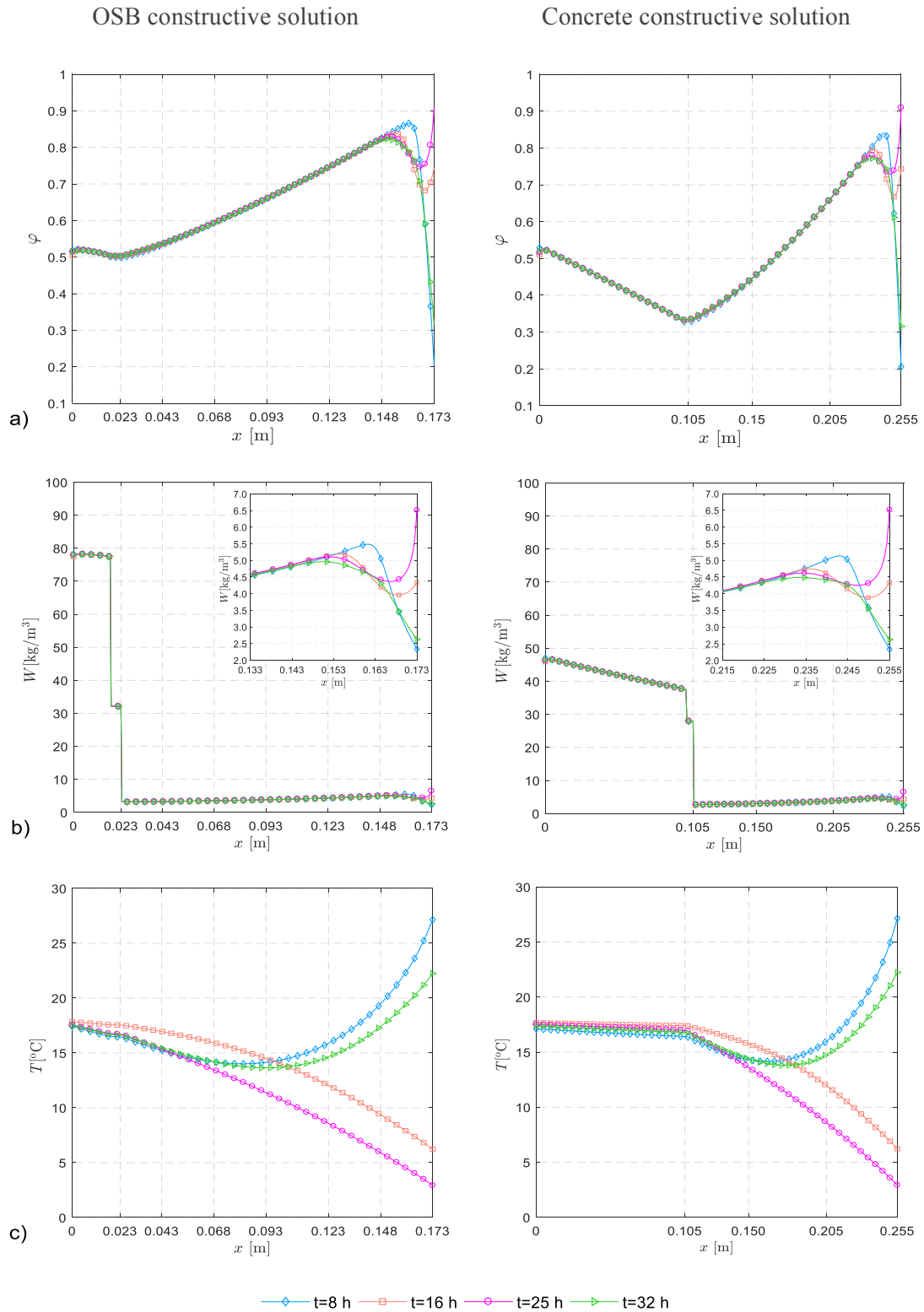


Figure 5-11: OSB and Concrete constructive solutions coated with ICB 0.150 m thick, subjected to Bragança winter climate: a) Relative humidity; b) Water content; c) Temperature.

However, the maximum relative humidity at depths not affected by the external periodic variations is higher for the OSB constructive solution. As the surface relative humidity for the 4 time instants was similar for both walls, the OSB wall must adsorb more water when $t = 8$ and 32 h (low values of surface ϕ) and desorbs less water when $t = 16$ and 25 h (high values of surface ϕ). This phenomenon is clearly seen in Figure 5-11b, in which the water content curves in the vicinity of the outer layer have higher values than those in the concrete wall.

Figure 5-11c presents the temperatures for the 4 time instants. As before, for both walls the temperature is highly dependent on changes in the boundary conditions. However, is noticeable that the temperatures for the 4 time instants across the concrete layer have similar values, due to the high thermal conductivity of the concrete.

5.8 Final remarks

This work evaluated the hygrothermal behaviour of two wall types (OSB and concrete) covered with uncoated medium density expanded cork board, under exposure to real climate data, namely, temperature, relative humidity and solar heat flux. For this purpose, a numerical model that simulates the coupled heat and moisture transfer in a porous layered building wall was used.

First, the hygrothermal properties of the medium density expanded cork were determined and validated experimentally using a calibrated hot-box. The experimental results for the OSB wall covered with an uncoated medium density ICB subjected to unsteady heat and moisture flow were found to be in a good agreement with the numerical simulations.

The changes in the driving potentials over time, such as relative humidity, moisture content, and temperature, along the cross section of an uncoated medium density ICB covered wall were analysed by performing a numerical simulation over a period of 200 days. It was found that the transport of heat through a wall covered with uncoated medium density ICB is several orders of magnitude higher than the transport of moisture, leading to the conclusion that moisture transport through the wall is only relevant when there are significant weather changes during the course of the year. Thus, the summer and winter climate conditions of Bragança and Seville were selected to illustrate the main hygrothermal behaviour features.

The variation of temperature, relative humidity and moisture content throughout OSB and concrete walls, as a function of the climate data, were then evaluated by performing numerical

simulations for periods of 132 h that are representative of the summer and winter weather conditions in Bragança and Seville.

Besides of the great impact of the solar heat flux on the surface temperature and relative humidity, it was found that the short-term environment moisture variation has no effect beyond the surface layers in terms of the relative humidity across a wall covered with uncoated medium density ICB. This is due to the rather slow process of moisture diffusion within the ICB. As for the other wall layers, these are not affected. Therefore, it can be concluded that moisture along the ICB coated wall is only high when the exterior moisture is high, and remains that way. When the relative humidity, despite being high, varies periodically, the relative humidity along the wall is similar to that in the interior environment. However, a change in the exterior surface temperature, changes the temperatures across the entire wall in a short time.

5.9 References

- [1] E. Commission, Communication from the Commission to the European Parliament, the Council, the European economic and social committee and the committee of the region - COM 571 - Roadmap to a Resource Efficient Europe, 2011.
- [2] A. Korjenic, J. Zach, J. Hroudová, The use of insulating materials based on natural fibers in combination with plant facades in building constructions, *Energy Build.* 116 (2016) 45–58. doi:10.1016/j.enbuild.2015.12.037.
- [3] F. Pacheco-Torgal, Eco-efficient construction and building materials research under the EU Framework Programme Horizon 2020, *Constr. Build. Mater.* 51 (2014) 151–162. doi:10.1016/j.conbuildmat.2013.10.058.
- [4] F.A.O. Fernandes, R.T. Jardim, A.B. Pereira, R.J. Alves de Sousa, Comparing the mechanical performance of synthetic and natural cellular materials, *Mater. Des.* 82 (2015) 335–341. doi:10.1016/j.matdes.2015.06.004.
- [5] L. Gil, Cork: Sustainability and New Applications, *Front. Mater.* 1 (2015) 2014–2016. doi:10.3389/fmats.2014.00038.
- [6] A.S. Tártaro, T.M. Mata, A.A. Martins, J.C.G. Esteves da Silva, Carbon footprint of the insulation cork board, *J. Clean. Prod.* 143 (2017) 925–932. doi:10.1016/j.jclepro.2016.12.028.

- [7] R. Peuhkuri, *Moisture Dynamics in Building Envelopes*, Technical University of Denmark, 2003.
- [8] K.B. Najim, External load-bearing walls configuration of residential buildings in Iraq and their thermal performance and dynamic thermal behaviour, *Energy Build.* 84 (2014) 169–181. doi:10.1016/j.enbuild.2014.07.064.
- [9] G. Manioğlu, Z. Yilmaz, Economic evaluation of the building envelope and operation period of heating system in terms of thermal comfort, *Energy Build.* 38 (2006) 266–272. doi:10.1016/j.enbuild.2005.06.009.
- [10] A. Antonyová, A. Korjenic, P. Antony, S. Korjenic, E. Pavlušová, M. Pavluš, T. Bednar, Hygrothermal properties of building envelopes: Reliability of the effectiveness of energy saving, *Energy Build.* 57 (2013) 187–192. doi:10.1016/j.enbuild.2012.11.013.
- [11] M. Rahim, O. Douzane, A.D. Tran Le, G. Promis, T. Langlet, Experimental investigation of hygrothermal behavior of two bio-based building envelopes, *Energy Build.* 139 (2017) 608–615. doi:10.1016/j.enbuild.2017.01.058.
- [12] T. Odgaard, S.P. Bjarløv, C. Rode, Interior insulation – Experimental investigation of hygrothermal conditions and damage evaluation of solid masonry façades in a listed building, *Build. Environ.* 129 (2018) 1–14. doi:10.1016/j.buildenv.2017.11.015.
- [13] M. Labat, M. Woloszyn, G. Garnier, J.J. Roux, Dynamic coupling between vapour and heat transfer in wall assemblies: Analysis of measurements achieved under real climate, *Build. Environ.* 87 (2015) 129–141. doi:10.1016/j.buildenv.2015.01.022.
- [14] N. Simões, I. Simões, A. Tadeu, C.A.B. Vasconcellos, W.J. Mansur, 3D transient heat conduction in multilayer systems – Experimental validation of semi-analytical solution, *Int. J. Therm. Sci.* 57 (2012) 192–203. doi:10.1016/j.ijthermalsci.2012.02.007.
- [15] J.R. Philip, D.A. De Vries, Moisture movement in porous materials under temperature gradients, *Trans. Am. Geophys. Union.* 38 (1957) 222–232. doi:10.1029/TR038i002p00222.
- [16] A.V. Luikov, Systems of differential equations of heat and mass transfer in capillary-porous bodies (review), *Int. J. Heat Mass Transf.* 18 (1975) 1–14. doi:10.1016/0017-9310(75)90002-2.

- [17] B. Seng, S. Lorente, C. Magniont, Scale analysis of heat and moisture transfer through bio-based materials — Application to hemp concrete, *Energy Build.* 155 (2017) 546–558. doi:10.1016/j.enbuild.2017.09.026.
- [18] T. Krejčí, J. Kruis, M. Šejnoha, T. Koudelka, Numerical analysis of coupled heat and moisture transport in masonry, *Comput. Math. with Appl.* 74 (2017) 229–248. doi:10.1016/j.camwa.2017.03.022.
- [19] H.M. Künzels, K. Kiessl, Calculation of heat and moisture transfer in exposed building components, *Int. J. Heat Mass Transf.* 40 (1996) 159–167. doi:10.1016/S0017-9310(96)00084-1.
- [20] K. Abahri, R. Belarbi, A. Trabelsi, Contribution to analytical and numerical study of combined heat and moisture transfers in porous building materials, *Build. Environ.* 46 (2011) 1354–1360. doi:10.1016/j.buildenv.2010.12.020.
- [21] L. Škerget, A. Tadeu, BEM numerical simulation of coupled heat and moisture flow through a porous solid, *Eng. Anal. Bound. Elem.* 40 (2013) 154–161. doi:10.1016/j.enganabound.2013.12.006.
- [22] H. Min, W. Zhang, X. Gu, R. Černý, Coupled heat and moisture transport in damaged concrete under an atmospheric environment, *Constr. Build. Mater.* 143 (2017) 607–620. doi:10.1016/j.conbuildmat.2017.03.163.
- [23] L. Škerget, A. Tadeu, J. Ravnik, BEM numerical simulation of coupled heat, air and moisture flow through a multilayered porous solid, *Eng. Anal. Bound. Elem.* 74 (2017) 24–33. doi:10.1016/j.enganabound.2016.10.004.
- [24] A. Holm, H.M. Künzels, Combined effect of temperature and humidity on the deterioration process of insulation materials in ETICS, *Proc. 5th Symp. Build. Phys.* (1999).
- [25] WUFI PC-Program for calculating the coupled heat and moisture transfer in building components.
- [26] P.H. Coons, E.M. Sparrow, J.M. Gorman, Temperature and heat flux at residential surfaces due to solar-beam radiative selectivity, geography/climate, insulation/structural configuration, humidity, and sky condition, *Therm. Sci. Eng. Prog.* 3 (2017) 102–113. doi:10.1016/j.tsep.2017.07.001.
- [27] K. Kant, A. Shukla, A. Sharma, Heat transfer studies of building brick containing phase

- change materials, *Sol. Energy*. 155 (2017) 1233–1242. doi:10.1016/j.solener.2017.07.072.
- [28] B. Cho, D. Park, J. Kim, H. Hamasaki, Study on the heat-moisture transfer in concrete under real environment, *Constr. Build. Mater.* 132 (2017) 124–129. doi:10.1016/j.conbuildmat.2016.11.121.
- [29] L. Škerget, A. Tadeu, C.A. Brebbia, Transient simulation of coupled heat and moisture flow through a multi-layer porous solid exposed to solar heat flux, *Int. J. Heat Mass Transf.* 117 (2018) 273–279. doi:10.1016/j.ijheatmasstransfer.2017.10.010.
- [30] M. Van Belleghem, M. Steeman, H. Janssen, A. Janssens, M. De Paepe, Validation of a coupled heat, vapour and liquid moisture transport model for porous materials implemented in CFD, *Build. Environ.* 81 (2014) 340–353. doi:10.1016/j.buildenv.2014.06.024.
- [31] T. Colinart, P. Glouannec, M. Bendouma, P. Chauvelon, Temperature dependence of sorption isotherm of hygroscopic building materials. Part 2: Influence on hygrothermal behavior of hemp concrete, *Energy Build.* 152 (2017) 42–51. doi:10.1016/j.enbuild.2017.07.016.
- [32] M. Jerman, R. Černý, Effect of moisture content on heat and moisture transport and storage properties of thermal insulation materials, *Energy Build.* 53 (2012) 39–46. doi:10.1016/j.enbuild.2012.07.002.
- [33] O. López, I. Torres, A.S. Guimarães, J.M.P.Q. Delgado, V.P. de Freitas, Inter-laboratory variability results of porous building materials hygrothermal properties, *Constr. Build. Mater.* 156 (2017) 412–423. doi:10.1016/j.conbuildmat.2017.08.184.
- [34] F. Tariku, K. Kumaran, P. Fazio, Transient model for coupled heat, air and moisture transfer through multilayered porous media, *Int. J. Heat Mass Transf.* 56 (2010) 3035–3044.
- [35] L.C. Wrobel, *The boundary element method. Vol 1 Applications in thermo-fluids and acoustics*, John Wiley & Sons, Ltd, New York, 2002.
- [36] M. Ramšak, L. Škerget, A subdomain boundary element method for high-Reynolds laminar flow using stream function-vorticity formulation, *Int. J. Numer. Methods Fluids*. 46 (2004) 815–847. doi:10.1002/fld.776.
- [37] V. Popov, H. Power, L. Škerget, eds., *Domain Decomposition Techniques for*

- Boundary Elements, Application to Fluid Flow, Advances in Boundary Element Series, WIT Press, Southampton, Boston, 2007.
- [38] H.M. Künzl, Simultaneous Heat and Moisture Transport in Building Components – One- and two-dimensional calculation using simple parameters -Technical Report, 1995.
- [39] I. Torres, Rising damp in historical buildings walls, FCTUC ; PhD Thesis [in portuguese], 2004.
- [40] <http://www.meteonorm.com/en/> (accessed July 5, 2017).

Chapter 6

Validation of the Solutions when Subjected to
Wind, Rain and Impact Loads

6.1 Introduction

As described in the previous chapters, the production of expanded cork board, a natural and fully recycled material commercially known as ICB, which promotes the recycling of agricultural waste [1], is increasingly being used to externally insulate the thermal envelope of buildings (roofs and facades). However, the external application of this material presents a novel solution which needs to meet a number of functional requirements associated with external coating solutions. These include protecting the building against weathering and mechanical stresses, providing an appearance and aesthetic compatible with the intended architectural solution, while being integrated within the environment in which the building is implemented, as well as remaining clean (or being easy to clean).

The envelopes of buildings are permanently exposed to environmental effects, such wind pressure or the combined effect of wind and rain (wind driving rain). The pressure generated by the wind acts both on the structure of the building and on the building's external cladding. It is dependent on the buildings shape, orientation and height, as well as on wind velocity and direction [2]. In turn, the speed and direction of the wind are influenced by the topography of the ground, as well as on the neighbouring buildings. A building inserted in a complex environment may be subject to different wind flow mechanisms, such as wake effects and channelling. These flow mechanisms are dependent on the height, shape, and on the relative location of the surrounding structures [3].

On the windward side of the building, the wind pressure is positive and pushes onto the building structure. However, when the wind flows around the building, very high suction pressures are generated, due to the formation of vortices. These occur mainly at the building leeward side and on the leading edges as well as on the roof [4–6]. In these areas, to avoid the risk of detachment, the cladding must be firmly bonded to the building structure [7]. Thus, to guarantee the mechanical integrity of the building envelope, its cladding, which includes the bonding system, must be tested for wind-induced suction forces. In addition, the external use of ICB (without coating) needs to ensure the water-tightness of the building envelope.

In Chapter 4, a solution consisting of an OSB panel covered with 70 mm thick medium density (MD) ICB boards was tested under dry and wet conditions. In this study, it was observed that, when the solution was exposed to a horizontal water spray, the water infiltration throughout the ICB had low penetration. In fact, the water did not reach the interface between the ICB

and the bonding mortar. These tests were performed without any pressure difference between the internal and the external environments. However, the penetration depth of the water through the ICB boards is expected to be related with intensity and frequency of the rain and with wind velocity [8], which generates a differential pressure between the inner and outer faces of the wall. Because the water under pressure may reach the bonding mortar that attaches the ICB boards to the support, it is fundamental for the bonding mortar to provide water-tightness, while ensuring vapour permeability. Hence, the ICB solution should be subjected to wind driving rain conditions in order to determine if it remains watertight, and if the bonding layer maintains its adhesion.

Performing water-tightness tests consists in subjecting the outer surface of a full-scale test sample to a pressure differential and to the spraying of water. The leak tightness of the solution is checked by visual inspection of the inner surface of the test specimens for any water infiltration. The air pressure and water spray rate used in the tests is related with the combination of environmental factors to which the components are subject to under service [9]. The estimation of the severity of the exposure of buildings facades to driving rain has been studied by several authors for different climate conditions experienced in several countries, namely Pérez-Bella et al. for Spain [10] and for Chile [11], Giarmar and Aravantinos [12] for Greece, Chand and Bhargava [13] for India, Rydock et al. [14] for Norway.

In addition to ensuring that the building is watertight and wind resistant, a facade solution must also withstand mechanical actions such as impact loads. The mechanical properties of ICB have been previously addressed in Chapter 3. It was shown that MD ICB exhibits good mechanical performance. However, since facades at ground level are particularly vulnerable to impacts, an actual wall with externally applied ICB should be tested.

Several studies regarding the resistance to impact of different constructive solutions can be found in the literature. Sanchez-Saez et al. [15] observed, by performing impact tests on agglomerated cork, that the thickness of the material does not influence the energy-absorption capabilities in the studied energy range. Ferreira et al. [16] subjected sandwich panels for wall assemblies in buildings (with cork agglomerate core and glass fibre reinforced polymer facings) to impact tests. Satisfactory behaviour to impact for both panel and connections were observed. The ability of carbon-cork agglomerates sandwich panels to withstand dynamic loads was evaluated by Castro et al. [18]. After performing a set of impact tests the authors noticed that all cork-based sandwiches, regardless of the type of granulate, presented higher

impact resistance, when compared with the other types of high-performance core materials studied.

When applied externally in actual building facades, ICB will be subjected to the effects of wind and rain, as well as to accidental impacts. Hence, the full evaluation of the behaviour of ICB-coated constructive solutions when exposed to these external aggressions, regarding both the material's performance and the strength of the adhesion, is considered to be essential. In order to undertake this analysis, several specimens incorporating different materials with externally applied ICB were built and tested. These tests included suction, suction after prolonged wetting, water-tightness and resistance to impact.

In the following sections, the three different test specimens built for these experiments are presented (MD ICB coated OSB, MD ICB coated metal panels, and omega profiles). Then, the performed tests are briefly described, and the obtained results are presented.

6.2 Experimental characterisation of constructive solutions

Since uncoated ICB is intended to act both as external thermal insulation and as the envelope's external cladding, the constructive solutions will be exposed to the simultaneous effects of wind and rain. As mentioned, in the presence of pressure gradients generated by wind, during rainy periods the penetration in the wall is expected to be able to reach the interface between the ICB and the bonding mortar. Therefore, the bonding mortar layer must provide water-tightness, ensure mechanical resistance to suction and inward loads, and guarantee vapour permeability. Furthermore, the whole solution is required to resist to impact loads.

All three specimens were built using MD ICB boards, with nominal dimensions of (1000×500×70) mm³. The three test specimens selected for this study correspond to the following constructive solutions:

- OSB base;
- corrugated metal panels base;
- steel profiles frame.

The latter two solutions were selected due to the importance of studying the mechanical resistance of an expanded cork board-bonding mortar interface with reduced area.

The following sections of this chapter describe the tests performed and provide a discussion of the obtained results.

6.2.1 Construction of the test specimens

First, a metal frame with inner dimensions of 2600 mm × 2050 mm, is built to support the test specimens. It uses tubular metal profiles RHS 150 mm × 100 mm × 4 mm along its entire perimeter and horizontal tubular metal sections RHS 50 mm × 50 mm × 3 mm, equally spaced by 500 mm. Figure 6-1 illustrates the layout of this frame.

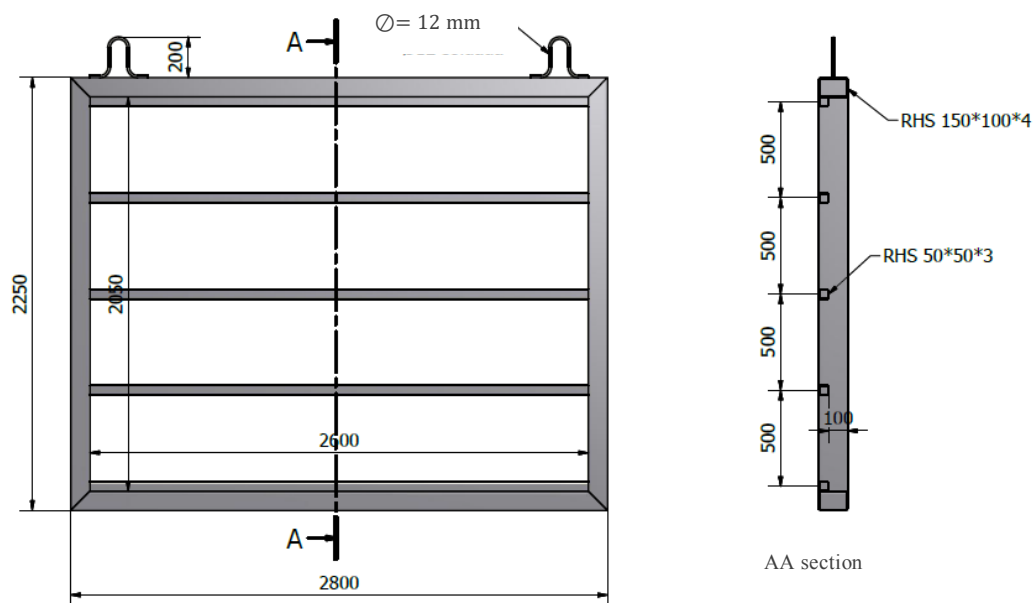


Figure 6-1: Front view of the metal frame and cross section AA (dimensions in mm).

- **Assembly of OSB and corrugated metal panels systems**

An OSB board was assembled on the right side of the frame (Figure 6-2a). Then, a primer was applied to the OSB panel (Figure 6-2b). After the required curing time (8 hours), a first coat of regularisation/waterproofing mortar (Figure 6-2c) was applied, over which a fiberglass mesh was applied (Figure 6-2d). A second and third coat of regularisation/waterproofing mortar was then applied (Figure 6-2e). Once dry, the MD ICB boards were applied by double bonding, using the same type of mortar.

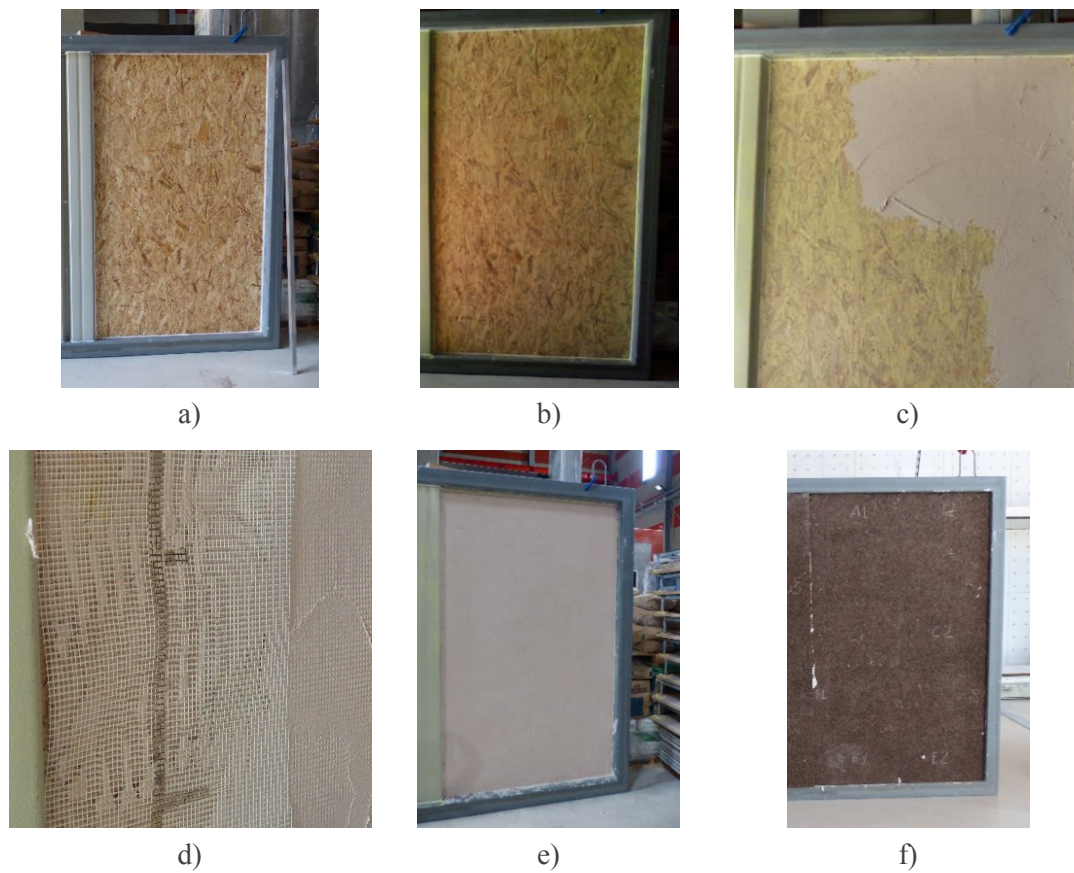


Figure 6-2: OSB specimen: a) OSB boards mounted on the frame; b) Application of the primer; c) Application of the 1st coat of regularisation/waterproofing mortar; d) Application of a fiberglass mesh; e) Appearance of the specimen after the application of the 2nd and 3rd coat of regularisation/waterproofing mortar; f) OSB coated with the ICB.

A corrugated metal panel was mechanical fixed on the left section of the metal frame, as illustrated in Figure 6-3a.

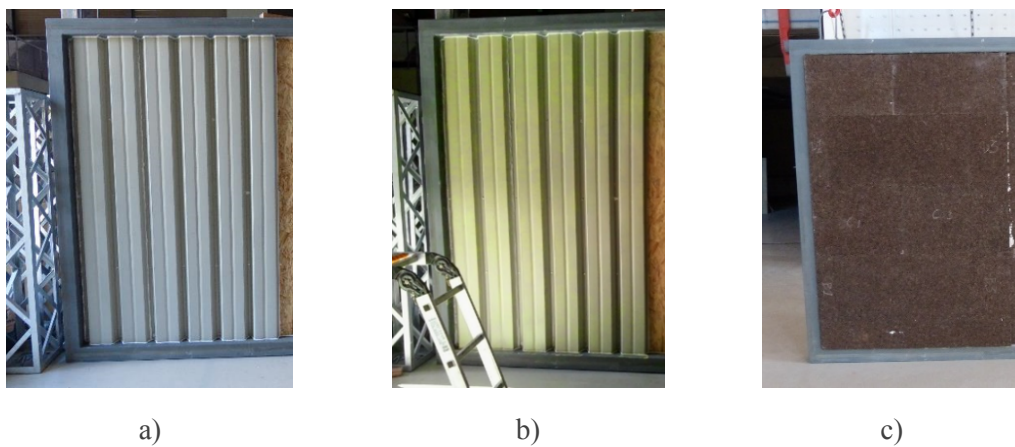


Figure 6-3: Corrugated metal panel assembly: a) Fixation of the corrugated metal panel; b) Application of the primer; c) Corrugated metal panel coated with ICB.

The connection of the corrugated metal panel with the metal frame and all screws were sealed to ensure water-tightness. The metal panel was coated with a primer before applying the MD ICB boards so as to ensure proper cohesive adhesion (Figure 6-3b). After the required curing time (8 hours), the MD ICB boards were then applied with double bonding. Figure 6-3c presents the appearance after the assemblage was finished.

- **Assembly of steel profile systems**

In the case of the steel profiles specimen, the ICB boards were fixed directly to the anodized aluminium profiles with omega cross-section, as shown in Figure 6-4a. The profiles were positioned to allow the cork boards to be fixed on the omega wings, as shown Figure 6-4b. The boards had a 35 mm × 35 mm milling on all sides in order to hold a half lap splice in height and width. With this milling, each board covers an area of (965×465) mm².

In this type of application, the ICB boards are not continuously bonded to the support. In order to evaluate the fixing capacity and the mechanical resistance of the cork boards, the following steel profile systems were tested:

- **Zone A:** profiles are 485 mm apart (each ICB board is fixed on both ends and along the centre);
- **Zone B:** profiles are 242.5 mm apart (the ICB is fixed onto 5 profiles).

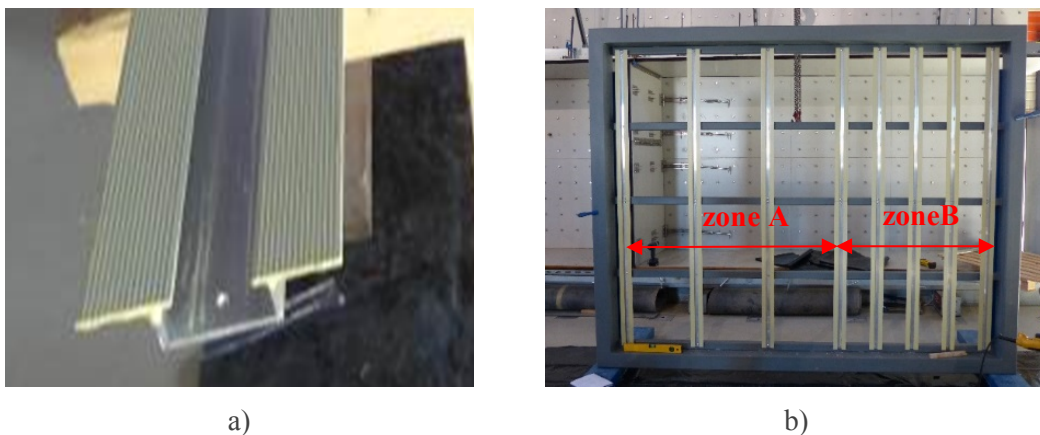


Figure 6-4: Omega profiles application: a) Omega profile with primer; b) Frame with the identification of the two steel profiles systems.

The MD ICB boards were applied after coating of the steel omega profile wings with a primer. After the required curing time, the bonding mortar was applied to both the profiles systems (see Figure 6-5a) and to the MD ICB boards, but only in the interface zones, as shown in

Figure 6-5b). Additionally, self-tapping screws were applied (positioned as indicated by the red circles in Figure 6-5c).

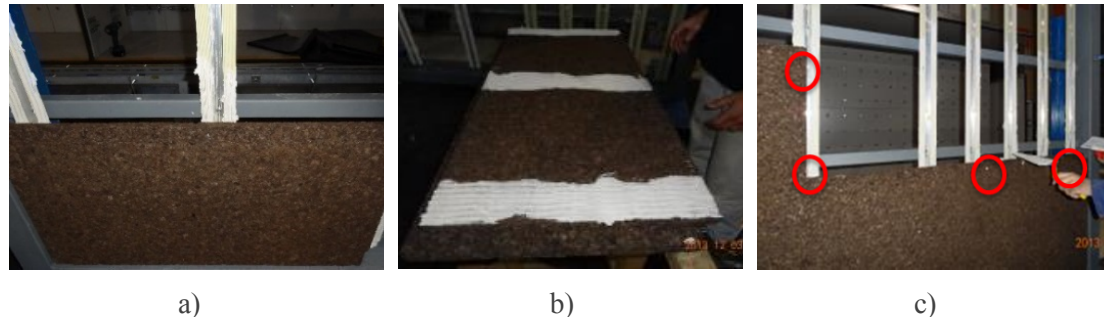


Figure 6-5: Assembly sequence of the MD ICB onto the omega profiles: a) Application of the bonding mortar to the profiles; b) Application of the bonding mortar to the MD ICB; c) Mechanical fixing.

6.2.2 Test procedures

As mentioned before, the building envelope is exposed to high wind-induced suction forces. Suction tests were performed on the test specimens, to ensure that both the ICB and the bonding system resist to extreme wind conditions. However, as the constructive solutions can be exposed to rain, a question arose on whether they would maintain the required resistance to suction also after being subjected to wetting. Therefore, suction tests were performed after the specimens were subjected to prolonged wetting. The OSB specimen was additionally subjected to a water-tightness test.

ICB coated steel omega profiles have a significant area in which the ICB boards do not have any support base, and therefore may be more vulnerable to impact loads. Thus, to assess the feasibility of this constructive solution system when exposed to accidental impacts, hard and soft body impact tests were also performed.

The following paragraphs describe the procedures followed for these tests. These are based on ETAG 034 Part I [18], EN 12155:2000 [19] and ISO 7892:1988 [20].

- **Suction tests before and after prolonged wetting**

The suction test, which is intended to simulate the suction effect that the wind has on the building's cladding, consists in applying a uniformly distributed load of suction to the outer face of the facade elements and on recording the deformation of these elements and the integrity of the specimen under test.

The test rig was mounted on a chamber equipped with a fan and a differential pressure transducer. The fan draws air out from the chamber until the specified value of differential pressure is reached.

The following consecutive suction levels were applied (see Figure 6-6): 2 levels at 300 Pa, 1 level at 500 Pa, 1 level at 1000 Pa and thereafter the levels increase in increments of 200 Pa up to 3000 Pa, with a return to 0 Pa after the solicitation of each suction level. Each suction level is applied during at least 10 seconds after the stabilisation of the deformations. The suction load is then withdrawn and the residual strain, after 1 minute, is recorded.

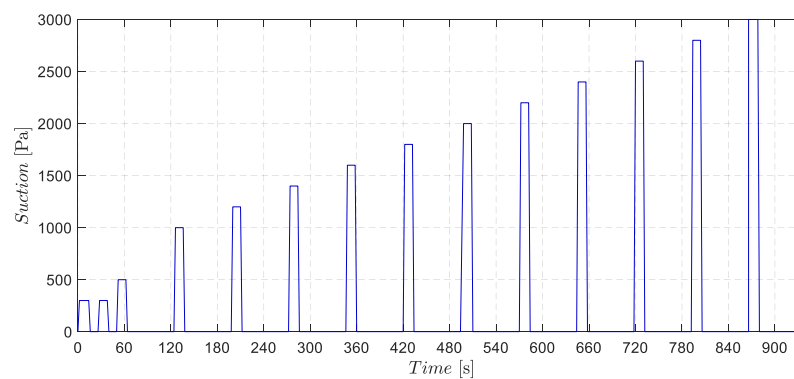


Figure 6-6: Test suction levels.

Assuming that all of the kinetic energy of the air in motion is transformed into static pressure when in contact with the wall [2], the maximum applied pressure of 3000 Pa corresponds to a category 5 hurricane according to the Saffir–Simpson hurricane scale.

To evaluate whether the specimens maintain the suction resistance under wet conditions, these were subjected to prolonged wetting for 94 hours. The wetting apparatus consists of a grid of water sprinklers uniformly distributed on the outer surface of the wall which ensures a uniform water flow rate of 2 L/(m² min). Then the specimens were, again, subjected to the previously described wind suction test.

- **Water-tightness test**

This test allows the evaluation of the water-tightness level of the specimen wall by exposing its outer surface to a continuous thin layer of water and to incremental positive static pressure, applied at defined time intervals.

The test was performed according to the following procedures:

- 1) A maximum test pressure of 2000 Pa was defined;
- 2) The water spraying system was activated with a 0 Pa test pressure. The total water flow was adjusted to provide 2 L/(m² min);
- 3) After 20 minutes of water spraying at 0 Pa, the test pressure was increased, as shown in Figure 6-7, up to the maximum test pressure;
- 4) The inner face of the wall was continuously inspected, looking for any water leakage.

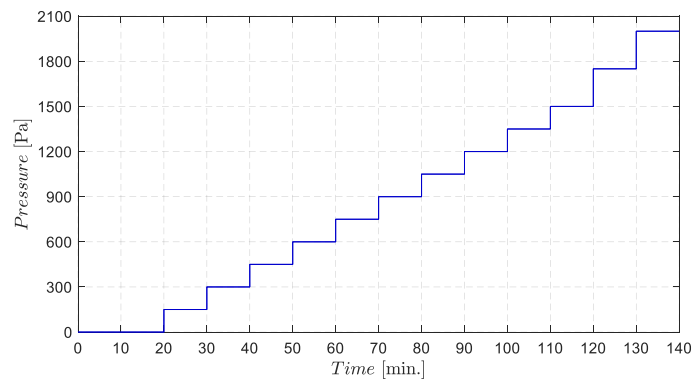


Figure 6-7: Sequence of applied pressures during the water-tightness test.

• Impact tests

The specimens were subjected to the impact from hard and large soft bodies. The test setups are illustrated in Figure 6-8.

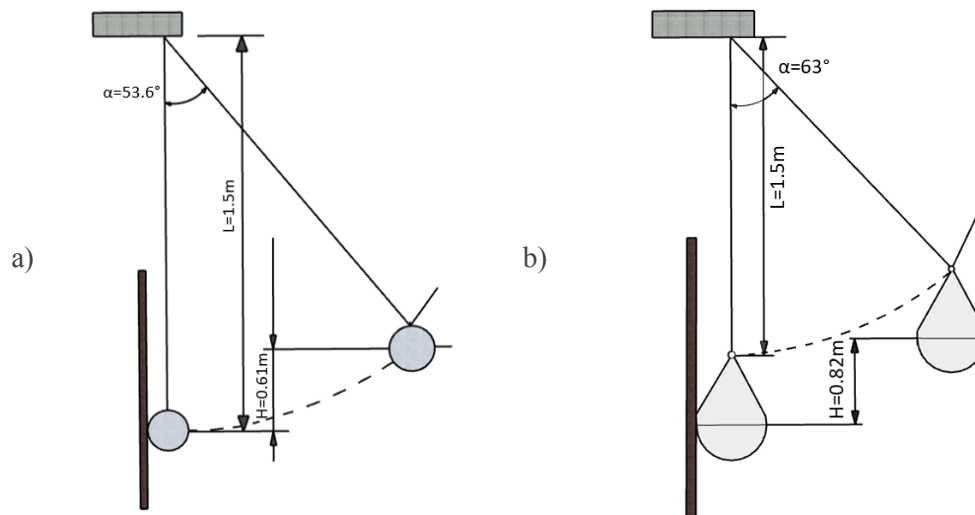


Figure 6-8: Impact test layout: a) Hard body; b) Large soft body.

The hard and soft body impact tests were performed with: a steel ball weighing 0.5 kg and a soft body weighing 50 kg. The drop height was defined so as to generate an impact energy of 3 J using the hard body of the steel ball and 400 J using the soft body.

6.2.3 Test results

This section presents a brief discussion of the experimental tests results.

- **OSB and metal panels systems**

First, the OSB and metal panel specimens wall was fitted on to the test chamber and subjected to the suction test. The test was performed according to the procedure described before.

After the end of the test, it was observed that, up to the maximum pressure of 3000 Pa, the wall withstood this pressure, both in the metal zone and in the OSB zone, without suffering any failure or excessive residual deformations (0.39 mm for the OSB panel and 0.33 mm for the metal panel). Thus, it was considered that even at a maximum pressure of 3000 Pa, the specimens presented good performance regarding wind resistance.

The wall was then subjected to prolonged wetting for 94 hours, as described previously, to ensure that the integrity of both the ICB and the bonding system under wet conditions. After this time, the suction test was repeated. It was concluded that the specimen maintained its integrity.

The water-tightness test was performed on the OSB constructive solution to simulate the effect of the wind driving rain. The test was carried out until a pressure of 2000 Pa was reached.

The test rig was then fitted onto the chamber previously used to perform the suction test, in which a wetting apparatus that provides a continuous water flow rate of 2 L/(m².min) was installed, as aforementioned. However, in this test, the specimen was subjected to positive static pressure increments at the same time as it was being sprayed with water.

A careful visual and thermographic inspection showed the integrity of the specimen sealing. The specimen remained watertight, as can be seen in Figure 6-9.

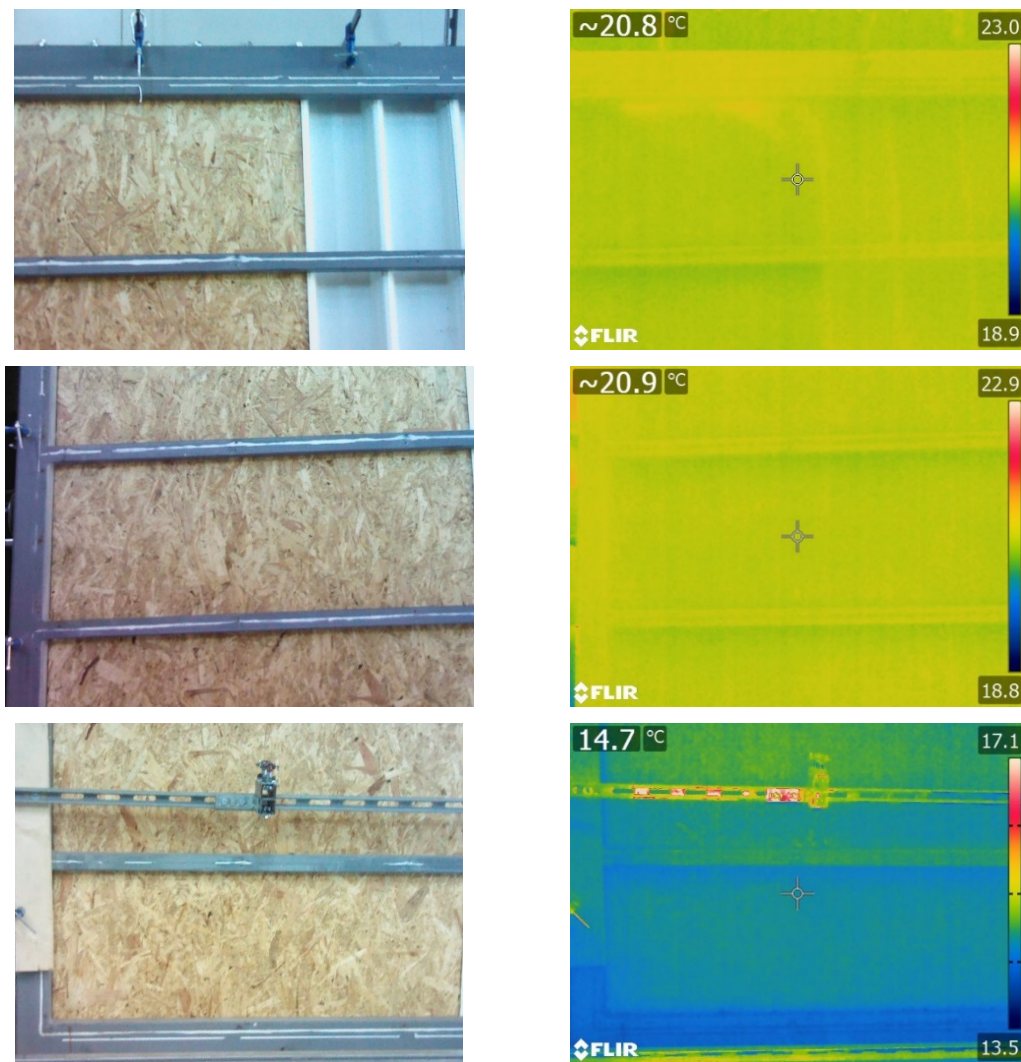


Figure 6-9: Photos and thermographic images of the specimen after the test.

- **Steel omega profiles**

The steel omega profiles wall was subjected to suction and to suction after prolonged wetting test.

Acrylic plates were mounted to the inner face of the specimen and carefully sealed to simulate the presence of a wall. Holes with a diameter of 15 mm were drilled in the acrylic plates, at approximately every square meter of the specimen, to ensure an adequate air permeability of the support. Additionally, 3 holes with 8 mm diameter were drilled in one of the omega profiles and in the centre of two expanded cork boards (one in Zone A and the other in Zone B) for placing the displacement transducers. Then, the specimen was fitted into the test

chamber with its outer surface facing inside the chamber (Figure 6-10). The suction test was initiated.



Figure 6-10: Finalized wall before the suction test.

As before, a maximum suction pressure of 3000 Pa was applied. The specimen endured this pressure without suffering any failure. It was also found that the values recorded for the maximum and residual deformations were very low (0.55 mm for Zone A and 0.50 mm for Zone B).

The specimen wall was then subjected to prolonged wetting for 94 hours, as previously described, after which it was once again subjected to the suction test (Figure 6-11a).

As can be seen in Figure 6-11b, it withstood the pressure without suffering any failure, both regarding the bonding and the ICB material. As before, the registered residual deformations were very low (0.57 mm for Zone A and 0.53 mm for Zone B).



a)



b)

Figure 6-11: Suction test after prolonged wetting: a) During wetting b) Final appearance of the panel where it can be seen that there is no mechanical failure.

The test results indicate that, with regards to wind suction resistance, it is possible to consider the larger space between profiles (485 mm).

After the wall dried, it was subjected to the hard and soft body impact test.

The hard body impact tests were carried out in the two previously defined zones: zone A and zone B.

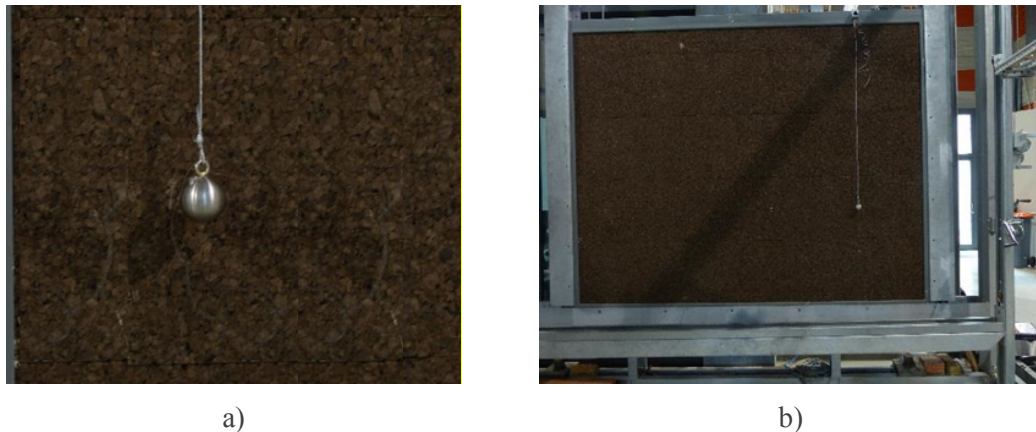


Figure 6-12: Hard body tests impact zones a) Zone A; b) Zone B.

Both areas showed no signs of detachment or material failure after the impact (see Figure 6-12).

Since zone A is the most critical zone, due to the greater distance between the supporting profiles, the large soft body impact test was carried out only for this zone (Figure 6-13).



Figure 6-13: Soft large body impact test.

As before, there was no evidence of detachment or material failure after the impact.

Considering these results, for a maximum distance between profiles of 485 mm, it can be concluded that this solution is adequate for use in areas which accessible to the public, at ground level and vulnerable to impacts.

6.3 Final remarks

In this chapter, three constructive solutions with externally applied ICB (OSB base, corrugated metal panel base, and steel omega profiles support structure) were experimentally tested. Their behaviour when subjected to suction, suction after prolonged wetting, and impact loads was evaluated, as well as regarding water-tightness.

It can be concluded that the studied constructive solutions can endure extreme weather conditions, while maintaining their mechanical integrity and water-tightness. To evaluate the resistance to impact, the solution which was expected to perform the worse (ICB fixed to omega profiles), was tested using both hard and soft body impact loads. It was observed that, for both tests, the constructive solution maintained its mechanical integrity. Thus, this constructive solution (485 mm distance between profiles) is considered to be suitable for application in zones easily accessible to the public at the ground level.

6.4 References

- [1] J.D. Silvestre, N. Pargana, J. De Brito, M.D. Pinheiro, V. Durão, Insulation cork boards-environmental life cycle assessment of an organic construction material, *Materials* (Basel). 9 (2016) 1–16. doi:10.3390/ma9050394.
- [2] W.A. Dalglish, W.R. Schriever, Wind pressures on buildings, *Can. Build. Dig. No. CBD-34*. (1968).
- [3] A. Elshaer, A. Gairola, K. Adamek, G. Bitsuamlak, Variations in wind load on tall buildings due to urban development, *Sustain. Cities Soc.* 34 (2017) 264–277. doi:10.1016/j.scs.2017.06.008.
- [4] X. Jing, Y. Li, Wind tunnel tests for wind pressure distribution on gable roof buildings, *ScientificWorldJournal*. 2013 (2013) 396936. doi:10.1155/2013/396936.
- [5] D.-X. Zhao, B.-J. He, Effects of architectural shapes on surface wind pressure distribution: Case studies of oval-shaped tall buildings, *J. Build. Eng.* 12 (2017) 219–228. doi:10.1016/j.job.2017.06.009.

- [6] Y. Uematsu, N. Isyumov, Wind pressures acting on low-rise buildings, *J. Wind Eng. Ind. Aerodyn.* 82 (1999) 1–25. doi:10.1016/S0167-6105(99)00036-7.
- [7] B.J.B. Gault, *Structures for architects*, 3rd ed., Routledge, New York, 2014.
- [8] S. Selvarajah, A.J. Johnston, Water permeation through cracked single skin masonry, *Build. Environ.* 30 (1995) 19–28. doi:10.1016/0360-1323(94)E0033-N.
- [9] N. Sahal, M.A. Lacasse, Proposed method for calculating water penetration test parameters of wall assemblies as applied to Istanbul, Turkey, *Build. Environ.* 43 (2008) 1250–1260. doi:10.1016/j.buildenv.2007.03.009.
- [10] J.M. Pérez-Bella, J. Domínguez-Hernández, B. Rodríguez-Soria, J.J. Del Coz-Díaz, E. Cano-Suñén, Estimation of the exposure of buildings to driving rain in Spain from daily wind and rain data, *Build. Environ.* 57 (2012) 259–270. doi:10.1016/j.buildenv.2012.05.010.
- [11] J.M. Pérez-Bella, J. Domínguez-Hernández, E. Cano-Suñén, J.J. del Coz-Díaz, M. Alonso-Martínez, Global analysis of building façade exposure to water penetration in Chile, *Build. Environ.* 70 (2013) 284–297. doi:10.1016/j.buildenv.2013.09.001.
- [12] C. Giarma, D. Aravantinos, Estimation of building components' exposure to moisture in Greece based on wind, rainfall and other climatic data, *J. Wind Eng. Ind. Aerodyn.* 99 (2011) 91–102. doi:10.1016/j.jweia.2010.12.001.
- [13] I. Chand, P.K. Bhargava, Estimation of driving rain index for India, *Build. Environ.* 37 (2002) 549–554. doi:10.1016/S0360-1323(01)00057-9.
- [14] James P., K.R. Lisø, E.J. Førland, K. Nore, J.V. Thue, A driving rain exposure index for Norway, *Build. Environ.* 40 (2005) 1450–1458. doi:10.1016/j.buildenv.2004.11.018.
- [15] S. Sanchez-Saez, S.K. García-Castillo, E. Barbero, J. Cirne, Dynamic crushing behaviour of agglomerated cork, *Mater. Des.* 65 (2015) 743–748. doi:10.1016/j.matdes.2014.09.054.
- [16] R. Ferreira, D. Pereira, A. Gago, J. Proença, Experimental characterisation of cork agglomerate core sandwich panels for wall assemblies in buildings, *J. Build. Eng.* 5 (2016) 194–210. doi:10.1016/j.job.2016.01.003.
- [17] O. Castro, J.M. Silva, T. Devezas, A. Silva, L. Gil, Cork agglomerates as an ideal core material in lightweight structures, *Mater. Des.* 31 (2010) 425–432.

doi:10.1016/j.matdes.2009.05.039.

- [18] ETAG 034: Guideline for European Technical Approval of Kits for External Wall Claddings Part I: Ventilated Cladding Kits Comprising Cladding Components and Associated Fixings, European Organisation for Technical Approvals, (2012).
- [19] EN 12155:2000 Curtain walling. Watertightness. Laboratory test under static pressure, European Committee for Standardisation, (2000).
- [20] ISO 7892: 1988 - Vertical building elements -- Impact resistance tests -- Impact bodies and general test procedures, International Organization for Standardisation, (1988).

Chapter 7

Final Considerations

7.1 Overview and main conclusions

Insulation materials produced from recycled or natural materials are among the solutions increasingly widely used to obtain more sustainable and more energy efficient buildings. Expanded cork board is an insulation material that is 100% natural and recyclable, and its use, uncoated, for external insulation is growing. However, this has not been supported by detailed technical characterisation. This work set out to characterise, experimentally and numerically, the application of ICB as an external thermal insulation composite system for both new building construction and for retrofitting projects.

This work started by reporting a survey on existing ICB coated buildings (Chapter 2). It was observed that water accumulation and water run-off, mostly caused by inadequate construction details, are the main causes of the most common building anomalies (development of fungi, lichens, and mosses). It was also noted that the ICB coated buildings' performance depends on the local environment and on the orientation of the building facades. Procedures for applying the ICB boards on different supports, on new buildings and retrofitting interventions, have been proposed. Constructive details and maintenance procedures have also been presented.

In Chapter 3 mechanical and hygrothermal properties of both standard (ST) and medium (MD) density ICB were evaluated. MD ICB showed far better mechanical behaviour than the standard material, without significant changes in its hygrothermal behaviour. Therefore, a more comprehensive study of MD ICB hygrothermal properties was performed.

The thermal conductivity of the MD ICB was measured from dry to moisture saturation state. It was found that the thermal conductivity varies linearly with the material moisture content. The adsorption/desorption curves of the MD ICB were found to exhibit significant hysteresis.

During the drying process of the saturated material it was found that more than a half of its initial water content was lost in the first nine hours under the action of gravity. After this time, the drying process becomes considerably slower.

It was observed that the MD ICB is resistant to long-term exposure to external factors, such as freeze-thaw cycles and sunlight. It was also observed that long-term deformation of the material under permanent loads is acceptable. However, care must be taken when the material is used on roofs since heavy equipment can induce undesirable long-term deformations.

In Chapter 4, an OSB wall covered with uncoated expanded cork and exposed to rain was studied experimentally using a hot-box apparatus. Steady- and unsteady-state for both dry and wet winter and summer conditions were studied. The thermal behaviour of the wall was simulated for the same boundary conditions using an analytical model to simulate the heat transfer phenomenon. To quantify the importance of the material moisture content to the wall's thermal behaviour, the analytical results were compared with those obtained experimentally. It was found that the water penetration throughout the wall was limited to the exterior surface layers. The moisture transport phenomenon and the changes in the hygrothermal material properties are almost entirely confined to the first layers of the expanded cork cladding and to the rainy period, and they are mainly caused by the temperature of the water.

In Chapter 5, the heat and moisture transfer through walls made from OSB and concrete and covered with uncoated medium density ICB were modelled using a boundary element method. First, the changes in the relative humidity, moisture content, and temperature within the OSB wall were evaluated by performing a numerical simulation over a period of 200 days. It was observed that the transport of heat in the wall was several orders of magnitude faster than the transport of moisture, indicating that the moisture transport through the wall is only relevant when there are significant weather changes during the course of the year.

Furthermore, the hygrothermal performance of OSB and concrete walls, when subjected to real weather data (including solar heat flux), was evaluated. Summer and winter weather conditions in Bragança (Portugal) and Seville (Spain) were selected to illustrate the main findings. It was noted that whereas the solar heat flux has a significant impact on the surface temperature and relative humidity, the short-term environment moisture variation only affects the relative humidity of the surface layers. However, the maximum relative humidity at depths not affected by the external periodic variations is higher for the OSB wall. For both walls, a change in the exterior surface temperature changes the temperatures across the entire wall in a short time. Thus, it was observed that the moisture content along the ICB coated walls is high only when the external moisture content is high and remains high. When the exterior relative humidity varies periodically, despite being high, the relative humidity in the walls is similar to the relative humidity of the interior environment.

In Chapter 6, some experimental tests were performed. Constructive solutions covered with medium density ICB were subjected to wind, rain and impact loads. Wood/corrugated metal plate and omega metal profile specimens were built. Wind suction resistance test, under dry

and wet conditions, as well as waterproof and impact tests were conducted. The results allow to conclude that the proposed solutions are able to resist to extreme weather conditions and can be applied in areas easily accessible to the public, such as those at ground level. Regarding the assembling of omega metal profiles, the distance between profiles was established as 485 mm.

From the work carried out in this thesis, it can be concluded that medium density expanded cork board is suitable to be used as an uncoated external thermal insulation. The required thermal insulation is ensured, even in wet conditions, as is the mechanical resistance to extreme weather conditions and to accidental impacts. However, to ensure a durable solution and to minimise the occurrence of anomalies, the proposed construction guidelines must be followed.

7.2 Future work

The evaluation of the mechanical and hygrothermal behaviour of the expanded cork agglomerate carried out in this thesis has shown that this material can be used, uncoated, for the external insulation of buildings. Although it is considered that the main objectives of this work have been achieved, some future work that may be considered would include:

- evaluating experimentally the hygrothermal behaviour of ICB coated wall subjected simultaneously to wetting, pressure and solar radiation;
- incorporating water percolation through the ICB into the numerical model;
- incorporating the water freeze effect within the ICB into the numerical model.

